INFORMATION TO USERS

This manuscript has been reproduced from the microfilm master. UMI films the text directly from the original or copy submitted. Thus, some thesis and dissertation copies are in typewriter face, while others may be from any type of computer printer.

The quality of this reproduction is dependent upon the quality of the copy submitted. Broken or indistinct print, colored or poor quality illustrations and photographs, print bleedthrough, substandard margins, and improper alignment can adversely affect reproduction.

In the unlikely event that the author did not send UMI a complete manuscript and there are missing pages, these will be noted. Also, if unauthorized copyright material had to be removed, a note will indicate the deletion.

Oversize materials (e.g., maps, drawings, charts) are reproduced by sectioning the original, beginning at the upper left-hand corner and continuing from left to right in equal sections with small overlaps.

Photographs included in the original manuscript have been reproduced xerographically in this copy. Higher quality 6" x 9" black and white photographic prints are available for any photographs or illustrations appearing in this copy for an additional charge. Contact UMI directly to order.

Bell & Howell Information and Learning
300 North Zeeb Road, Ann Arbor, MI 48106-1346 USA
800-521-0600

A Neutralization-Reionization Mass Spectrometry and Computational Analysis of 3-Hydroxypyridine, 2-Hydroxypyridine/2-(1H)Pyridone, and Uracil

Jill K. Wolken

A dissertation submitted in partial fulfillment of the
requirements for the degree of

Doctor of Philosophy

2000

Program authorized to offer degree: Department of Chemistry

In presenting this dissertation in partial fulfillment of the requirement for the Doctoral degree at the University of Washington, I agree that the Library shall make its copies freely available for inspection. I further agree that extensive copying of the dissertation is allowable only for scholarly purposes, consistent with "fair use" as prescribed in the U.S. Copyright Law. Requests for coping or reproduction of this dissertation may be referred to Bell and Howell Information and Learning, 300 North Zeeb Road, Ann Arbor, MI 48106-1346, or to the author.

Signature Jill K. Wolken

Date June 5, 2000

University of Washington
Graduate School

This is to certify that I have examined this copy of a doctoral dissertation by

Jill Karen Wolken

And have found that it is complete and satisfactory in all respects, and that any and all revisions required by the final examining committee have been made.

Chair of Supervisory Committee:

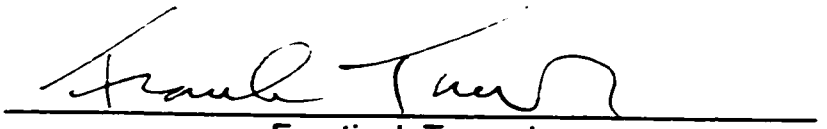

Frantisek Turecek

Reading Committee:

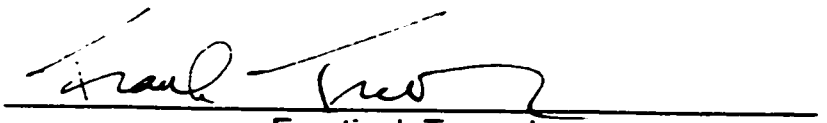

Frantisek Turecek

Craig Beeson

Richard Gammon

Date: May 24, 2000

University of Washington

Abstract

A Neutralization-Reionization Mass Spectrometry and Computational Analysis of 3-Hydroxypyridine, 2-Hydroxypyridine/2-(1H)Pyridone, and Uracil

Jill K. Wolken

Professor Frantisek Turecek

Department of Chemistry

Free radical damage to DNA has been studied since the early years of radiobiology, when it became well established that DNA, and specifically the purine and pyrimidine bases are critical cellular target for radiation-induced damage. Cytosine and uracil are of key importance since the observation that cytosine deaminates to form uracil at a finite rate in vivo. Although a detailed mechanism has not been well established, it has been observed that radical damage increases mutations such as the C to A point mutation which occurs if uracil is left in the replicating DNA strand. This dissertation focuses on both modeling studies for the pyrimidine base radicals by examining the 3-Hydroxypyridine and the 2-Hydroxypyridine / 2-(1H)Pyridone system as well as the more complicated uracil system by neutralization-reionization mass spectrometry.

Neutralization - reionization mass spectrometry (NRMS) is a technique that allows the characterization of radical stability and dissociation pathways by femtosecond electron collisions of the corresponding ion with a target gas, typically dimethyldisulfide. *Ab initio* and density functional theory help characterize the protonation sites in addition to the radical and ion stabilities. Kinetic modeling, such as RRKM is useful in determining which expected fragmentation pathways could occur on the time scale of the experiment. These computational techniques aid in interpretation of the NRMS spectra.

Table of Contents

List of Figures

Chapter 4. **2-Hydroxypyridine / 2-(1H)pyridone**

Chapter 5. **Uracil**

List of Tables

Acknowledgements

I would sincerely like to thank my research supervisor, Dr. Frantisek Turecek, for his expertise and encouragement throughout the entire course of my graduate studies. I would also like to acknowledge others from whom I have learned a great deal through many enlightening discussion: Dr. Terry Olney and Dr. Aaron Frank. I would also like to thank the people who have contributed significantly to my understanding of the 'proper way' to teach chemistry: Dr. William Zoller and Dr. Richard Gammon.

I would like to thank the staff at the mass spectrometry facility at UW for their assistance in maintaining the mass spectrometers, in particular Mr. Jim Roe and Dr. Martin Sadilek.

Funding for this research was provided by the National Science Foundation. Computations were performed on the Computational Cluster maintained at UW and funded by the department of Chemistry with matching funds from the National Science Foundation.

Finally, I wish to thank my mom, Kathy Wolken, and Jack Debertin and the rest of my family for their continual support, infinite patience and unlimited encouragement. This thesis is dedicated to them.

Chapter I. Introduction:

Free radical damage to DNA has been studied since the early years of radiobiology, when it became well established that DNA, and specifically the purine and pyrimidine bases, was a critical cellular target for radiation-induced damage[1]. Attention was focused on oxygen free radicals after the discovery of the enzyme superoxide dismutase (SOD) by McCord and Fridovich[2] which acts to eliminate superoxide to form hydrogen peroxide and oxygen (1).

$$\bullet O_2^- + \bullet O_2^- \xrightarrow{SOD/2H+} H_2O_2 + O_2 \qquad (1)$$

With the discovery of SOD, interest in DNA damage induced by oxidative stress was quickly brought into the forefront. DNA damage by oxygen free radicals is frequently postulated to cause mutations which are thought to initiate and/or progress human cancers. It is a daunting task to prove this relationship between oxygen free radicals and cancer due to the large number of reactive oxygen species that can potentially damage DNA. These highly reactive chemical species[3] include H_2O_2, $\bullet O_2^-$, $^1O_2$, $\bullet OH$, NO_2, $RO\bullet$, and $ROO\bullet$, and although each molecule has a distinct chemistry and distribution within a cell, all of them have the potential to alter nucleotide residues. Upon reaction with DNA, oxygen radicals can produce over 30 different adducts and this excludes protein and lipid addition products, and different types of cross linking[4]. There are potentially hundreds of different types of chemical changes which could occur in DNA from oxygen free radicals that could cause mutagenic lesions involved in human cancers.

There are currently numerous chromatographic and electrophoretic assays that allow quantitation of individual photo-induced and oxidative DNA base modification. However, these techniques are limited to targeting stable base modified adducts and do not attempt to understand the radical chemistry by which these adducts were formed. There are currently three general 'tools' being used to understand radical chemistry starting with the primary ionization event to the final nonradical products: 1) product

analysis studies on the building blocks of DNA and model compounds for them 2) electron paramagnetic resonance (E.P.R.) in matrices, single crystals, and liquid solution 3) time resolved methods with mainly optical and conductance detection on DNA components and model compounds[4].

In this thesis, I showed how to employ Neutralization - Reionization Mass Spectrometry (NRMS) in conjunction with computational analysis as yet another tool to study radicals relevant to DNA damage by free radicals.

Neutralization - Reionization Mass Spectrometry (NRMS) is a mass spectrometry technique which probes the chemistry of neutral molecules[5]. Lavertu[6] discovered in 1966 that fast ionic beams undergo charge exchange upon collision with a neutral target gas to create a beam of neutral molecules. This observation led to investigating gas-phase chemistry of neutral species by mass spectrometry. Porter[7] et. al. used neutralized ion beams to investigate hypervalent radicals[8], including the Rydberg states of $\bullet H_3$. McLafferty[9] et. al. advanced the study of radicals with studies of polyatomic organic intermediates. In recent years, NRMS had become a powerful tool for the formation and identification of a number of previously elusive species[10].

A schematic representation of a NRMS experiment is depicted in Figure 1. In a typical NRMS experiment, a beam of fast ions collides with a target gas (CH_3SSCH_3), forming neutral species. The remaining fast ions are deflected, and the neutral species are allowed to travel along the chamber. These surviving neutral species and fragments of these species are reionized by a collision with another gas. The reionized beam[5] is then analyzed, or can be subjected to further experimentation.

NRMS has some distinct advantages when compared to other experimental techniques. First, there are no solvent or wall effects since the gas-phase molecules of interest are in high vacuum. Secondly, all techniques for ion preparation can be utilized to form neutral species of interest. Oftentimes, other experimental techniques are restricted to photochemical or thermal generation of short-lived neutrals[5].

It should be noted that NRMS has some limitations which makes direct observation of the neutral spectrum elusive. Since the detector at the end of the flight

chamber detects ions, and not neutrals, the resulting mass spectrum is a superposition of the spectra of neutral and ion dissociation products. In addition, if rearrangements of neutral species are often difficult to decipher based solely upon the NR spectrum. Oftentimes, computational calculations are performed on molecules of interest to aid in the interpretation of NRMS data.

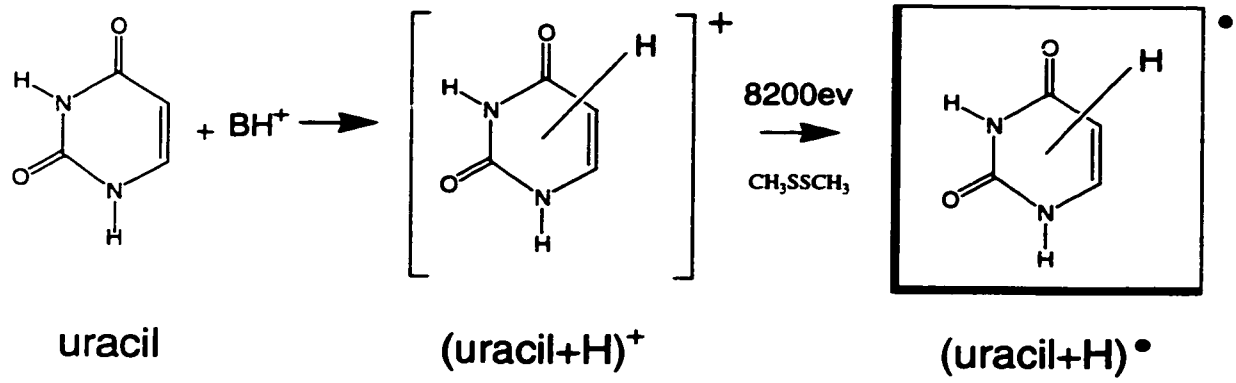

Figure 1. Schematic representation of a Neutralization - Reionization experiment of mass selected uracil ions.

In the work presented, *ab initio* and density functional theory (DFT) were used to determine energetics of species that had special interest to DNA radical damage while Rice-Ramsperger-Kessel-Marcus (RRKM) calculations were performed to understand the reaction kinetics. These techniques together proved extremely useful in the interpretation of NRMS data. *Ab initio* and density functional theory were used to determine the thermodynamic stabilities of ions and radicals, where RRKM was used to determine the unimolecular rate constants for fragmentation pathways.

The *ab initio* method presented in this work is based on molecular orbital (MO) theory. The approximate treatment of electron density and motion places individual electrons in one-electron functions, called spin orbitals. These spin orbitals consist of a spatial component ($\Psi(x,y,z)$) and a spin component (α or β). In the simplest form of MO

theory, a single assignment of electrons to orbitals (often called the electronic configuration) is made. These single electron orbitals are brought together to form approximate many-electron wave function Ψ, which is the simplest MO approximation to the solution of the Schrödinger equation[11].

In practice, the MO Ψ_1, Ψ_2, ...Ψ_n are further restricted to be a linear combination of a set of N known one-electron functions satisfying the conditions:

$$\Psi_i = \sum_{\mu=1}^{N} c_\mu \varphi_\mu \qquad (2)$$

The functions φ_1, φ_2....φ_N are defined in this specification of the model are known as one-electron basis functions, or simply basis functions. If the basis functions are the atomic orbitals for the atoms which compose the molecule, this is described as the linear combination of atomic orbitals (LCAO) approximation. The unknown coefficients, c_μ are determined so the total electronic energy calculated from the many-electron wavefunction is minimized according to the variational theorem. The variational theorem assures that the energy calculated will be the smallest energy possible while still being greater then the exact solution of the Schrödinger equation energy. This energy represents the best energy which can be obtained within the limits of the method. This is the lowest energy with the constraints imposed by 1) the use of limited basis set in the orbital expansion and 2) the use of a single assignment of electrons to orbitals. The lowest energy possible is called the Hartree-Fock limit, since even with the largest basis set, the energy obtained is not an exact solution of the Schrödinger equation[11].

The deficiency of the Hartree-Fock theory is the incomplete description of the correlation between motions of electrons. Even with a large and completely flexible basis set, the exact solution of the Schrödinger equation cannot be written as a single electron configuration. To correct for this error, it is necessary to use wavefunctions which include electron correlation beyond the Hartree-Fock level. There are many different approaches to account for electron correlation, but in the work presented here, second order Møller-Plesset[12] (MP2) perturbation theory, DFT, and quadratic configuration interaction were used exclusively. Figure 2 shows a schematic representation of theoretical models and

how both improvement of the basis set and improvement of the correlation treatment is needed to arrive at the exact solution of the Schrödinger equation.

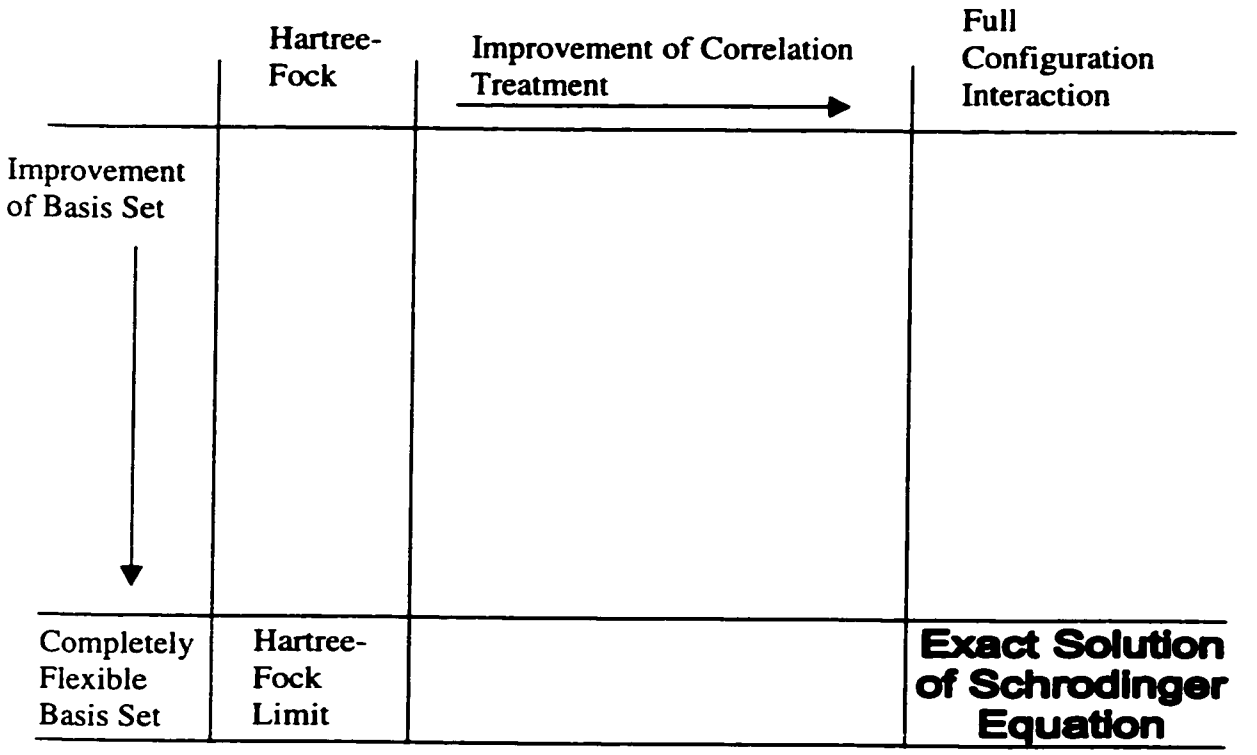

Figure 2. Schematic representation[11] of the theoretical models showing basis set improvement vertically and correlation improvement horizontally.

The second order Møller-Plesset[12] (MP2) theory attempts to find the lowest energy of the full Hamiltonian matrix by treating the matrix as the sum of two parts, the second being a perturbation of the first. The MP2 approximation of electron correlation is computationally feasible in addition to providing a decent approximation (~ 90%) of the electron correlation. However, MP2 energies, like all perturbation theories, are no longer variational, and consequently are no longer an upper bound of the exact solution of the Schrödinger equation[11].

The B3LYP method is based on density functional theory (DFT) which is combined with MO theory. The DFT allows the N-electron equation wave function ($\Psi(\chi_1, \chi_2,...\chi_n)$) and the associated Schrödinger equation to be replaced by a relatively simple electron density $\rho(r)$. It follows that the ground state electron density uniquely determines the properties of a ground state, and importantly, the ground state energy. The B3LYP calculation is a hybrid method that mixes a non-local density operator of Lee, Yang, and Parr with a Hartree-Fock operator. It is often useful when examining a chemical system computationally that both MO theory and density functional theory be employed to show discrepancies between the two theories[13].

While knowing the energetics of any given system is important, stability isn't the only factor when deciphering spectra from a NRMS instrument. Since the neutral time of flight is limited by the 60 cm long flight path, only fragmentation pathways which can occur on the timescale of the instrument are expected to be seen at the detector. Therefore, it can also be useful to model reactions kinetically. Rice-Ramsperger-Kassel, later refined by Marcus determined an approach to model unimolecular rate constants became known simply as RRKM.

In 1927 and 1928 Rice, Ramsperger, and Kassel developed the framework to understanding the unimolecular reaction[14]. The dissociating system is treated as an assembly of identical harmonic oscillators, one of which is truncated at an energy E_a, which corresponds to the activation energy for dissociation. If the dissociative oscillator happens to have an energy in excess of the activation energy, the molecule dissociates. A fundamental assumption of the theory is that energy is statistically distributed among all the oscillators. The rate of dissociation is then proportional to the probability that for a given total energy E, the dissociative oscillator has an energy greater then the activation energy. The RRK expression for the rate contains two important features. First, it predicts that the rates are a strong function of the number of vibrational oscillators and second, it predicts that the rate increases rapidly with excess energy. Although both of these predictions are correct, the RRK treatment is incapable of determining the correct rate constant for a given dissociation, even within an order of magnitude. The failure of

the RRK theory to predict the correct rate is due to numerous reasons. The main reason is the number of oscillators to correctly model chemically interesting systems needs to be higher then the RRK theory allows. In 1951, Rice and Marcus eliminated the problems associated with classic RRK theory. This quantum theory, which treats the vibrational (and rotational) degrees of freedom in detail, became known as RRKM. The RRKM expression is given by eq. 3. Where $\rho(E)$ is the density of vibrational states of the energy E, $N^{\dagger}(E-E_a)$ is the sum of the vibrational states from 0 to $E-E_a$ in the transition state, h is Planck's constant and σ is the reaction symmetry factor. A major difference between RRKM and RRK theory is that the former depends strongly on the values for the vibrational frequencies[14], while the later does not. For simplicity, the rotational degrees of freedom are not shown in equation 3.

$$k(E) = \frac{\sigma N^{\dagger}(E-E_a)}{h \rho(E)} \qquad (3)$$

With the great improvements in computational speed and accessibility over the last two decades, experimentalist are able to supplement experimental data with computational insight into a given system like never before. This factor has allowed NRMS to clearly established itself in the last decade as a technique designed to study a wide range of radicals and molecules of particular interest and/or unusual structure which can be generated by neutralization of the corresponding cation.

Because it is well known that free radical reactions target DNA bases, NRMS in conjunction with computations could help establish proton affinity, radical stability, and reaction pathways for these molecules. However, since these bases have many basic sites and possible tautomers, a model system was initially chosen to aid in the understanding of the RNA base uracil. Figure 3 shows the structures of 2-hydroxypyridine / 2(1H)-pyridone, 3-hydroxypyridine, and uracil.

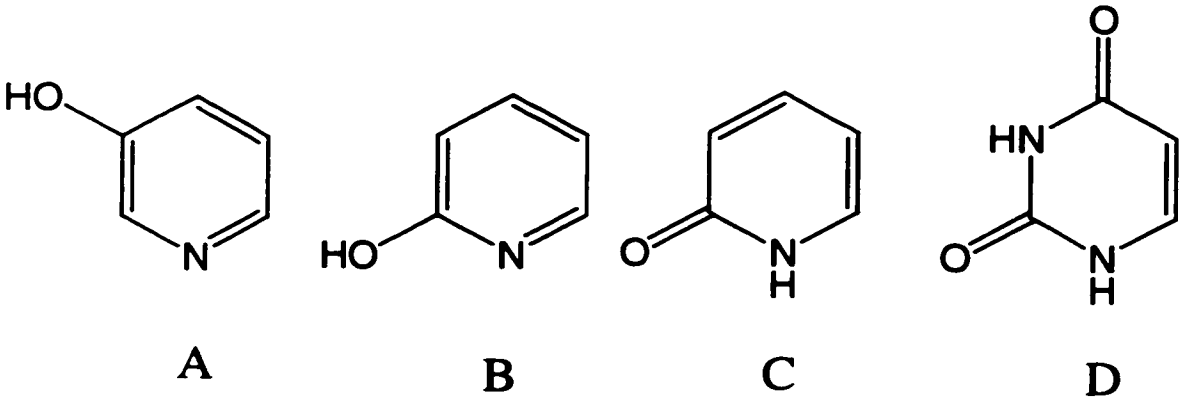

Figure 3. Structures of 3-hydroxypyridine (A), 2-hydroxypyridine (B), 2(1H)-pyridone(C), and uracil(D)

The tautomerization in the 2-hydroxypyridine / 2(1H)-pyridone system has been the study of many investigations because it models the pyrimidine bases. 2-Hydroxypyridine / 2(1H)-pyridone was one of the few systems where the energy difference between the two tautomers is sufficiently small that both species are present in the gas phase. 3-Hydroxypyridine was also investigated since it lacked gas phase tautomers.

In 1907, UV experiments showed 2(1H)-pyridone was more stable in aqueous solution[15]. It wasn't until 1965 with Levine and Rodionova[16] that it was determined the 2-hydroxypyridine was more stable in the gas phase and exists in a ratio of 2:1 at 573K. This was confirmed by Peak[17] et. al. in 1977 when he determined the ratio was closer to 2.6:1 at 412K. The difference in stability between gas phase and aqueous phase allows 2-hydroxypyridine / 2-(1H)pyridone system to be used as a model system for computational chemists seeking to determine solvation effects on model compounds of biologically relevant compounds. For this reason, there are numerous computation gas phase studies for these compounds[18].

In Chapters III and IV, I show how neutralization - reionization mass spectrometry (NRMS) was used to obtain radical information on 2-hydroxypyridine / 2-

(1H)pyridone system in addition to 3-hydroxypyridine. From a combination of NRMS experiments, *ab-initio* calculations, density functional theory calculations, and RRKM calculations, the radical and ionic stabilities, proton affinities, and fragmentation pathways were determined. In Chapter V, the more complicated uracil was studied by NRMS in conjunction with computational modeling to determine a complete picture of radical fragmentation pathways. Chapter VI focuses on addition work, such as cytosine, aminopyridine, and Dabco.

Once the background research on the model compounds were complete, it was necessary to springboard that information to a more complicated biologically relevant system. The system further investigated was the RNA base uracil for the main reason that genome damage in the form of deamination of cytosine to uracil is believed to lead to DNA point mutations[19].

In 1953, James Watson and Francis Crick deduced the three dimensional structure of DNA by analyzing x-ray diffraction photographs of DNA fibers taken by Rosalind Franklin and Maurice Wilkins[20] (Figure 4). It was found the two chains are held together by hydrogen bonds between pairs of bases. Adenine is always paired with thymine and guanine is always paired with cytosine. Uracil replaces thymine in RNA.

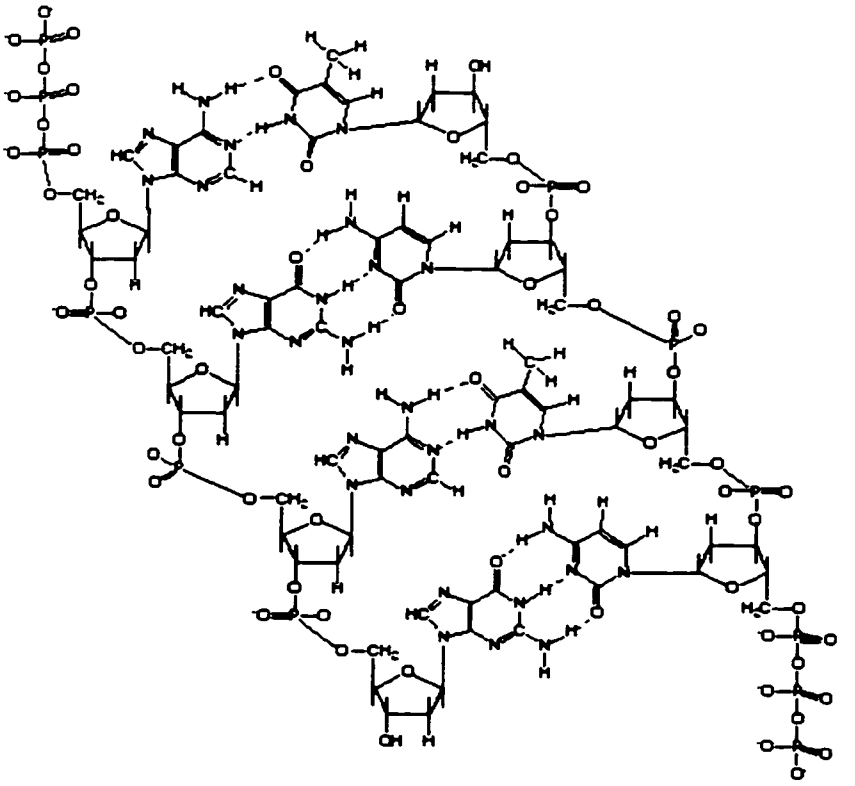

Figure 4. DNA [21]

DNA damage is a universal problem for life. The genetic material is unstable under physiological conditions[19] and can be further assaulted by reactive chemicals. Unrepaired damages can result in loss of genetic information or interfere with transcription and replication. In 1974, it was found by Lindahl and Nyberg[22] that oxidative deamination of DNA cytosine to uracil occurs spontaneously at an appreciable rate. In 1985, Tice and Setlow[23] estimated the rate of spontaneous deamination of cytosine to uracil in DNA is 8 per cell per hour based on data from Shapiro[24]. However, deamination occurs 4000 times faster in single-stranded DNA, making deanimation a significant event in DNA replication[25]. Uracil DNA glycosylases (UDGases), which remove uracil from DNA as the free base yielding an apyrimidinc site in the DNA has been isolated in bacteria strains as well as mammalian cells. These UDGases show amazing specificity for

excision of uracil from DNA, with weak specificity activity against synthetic uracil analogs such as 5-fluorouracil and 5-hydroxyuracil. They act to excise uracil from single-stranded and double-stranded DNA, with excision from single-stranded DNA occurring most quickly. No activity has been reported against any normal DNA base, or against uracil in RNA. However, if the DNA-uracil is not replaced before replication, the uracil behaves like a thymine analog. When the U-containing strand is replicated, this leads to A-U bond, which can be replicated to A-T. This causes an overall mutation of C to T[25].

Over the years, numerous modeling studies of nucleobases have been performed to determine solvation effects and tautomerization energies[26]. The overwhelming consensus is the most stable tautomer of uracil is the dioxo form, regardless of environment.

While a reaction mechanism hasn't been determined for point mutations in DNA, one of the focal point has been studying the chemistry of the radical. In Chapter V, I used *ab initio* calculations, DFT calculation, RRKM kinetic calculations, and neutralization – reionization mass spectrometry to characterize the radical and ion energetics, fragmentation pathways, and transition state energies for both hydrogen extraction and ring cleavage. While there is much work to be done before the complete picture of nucleobases radicals can be understood, an emerging picture of uracil radicals is shown in Chapter V.

Chapter II. Experimental:

Instrumental:

A tandem quadrupole acceleration – deceleration mass spectrometer was used, as described previously[27]. The instrument, shown in Figure 2, consists of a) an ion source, b) quadrupole ion guide, c) acceleration lens, d) neutralization collision cell, e) conduit (drift region), f) reionization collisional cell, g) energy filter, h) mass analyzer, and i) detector.

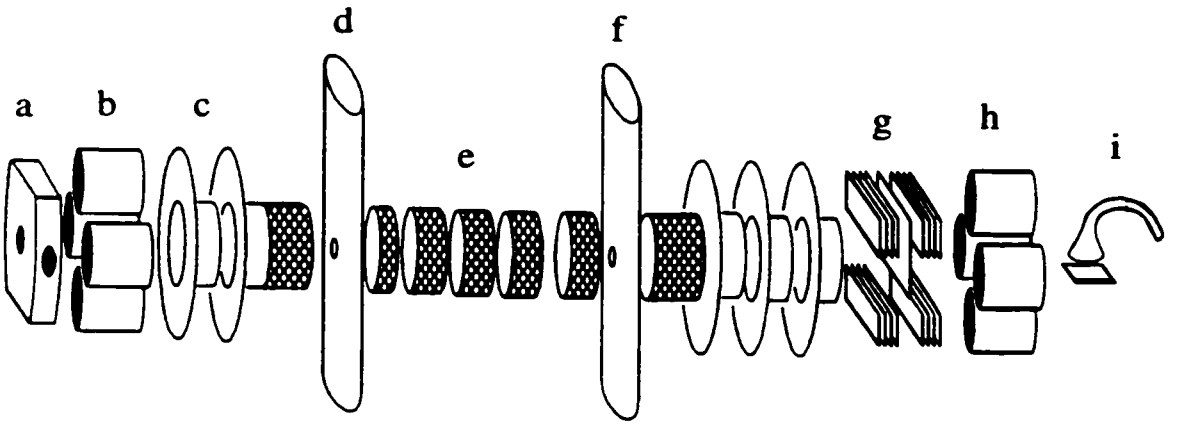

Figure 5. Diagram of neutralization – reionization mass spectrometer

Both a quadrupole ion guide and an electrostatic lens were used to focus the ions exiting the ion source. The ions were accelerated to 8200eV and passed through a differentially pumped collision cell where a neutralization gas was introduced so as to allow 70% transmission of the ion beam. This corresponds to predominantly (≈ 85%) single collisions between the ions and the neutralization gas resulting in a small fraction of neutral species of interest. The neutrals pass through the conduit where a +250V potential is applied to a cylindrical electrostatic lens, rejecting the remaining ions. The conduit is a 60 cm differentially pumped chamber and consists of a gas inlet port for use in neutralization – collisional – reionization (NCR) experiments. The surviving neutrals

and fragments enter a second differentially pumped collisional cell where oxygen is introduced at 70% transmission relative to the incident ion beam to reionize the neutral beam. The fast ions were decelerated to 78 eV kinetic energy and energy filtered by a chicane lens. The ions were mass analyzed by a second quadrupole operating at unit mass resolution and detected by an electron multiplier. The ion currents were converted to a voltage by a Keithley Model 428 amplifier and recorded by a computer controlled data system[27].

All of the samples were introduced into the ion source from a heated glass direct inlet probe extending to the ion source. Both chemical ionization and electron impact were used depending on the type of experiment performed. Electron impact was used to generate cation precursors from stable molecules. Typical electron impact conditions are as follows: electron current 0.5 mA, electron energy 70 eV, source temperature 200-250°C, sample pressure $2.0 \times 10^{-6} - 1.0 \times 10^{-5}$ Torr. The pressure was measured on a Bayard-Alpert ionization gauge located on the differential pump manifold.

The chemical ionization source, which consists of a 'high pressure' reaction cell, is used to form protonated precursors. Typical chemical ionization conditions are as follows: electron current 1.0 mA, electron energy 100 eV, source temperature 200-250°C, sample pressure $2.0 \times 10^{-6} - 1.0 \times 10^{-5}$ Torr, reagent pressure $5.0 \times 10^{-5} - 2.0 \times 10^{-4}$ Torr. The reagents used were NH_3, H_2O, $(CH_3)_2CO$, and CH_4. Deuterated reagents were used to deuterate samples. The proton affinities of the reagents were 853, 812, 697, and 551 kJ/mole respectively to create ions with a range of internal energies. Protonation conditions were maximized such that $[M + H]^+ / M^+$ ratio > 10, and in most cases was greater then 20.

Neutralization – collisional – reionization (NCR) experiments of the intermediate neutrals was performed by admitting helium into the differentially pumped conduit region such as to achieve 30, 50, and 70% transmission of the ion beam. The collisions between the neutral beam and the helium creates greater internal energy in the neutrals, and oftentimes, greater neutral fragmentation.

Collision-induced dissociations (CAD) were measured on a JEOL HX-110 doubly focusing mass spectrometer with an EB geometry (electrostatic sector E preceded magnet B). Air was used as a collision gas at pressures allowing 50% transmission of the ion beam at 10keV. CAD spectra were measured in the first field-free region and the spectra were recorded with use of a linked B/E scan. The spectra were averaged over 10-20 consecutive scans.

Materials: All chemicals were used as received without further purification: 1,4-Diaxabicyclo[2.2.2]octane-DABCO(Aldrich, 98%), 2-Hydroxypyridine (Aldrich, 97%), 3-hydroxypyridine (Aldrich, 98%), uracil (Aldrich, >99%), cytosine (Aldrich, >99%), NH_3 (Matheson, 99.99%), ND_3 (Matheson, 99% D), $(CH_3)_2CO$ (Aldrich, 99.7%), $(CD_3)_2CO$ (Cambridge Isotope Laboratories, 99.9% D), H_2O (Aldrich, >99%), D_2O (Cambridge Isotope Laboratories, 99.9% D), CH_4 (Matheson, 99.97%), CD_4 (Cambridge Isotope Laboratories, 99% D) dimethyl disulfide (Aldrich, 99%), and O_2 (>99%). Freeze-thaw cycles were used to degas the neutralization gas prior to use.

Calculations:

Standard ab initio calculations were carried out using the Gaussian 94 and 98 suites of programs[28]. Geometries were optimized with Hartree-Fock calculations (RHF/6-31G(d,p) for the molecules, UHF/6-31G(d,p) for the radicals, and UHF/6-31+G(d,p) for the transition states). Harmonic frequencies were calculated with HF/6-31G(d,p) (or UHF/6-31+G(d,p) for the transition states) and used to characterize local minima (all frequencies real) and first order saddle points (1 imaginary frequency). Dissociation pathways were investigated with stepwise calculations in with the dissociating bond was held fixed while the remaining degrees of freedom were fully optimized. The HF frequencies[11] were scaled by 0.893 and used to calculate zero-point energy corrections, enthalpies, and partition functions. Single point energies were obtained by B3LYP and Møller-Plesset perturbation calculations truncated at second order with frozen core excitations (MP2) using the larger 6-311G(2d,p) and 6-311+G(2d,p) basis sets. The spin-

unrestricted MP2 calculations (UMP2) were affected by contamination from higher spin states. Annihilation of higher spin states by spin projected[29] reduced the $< S^2 >$ and resulted in lower projected MP2 values. These PMP2 values were used in place of MP2 for all open shelled systems. At the highest level of theory, quadratic configuration interaction calculations (QCISD) were performed and extrapolated to effective QCISD/6-311+G(2d,p) by a composite procedure (eq. 4) based on additivity approximation[30].

$$\begin{aligned} \text{QCISD/6-311+G(2d,p)} \approx \text{QCISD(6-31G(d,p)} + \\ \text{MP2/6-311+G(2d,p)} - \text{MP2(6-31G(d,p)} \end{aligned} \tag{4}$$

This treatment is analogous to the G2(MP2) scheme[31] and its modifications[32] but uses smaller basis sets for the single-point calculations. The QCISD energies are less sensitive to spin contamination and were shown to have differences between PMP2 and UMP2 of < 1 mhartree for radicals and < 3 mhartree for transition states for a similar system[33]. QCISD energies for uracil were compared between ROMP2 and PMP2 for internal consistency and are discussed further in Chapter 5.

RRKM calculations of unimolecular rate constants were performed using Hase's program[34]. Direct counting of quantum states was used to acquire microcanonical rate constants, k(E,J,K), which were Boltzmann averaged over the rotational states to provide k(E) values.

Chapter III. 3-Hydroxypyridine

The 3-hydroxypyridine (**3**) system was studied by experimental and theoretical methods. This system was simpler then the 2-hydroxypyridine / 2(1H)-pyridone (**1,2**) system discussed later in Chapter 4 by the lack of tautomerization in the gas phase. This allowed a more straightforward investigation of the radical stability, energetics, and fragmentation pathway. The work from this chapter has been previously published in *J. Am. Chem. Soc.* **1999**, *121*, 6010-6018.

Numerous ion and radical structures are discussed in the following text. For clarity, a system has been developed. 2-Hydroxypyridine, 2-(1H)pyridone, and 3-hydroxypyridine are referred to as **1,2,3**, respectively. Ions of **1,2**,and **3** are referenced by $\mathbf{1}^+$, $\mathbf{2}^+$, and $\mathbf{3}^+$, whereas radicals are $\mathbf{1}^\bullet$, $\mathbf{2}^\bullet$, and $\mathbf{3}^\bullet$. Protonated ions are referenced as $\mathbf{1aH}^+$, where **1** refers to 2-hydroxypyridine, the **H** refers to protonation with an H atom, the charge designates an ion, and **a** refers to position where the proton resides. The **a** refers to protonation at the nitrogen (N1), **b**,**c**,**d**,**e**, and **f** refer to the ring positions C2, C3, C4, C5 and C6 respectively. The **g** refers to the oxygen position (O7). To refer to a radical, the charge has been replaced by a dot (i.e. **2aH•**), and to indicate the addition of a deuterium, the H has been replaced by a D (i.e. $\mathbf{2aD}^+$). It should be noted that **2** cannot be protonated at the C2 site, so an ion or radical does not exist with a proton residing at the C2 position. The naming is consistent throughout chapters 3 and 4.

Every calculation was performed with both *ab initio* theory and density functional theory. Both energies are reported, with the *ab initio* calculation always reported first (e.g 323/346 kJ/mol). This corresponds to MP2 / B3LYP. Unless otherwise indicated, the basis set is 6-311G(2d,p).

Abstract:

Radicals 3-hydroxy-(1H)-pyridinium (**3aH•**) through 3-hydroxy-(6H)pyridinium (**3fH•**) and 3-pyridylhydroxonium (**3gH•**) were studied as models of hydrogen atom adducts to nitrogen heterocycles. Radical **3aH•** was generated in the gas phase by femtosecond collisional electron transfer to stable 3-hydroxy-(1H)-pyridinium cations (**3aH$^+$**). The fractions of nondissociating **3aH•** decreased with increasing internal energy of the precursor cations as determined by the gas-phase protonation energetics. Radical **3aH•** dissociated unimolecularly by loss of the N-bound hydrogen atom to produce 3-hydroxypyridine (**3**). The dissociation showed large isotope effects that depended on the internal energy of the radical. Other dissociations of **3aH•** were loss of OH•, ring contractions forming C-OH and pyrrole, and ring cleavages leading to C_3H_x and C_2H_xN fragments. Combined MP2 and B3LYP/6-311g(2d,p) calculations yielded proton affinities in **3** as 938 (N1), 757 (C2), 649 (C3), 721 (O), 727 (C4), 714 (C5), and 763 (C6) kJ/mol. **3aH$^+$** was the most stable isomer formed by protonation of **3**. Radical **3aH•** was the most stable isomer whereas **3bH•**, **3cH•**, **3dH•**, **3eH•**, and **3fH•** were calculated to be 9, 48, 16, 18, and 22 kJ/mol less stable then **3aH•** respectively. The 3-pyridylhydroxonium radical **3gH•** dissociated without a barrier by cleavage of the OH bond. N-H bond dissociation in **3aH•** was 102 kJ/mol endothermic at 298K and required an activation energy of 126 kJ/mol. Deuterium isotope effects on the N-(H,D) bond dissociations were modeled by RRKM calculations and used to estimate the internal energy distribution of **3aH•**. Isomerizations of **3aH•** → **3bH•** and **3bH•** → **3cH•** required activation energies of 174 and 130 kJ/mol respectively. Ring-cleavage dissociations of **3aH•** were > 220 kJ/mol endothermic. The occurrence of competitive ring cleavage dissociations pointed to a bimodal internal energy distribution in **3aH•** due to the formation of excited electronic states upon electron transfer. The electronic properties and excited states of heterocyclic radicals are discussed.

Results and Discussion

Ion Stability:

The ions of **3** were investigated using MP2 and B3LYP calculations with the 6-311G(2d,p) basis set. The results are shown in Table 1. The most stable ion from both sets of calculations was **3aH$^+$** by over 150 kJ/mol. The trends for ion stability remain constant until the 4^{rth}, 5th, and 6th positions where there are theory dependent differences.

Table 1. Ion Structure and Relative Stability of protonated 3-hydroxypyridine (**3**)

Ion Structure	Symbol	Relative Stability MP2 / B3LYP	Ranking MP2	Ranking B3LYP
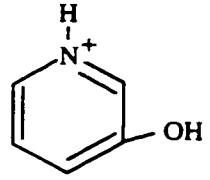	**3aH$^+$**	0 / 0	1	1
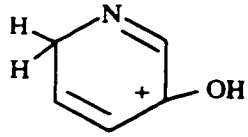	**3fH$^+$**	188 / 164	2	2
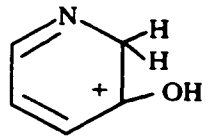	**3bH$^+$**	192 / 170	3	3
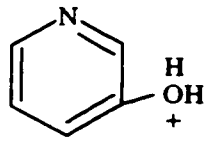	**3gH$^+$**	215 / 219	4	6
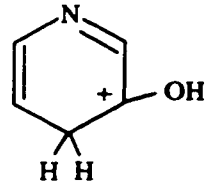	**3dH$^+$**	224 / 197	5	4

Ion Structure	Symbol	Relative Stability MP2 / B3LYP	Ranking MP2	Ranking B3LYP
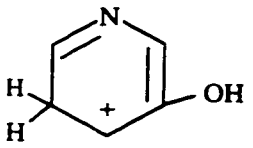	**3eH$^+$**	239 / 209	6	5
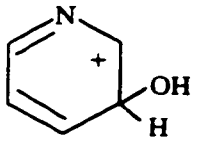	**3cH$^+$**	303 / 276	7	7

Ion Formation and Dissociations:

Precursor cations for the generation of transient radicals were produced by gas-phase protonation of 3-hydroxypyridine (**3**). The protonation exothermicities were defined by the proton affinities (PA) of **3** and those of the reagent conjugate bases[35], methane (544 kJ/mol), water (690 kJ/mol), acetone (812 kJ/mol), and ammonia (854 kJ/mol) (See. Eq. 5).

$$-\Delta H_r = PA(\mathbf{3}) - PA(\text{reagent}) \qquad (5)$$

Since only exothermic protonations are kinetically competitive in ion-molecule reactions in the gas-phase[36], the protonation sites were determined by the proton affinities at each site for **3**. Precursor ions for the formation of **3aH•** were prepared by gas-phase protonation of **3**. According to the proton affinities of the reagent gases and **3**, the proton affinity of **3** at the most basic site was 931 or 946 kJ/mol using either MP2 of B3LYP at the 6-311G(2d,p) basis set respectively. Other sites are shown. (See Figure 6.) Protonation at the most basic site in **3** by either CH_5^+, H_3O^+, $(CH_3)_2COH^+$, or NH_4^+ occurred exothermically by 378, 232, 110 and 69 kJ/mol respectively. Protonation of **3**

with weaker gas-phase acids such as NH_4^+ and $(CH_3)_2COH^+$ are expected to yield a single ion isomer **3aH$^+$**. (See Figure 7) Protonation with H_3O^+ can add a proton to any site except the C3 position. Reaction with CH_5^+ can add a proton to all sites non-selectively. (See Table 2.)

Stable **3H$^+$** ions were obtained in each case and used to generate radicals by collisional electron transfer. The calculated thermodynamic proton affinity of **3** of 931 and 946 kJ/mol by MP2 and B3LYP respectively was the most stable ion **3aH•** and was in reasonable good agreement with the experimental value.[37]

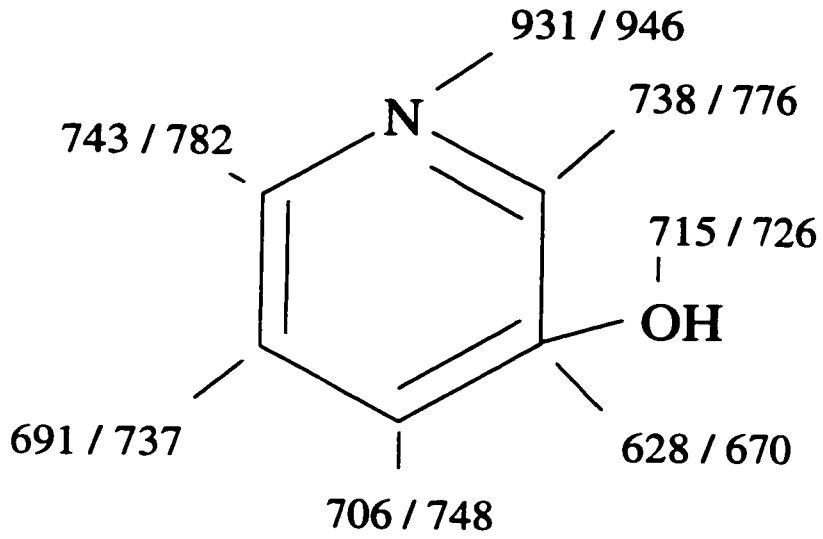

Figure 6. Proton affainities for all sites in **3**. MP2/B3LYP 6-311G(2d,p)

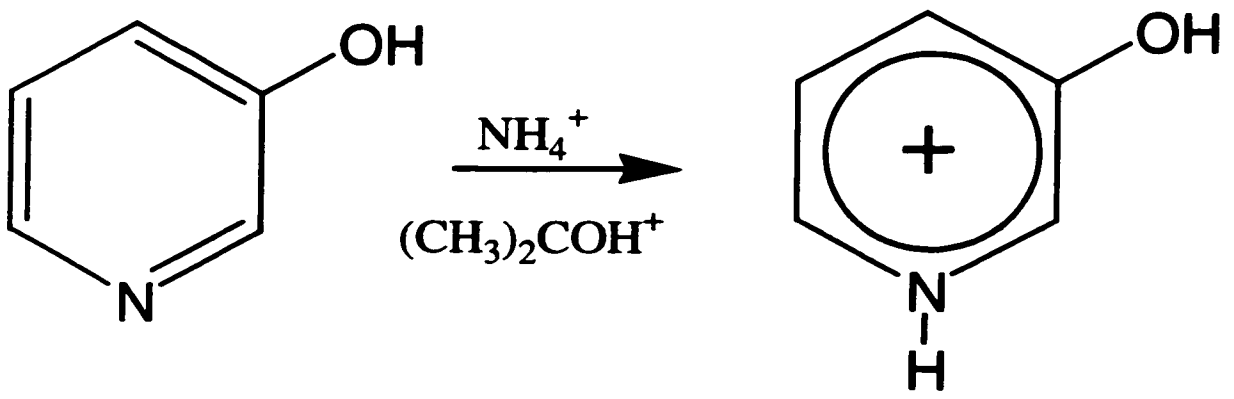

Figure 7. Protonation of **3** with NH_4^+ or $(CH_3)_2COH^+$ to form a single ion product

Table 2. Exothermicity of **3** and various gas- phase acids (kJ/mol) MP2 / B3LYP.

	NH_4^+	$(CH_3)_2COH^+$	H_3O^+	CH_5^+
N-1	78 / 93	119 / 134	234 / 249	380 / 395
C-2	NA	NA	42 / 79	187 / 225
C-3	NA	NA	NA	77 / 119
C-4	NA	NA	9 / 51	155 / 197
C-5	NA	NA	NA / 40	140 / 186
C-6	NA	NA	46 / 85	192 / 231
O-7	NA	NA	18 / 29	164 / 175

NA means the reaction is endothermic, and therefore too slow to occur in the ion source.

Since the NRMS spectra has components of both ionic and neutral dissociations, it is useful to separate the dissociations when possible. The ionic dissociation mechanism is more easily elucidated in partially deuterium labeled species. To elucidate ion dissociations, collisionally activated spectra (CAD) were investigated for **3H**$^+$ by protonation with $(CH_3)_2C\text{-}OH^+$, **3DOH**$^+$ by deuteration with $(CD_3)_2C\text{-}OD^+$, **3HOD**$^+$ by protonation of **3OD** with $(CH_3)_2C\text{-}OH^+$, and **3DOD**$^+$ be deuteration of **3OD** with $(CD_3)_2C\text{-}OD^+$. The major dissociation channels for **3H**$^+$ were loss of H, H_2, OH, H_2O, COH and formation of $C_2H_4N^+$, $C_3H_3^+$, and $HC{=}NH^+$. (See Figure 8). The loss of H from **3H**$^+$ was nonspecific and involved hydrogen atoms from all positions as shown through deuterium labeling. For example, **3DOH**$^+$ showed loss of H/D in 80/20 ratio which indicates involvement of the ring hydrogen atoms. The MIKES-CAD spectra of **3DOD**$^+$ and **3HOD**$^+$ showed statistical losses of H and D from all sites. The elimination of COH from **3H**$^+$ involved the hydroxyl hydrogen, as deduced from deuterium labeling from **3HOD**$^+$. The structure of the resulting $C_4H_5N^{\bullet+}$ ion from **3H**$^+$ was examined by NRMS and gave a spectrum identical with that of pyrrole$^{\bullet+}$.[38] The loss of hydroxyl from **3H**$^+$ involved partial exchange of the OH hydrogen with those of the ring C-H bonds.

In summary, the CAD spectra provides signatures for ion dissociations which can later be distinguished from radical dissociations in the NR spectra. In particular, the ion dissociations were characterized by non-specific loss of hydrogen atom from **3H**$^+$. In addition, small neutral fragments originating from CAD precursor ions were identified.

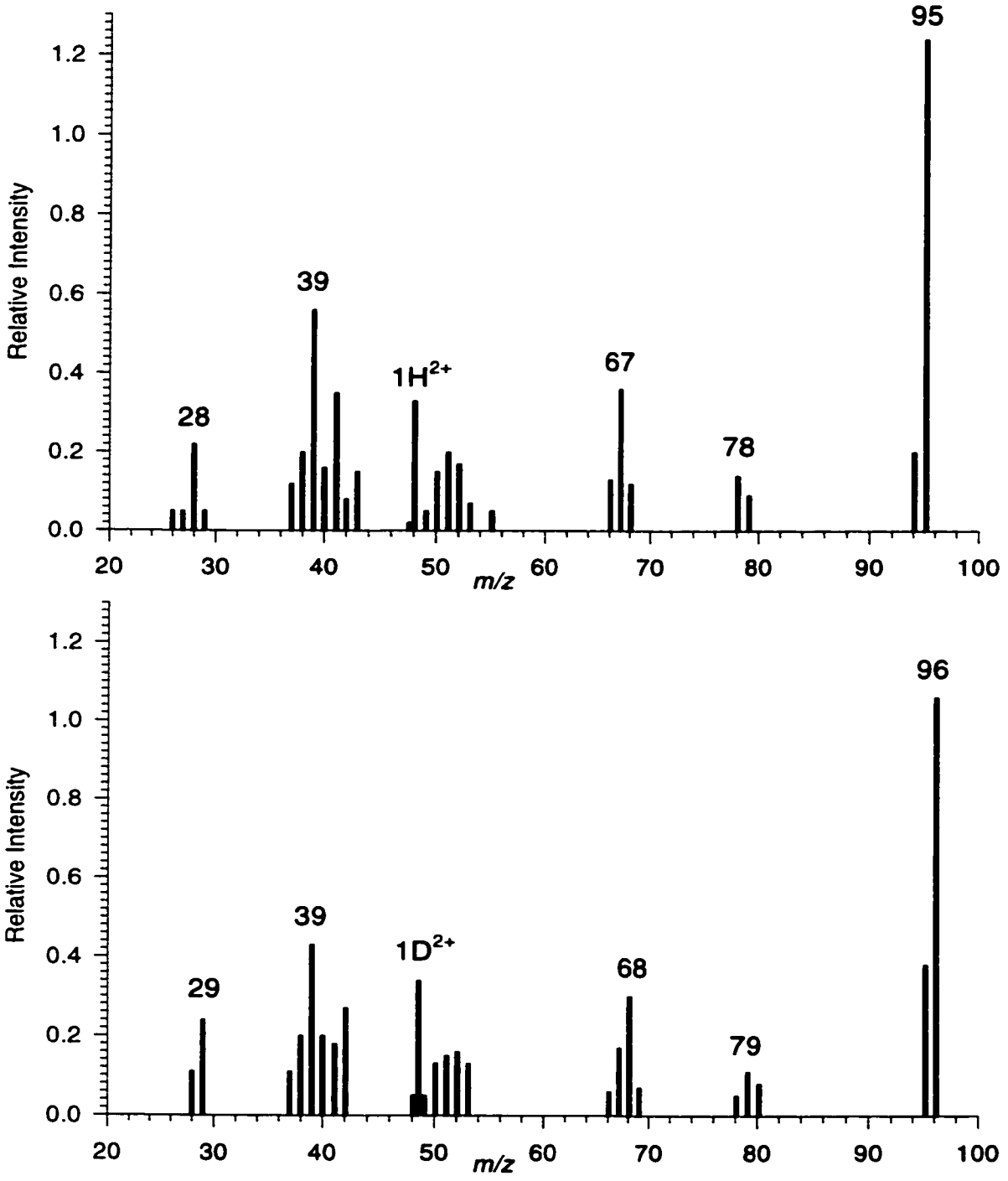

Figure 8. Collision-activated dissociation (CAD) mass spectra of **3aH**$^+$ and **3aDOH**$^+$ at 10 keV ion kinetic energy. Air at 50% ion beam transmittance was used as a collision gas.

Formation and Dissociations of Radicals 3H•:

Ions prepared by protonation of **3** with NH_4^+, $(CH_3)_2COH^+$, H_3O^+, and CH_5^+ were collisional neutralized and studied The NR mass spectra (Figure 9.) showed non-dissociating or survivor ions (*m/z* 95 in a and *m/z* 96 in b and c) which indicated that fractions of intermediate hydroxypyridinium radicals were formed that had lifetimes greater then the flight time between the neutralization and reionization cells (4.67 μs). The relative abundance of the survivor ions correlated with the internal energy of the precursor ion in that the greater internal energy of the precursor ion, the less survivor ion existed. The internal ionic energy is limited by the difference between the proton affinity of **3** and that of the conjugate base of the gas-phase acid (See Table 2.). The NR spectra showed **[3H]** at *m/z* 96 is 2.0, 1.8, 1.1, and 0.6% for precursor ions prepared with NH_4^+, $(CH_3)_2COH^+$, H_3O^+, and CH_5^+ respectively. The dissociations induced by NR were loss of H (*m/z* 95), CO (*m/z* 68), COH (*m/z* 67), and formation of small fragments, C_2H_2/CN (*m/z* 26), CO (*m/z* 28), COH (*m/z* 29), C_3H_3/C_2HN (*m/z* 39) and C_4H_x/C_3NH_y (*m/z* 49-55). Some of these fragments coincide by mass with those from collisionally activated ion dissociations and could occur from ionic dissociations after collisional reionization. However, some dissociations of the intermediate radicals showed distinct mechanisms which could be distinguished by deuterium labeling.

Partial deuterium labeling of **3** showed substantial differences in the NRMS spectra dependent on the site of the deuterium. **3aDOH$^+$** showed a substantial increase in survivor ions over **3aH•**, indicating a strong isotope effect increases the stability of the ions and radicals during the life time of the experiment. **3aHOD$^+$** made by addition of a deuterium by $(CD_3)_2COD^+$ showed a predominant loss of D over H, in ~ 2:1 ratio. **3aDOH$^+$** made from solution exchange with D_2O followed by addition of a hydrogen by $(CH_3)_2COH^+$ showed a substantially different fragmentation. Hydrogen was the predominant loss, by ~ 4:1 ratio. (See Figure 10).

Deuterium labeling of the N and in the hydroxyl group independently revealed the mechanism of hydrogen loss from 3-hydroxypyridinium radicals. Table 3 shows the fractions for losses of H verses D from deuterated ions upon NR. In contrast to ion

dissociations, the NR dissociations showed substantial specificity in the loss of the nitrogen bound hydrogen atom. Loss of H or D from the hydroxyl group was less effective. Approximately 15% of H loss was due to hydrogen loss from ring positions other then the nitrogen site as evidenced by loss of H from **3DOD**$^{+}$.

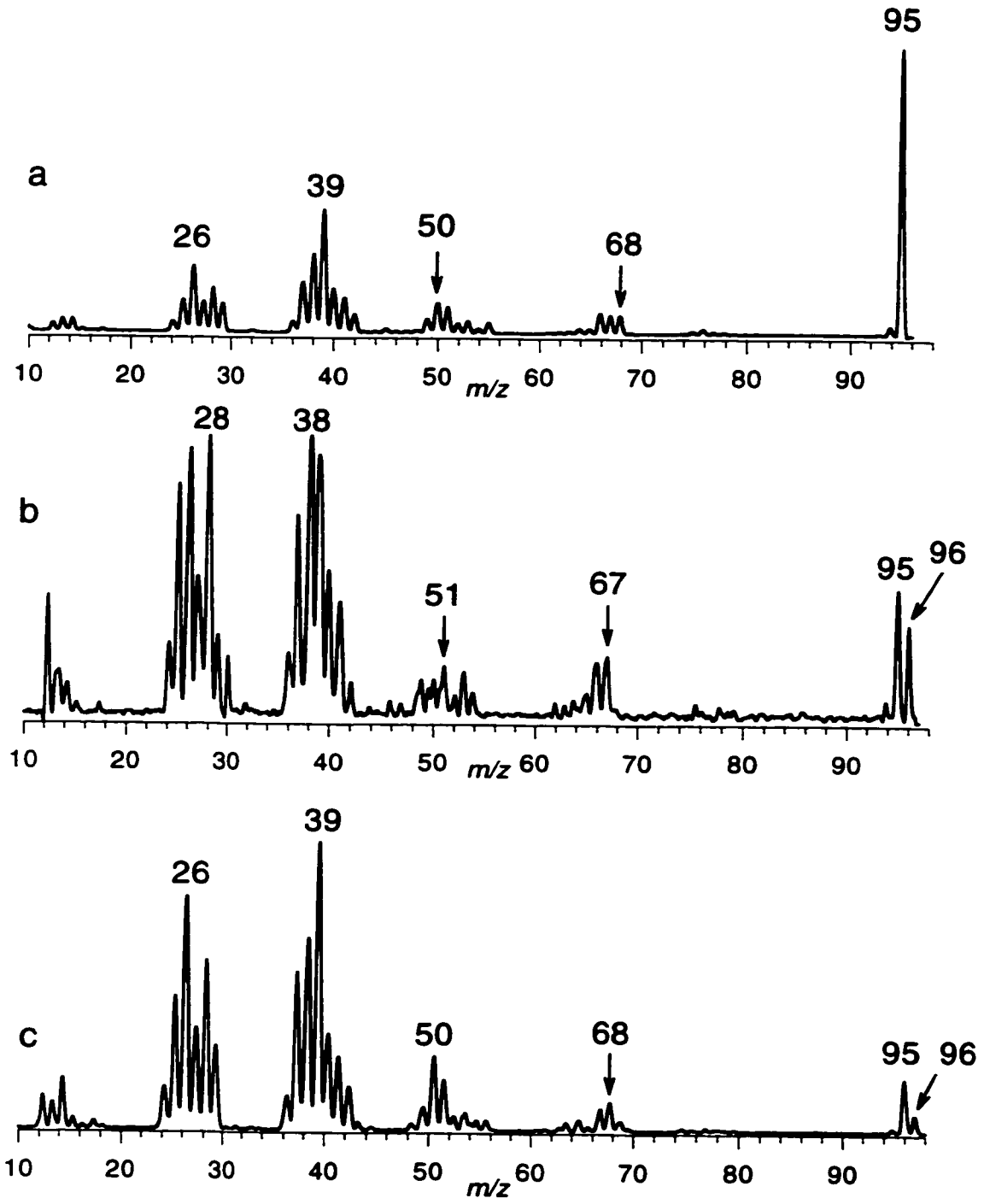

Figure 9. Neutralization (CH_3SSCH_3, 70% transmittance) – reionization (O_2, 70% transmittance) of (a, top) **3**, (b, middle) $\mathbf{3H^+}$ by protonation with NH_4^+, and (c, bottom) $\mathbf{3H^+}$ by protonation with CH_5^+.

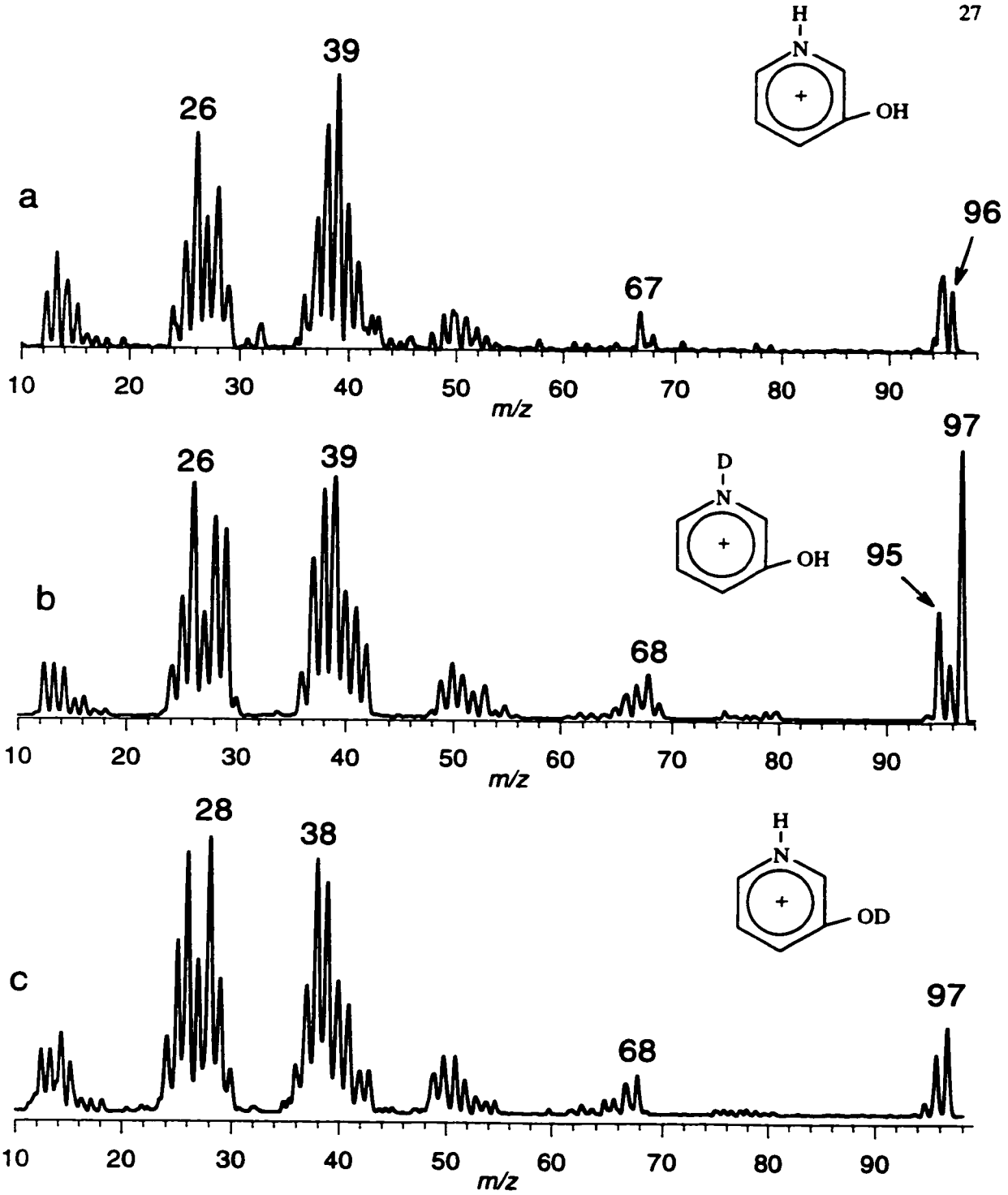

Figure 10. Neutralization (CH_3SSCH_3, 70%T) – reionization (O_2, 70%T) of (a, top) **3H•** by protonation of **3** with $(CH_3)_2C\text{-}OH^+$, (b, middle) **3aDOH$^+$** by protonation of **3** with $(CD_3)_2C\text{-}OD^+$, (c, bottom) **3HOD$^+$** by protonation of **3OD** with $(CH_3)_2C\text{-}OH^+$.

For the selectively labeled ion **3aDOH**$^+$, the specific loss of the nitrogen bound deuterium atom was further increased to 76% upon collisional activation of the intermediate radicals with He. A similar effect was observed for variable-time experiments (See Figure 11) in that the observation time for neutral dissociations was increased from 0.45 to 1.32 μs. Both the extent of (H,D) loss and the **[3aDOH – D] / [3aDOH – H]** (*or m/z* 95 / *m/z* 96 ratios) abundance ratios increased upon allowing longer neutral dissociation while shortening ionic dissociation. The effects of neutral collisional activation and lifetime clearly indicate that the specific loss of D was due to dissociations of neutral **3aDOH•** or its isotopomers.

The NR spectra for **3DOD**$^+$ and **3D**$^+$ formed by addition of a deuterium by D_3O^+ and CD_5^+ also showed predominant loss of D as seen for the system protonated with NH_4^+. (Table 3). Addition of a deuterium by CD_5^+ was sufficiently exothermic to occur non-selectively at all positions to form any ion. Likewise, deuteration with D_3O^+, which was accompanied by OH → OD exchange could produce any ion except **3cD**$^+$ at *m/z* 98. Collisional neutralization of these ring labeled ions, followed by dissociations of the radical intermediates, would be expected to yield greater loss of H than that seen. For example, suppose the C-4 position of **3** has a deuterium added so the C-3 site has both a hydrogen and deuterium. Loss from this position, barring any isotope effects would result in ~ 50/50 ratios for loss of H/D since the H and D atoms in these radicals would be chemically equivalent. However, the loss of H would be preferred by a primary isotope effect making this ratio even greater. The fact this was NOT observed presents evidence that isomers other then **3aDOH** $^+$ were not present as major components in the ion beam used for collisional neutralization. A likely explanation is that less stable ions isomers formed by exothermic protonation with CH_5^+ or H_3O^+ were depleted by ion-molecule reactions with neutral **3** present in the ion source. Ion trajectory simulations indicated that the ions underwent an average of 40-50 collisions in the ion source which should facilitate exothermic proton transfer from the less stable isomer to form **3aDOH** $^+$.

Table 3. Summary of NRMS data.

Protonation Reagent	Ion Structure	Loss of D / H	
		-D %	-H
ND_4^+	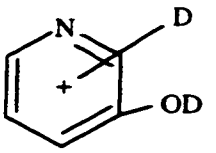	85	15
$(CD_3)_2COD^+$ (from acetone d-6)	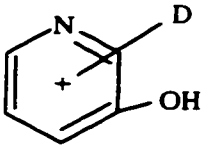	65 76_{NCR}	35 24_{NCR}
$(CH_3)_2COH^+$	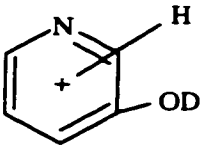	14	86
D_3O^+ (from D_2O)	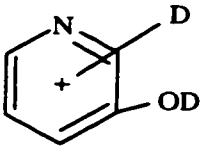	84	16
CD_5^+ (from CD_4)	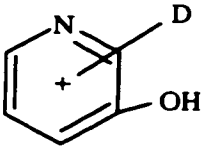	69	31
CH_5^+	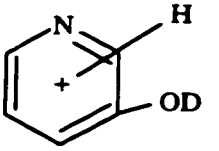	9	91

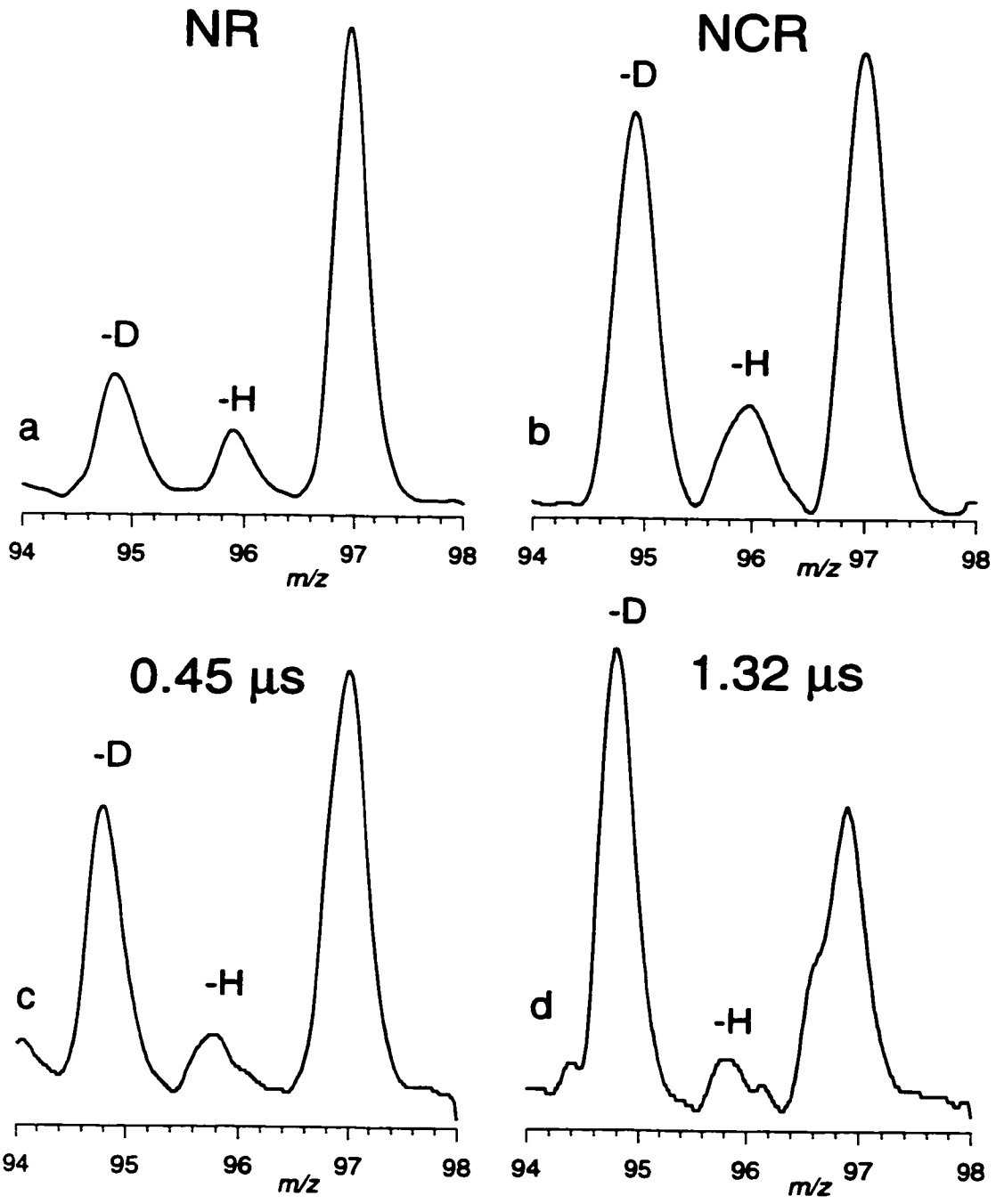

Figure 11. Top. Neutralization- Collisional-Activation-Reionization (NCR) with 50% T He in the conduit region. Bottom. Neutralization-Reionization (NR). No helium is present in the conduit region.

Radical Energetics:

To further investigate **3aH•**, *ab initio* and DFT calculations were used to study the relative energies of radicals **3aH•** - **3gH•** in the ground electronic and excited states. RRKM calculations were used to investigate the dissociation kinetics as well as isotope effects of the radicals.

Geometries of radicals **3aH•** - **3fH•** as well as open ring products and transition states were optimized with the UHF/6-31G(d,p) basis set. (See Figure 12) An attempted geometry optimization of **7gH•** resulted in an exothermic dissociation to **3** and a hydrogen atom. This indicates that at this level of theory, **3gH•** is not expected to be stable. MP2 and B3LYP calculations agree that **3aH•** is the most stable isomer of the (**3** + H)• adducts. (See Table 4) The energy difference between **3aH•** and the least stable isomer (**3cH•**) as 53 kJ/mol. The energy differences were smaller for $H^{\bullet}$ addition than H^{+} addition indicating $H^{\bullet}$ is less site specific than H^{+}.

Since the radicals are formed by collisional neutralization of corresponding ions, the radical may be able to gain vibrational energy by Franck-Condon effects due to a mismatch between the geometry of the radical and ion. To be able to correctly assess the energy imparted into the radical to understand dissociation pathways, the Franck-Condon energy must be determined.

Franck-Condon energies for vertical neutralization and ionization were calculated for **3aH•**, **3bH•**, and **3aH^{+}**. Vertical electron capture in the $v^{1} = 0$ state of **3aH^{+}** formed **3aH•** with 27 kJ/mol of vibrational energy. Vertical ionization of the $v^{1} = 0$ state of **3aH•** formed ion **3aH^{+}** with 45 kJ/mol of vibrational energy. Vertical electron capture in vibrationally relaxed **3bH^{+}** formed radical **3bH•** with 36 kJ/mol of vibrational energy. This shows the Franck-Condon energy due to vertical ionization of **3aH•** and neutralization of **3aH^{+}** and **3bH^{+}** is only moderate.

Table 4. Radical structures and relative stabilities for protonated 3-hydroxypyridine (**3**)

Radical Structure	Symbol	Relative Stability UMP2 / B3LYP	Ranking UMP2	Ranking B3LYP
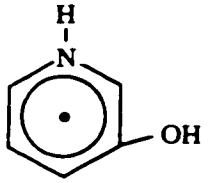	3aH•	0 / 0	1	1
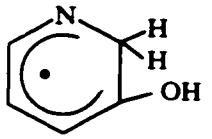	3bH•	9 / 8	2	2
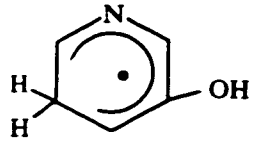	3eH•	14 / 21	3	4
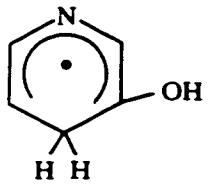	3dH•	16 / 16	4	3
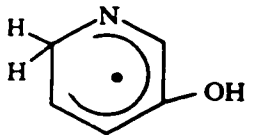	3fH•	21 / 22	5	5
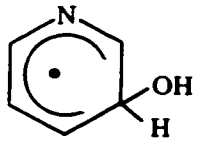	3cH•	43 / 53	6	6

Oftentimes, there are energy barriers associated with ring cleavage or hydrogen dissociations as the electrons in a given bond must reorganize to form the new products. The height of these energy barriers can give insight into certain dissociations above the thermochemical threshold. The dissociation of the N-H bond in **3aH•** was investigated by stepwise energy calculations along the reaction coordinate. A transition state (**TS1**) was located at d(N-H) = 1.568 Å. Single point calculations and zero-point energy corrections gave the 0 K energy of **TS1** as 126 kJ/mol above **3aH•**. The bond dissociation energy, **3aH•** → 3 + H• was 99 and 102 kJ/mol at 0 K and 298 K respectively. Therefore, the energy barrier for the addition of a hydrogen atom to nitrogen in **3** was ~ 27 kJ/mol. (See Figure 14)

Other unimolecular reactions of **3aH•** required substantial potential energy barriers as seen for **TS1**. Hydrogen atom migration from N1 to C2 to form **3bH•** required 174 kJ/mol above **3aH•** in the transition state (**TS2**) while cleavage of the N1-C2 bond in **3aH•** forming an open ring radical was 223 kJ/mol endothermic at 0 K.

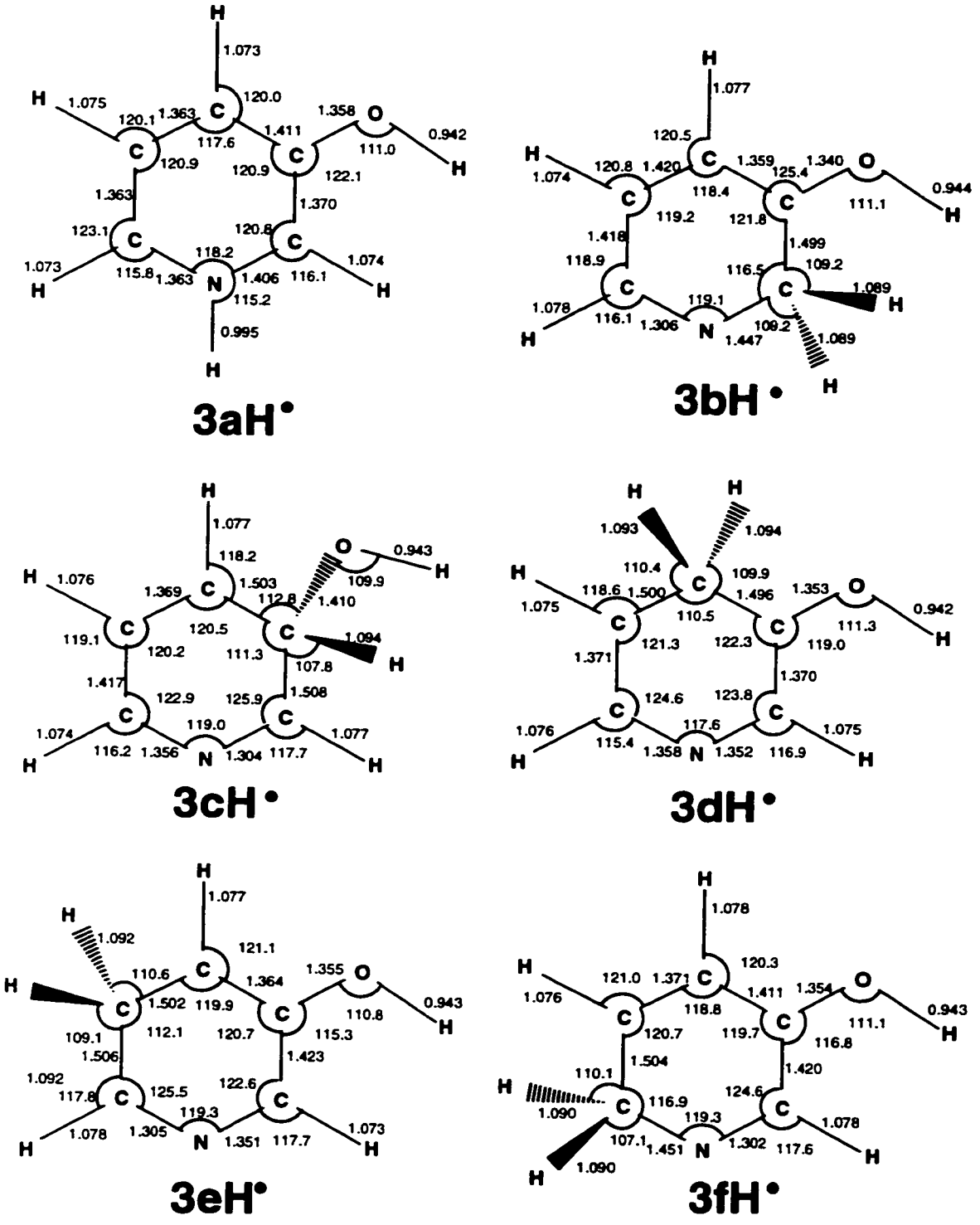

Figure 12. RHF/6-31G(d,p) optimized structure of **3aH•** - **3fH•**.

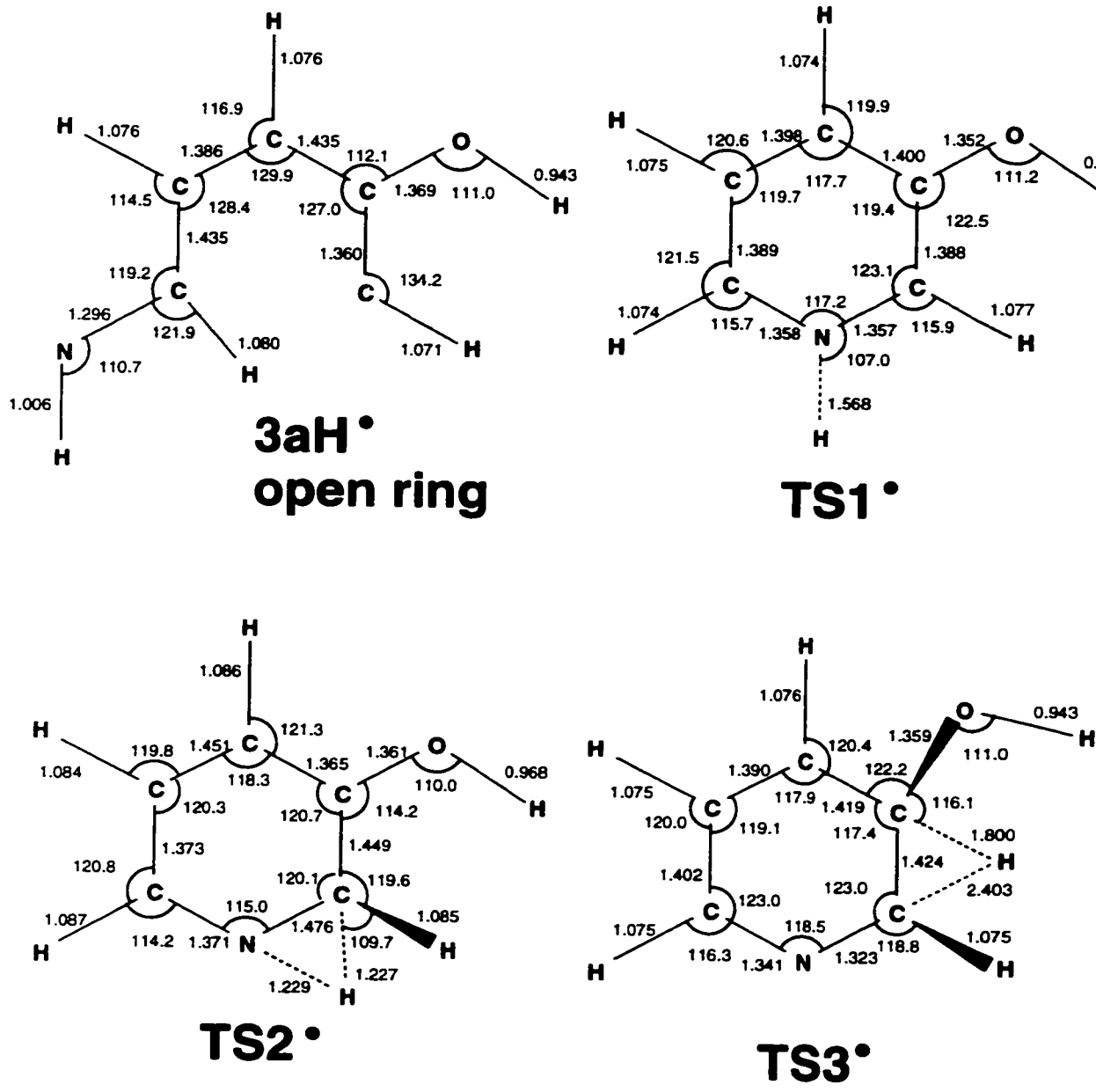

Figure 13. RHF/6-31G(d,p) optimized structures for a ring opening and transition states

Since the open ring radical was a local energy minimum, it must be separated from the more stable **3aH•** by an additional potential energy barrier. Hence, a ring cleavage in **3aH•** en route to formation of C_2H_2, C_3H_3, and C_2H_4N was a high-energy process. A high threshold energy was also calculated for the extraction of •C-OH to form pyrrole, which would require 256 kJ/mol above **3aH•** at 0 K.

Loss of hydroxyl from **3aH•** to give pyridine was the only dissociation that had a thermochemical threshold (103 kJ/mol at 0 K) comparable to that for loss of H. However, the formation of pyridine required prior hydrogen migrations, such as **3aH•** → **3bH•** → **3cH•** which both had substantial potential energy barriers. The hydrogen migration for the **3bH•** → **3cH•** isomerization (**TS3**) was calculated at 140 kJ/mol above **3aH•**. A direct loss •OH from **3aH•** would produce azacyclohexatriene-3-ylidene (pyridine 3-ylide) which is expected to be about 200 kJ/mol less stable than pyridine by analogy with pyridine 2-ylide.[39] Hence, cleavage of the N-H bond was by far the lowest-energy dissociation of **3aH•**.

The potential energy diagram in Fig. 13 also allowed as assessment of radical additions to pyridine and **3** in addition to dissociation pathways. Addition of •OH to C3 in pyridine was a barrierless process at the present level of theory. Although a transition state for the addition was located by UHF/6-31G(d,p) calculations, single-point energies at the Hartee-Fock saddle point were slightly lower than the combined energies of the pyridine and •OH. This result was consistent with previous observations that •OH is added to C-3 in pyridine determined by pulse radiolysis.[40] A further isomerization of **3cH•** → **3bH•** required a barrier of 92 kJ/mol. This barrier is substantially higher than the thresholds for both the reverse dissociation of **3cH•** to pyridine and •OH and the loss of a hydrogen atom to form **3** (51 kJ/mol). The high energy barrier should make the **3cH•** → **3bH•** isomerization inefficient except at high thermal energies. It should be noted that loss of H-3 from **3cH•** probably also had an activation barrier by analogy with the similar dissociation of the 4-amino-(4H) pyridinium radical.[33] The loss of H from **3cH•** can therefore be slow enough to compete with collisional cooling provided the reaction

occurred in a condensed state. Consequently, **3cH•** may be a detectable intermediate of •OH addition to pyridine.

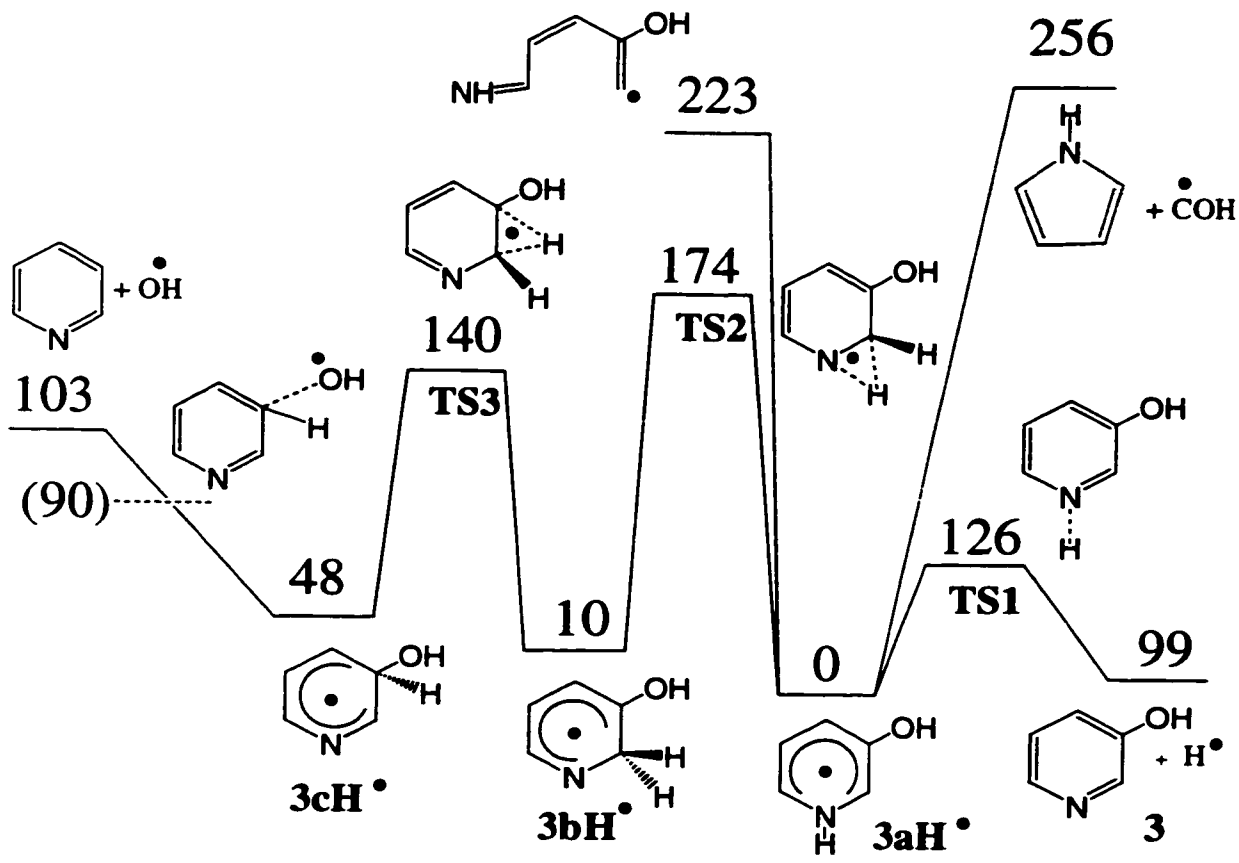

Fig 14. Potential energy diagram

Dissociation Kinetics:

The kinetics of **3aH•** and **3aD•** dissociations and isomerizations were investigated with RRKM calculations. The MP2 and B3LYP averaged energy barriers were used. The absolute values of the unimolecular rate constants (k_{uni}) are known to depend strongly on the critical energies used. However, the relative values are generally

less susceptible to offsets of potential energy.[41] Of particular interest were a) the relative rates of hydrogen atom loss in **3aH•** versus isomerization to **3bH•**, b) the magnitude of the primary isotope effect on the dissociations of the N-H and N-D bonds in **3aH•** and **3aD•** respectively and c) the higher-order isotope effects on the dissociation of the N-H bonds in **3aH•** and **3aHOD•**. The calculated $k_{uni}(E)$ are shown in Figure 15. The $k(E)$ curves for the N-H and N-D bond dissociations showed shallow slopes near the dissociation threshold. For the experimental radical lifetimes of 4.67 μs, 50% dissociation was achieved at log k_{uni} = 5.17 as shown in Figure 15. This required kinetic shifts[42] of 35, 36 and 41 kJ/mol for **3aH•**, **3aHOD•**, and **3aDOD•** respectively, which increased the kinetic stability of the radicals on the time scale of the NRMS measurements.

The $k(E)$ curves further showed that the **3aH•** → **3bH•** isomerization was at least 2-3 orders of magnitude slower than the loss of H or D at all relevant internal energies of **3aH•** and **3aD•**. This implies that dissociating **3aD•** could NOT undergo a competitive rearrangement to **3bD•**. Since **3bD•** has both a hydrogen and a deuterium bound to the C2 position, it would be expected that barring an inverse isotope effect, **3bD•** would eliminate both hydrogen and deuterium from this site. However, the loss of deuterium from **3aD•** would be expected to be nearly 100% specific since isomerization is not energetically feasible. The loss of hydrogen as observed from the NRMS spectrum must be entirely due to nonspecific ion dissociations following reionization. Available thermochemical data[43] places the threshold energy for the loss of H from **3aH$^+$** at 505 kJ/mol above that of **3aH$^+$**. This is substantially higher than the energy barriers for proton migrations in aromatic ions (< 150 kJ/mol).[44] Therefore, **3aH$^+$** having sufficient internal energy to dissociate would also be expected to have enough energy to undergo extensive scrambling of hydrogen atoms prior to loss of H, as observed in the CAD spectrum.

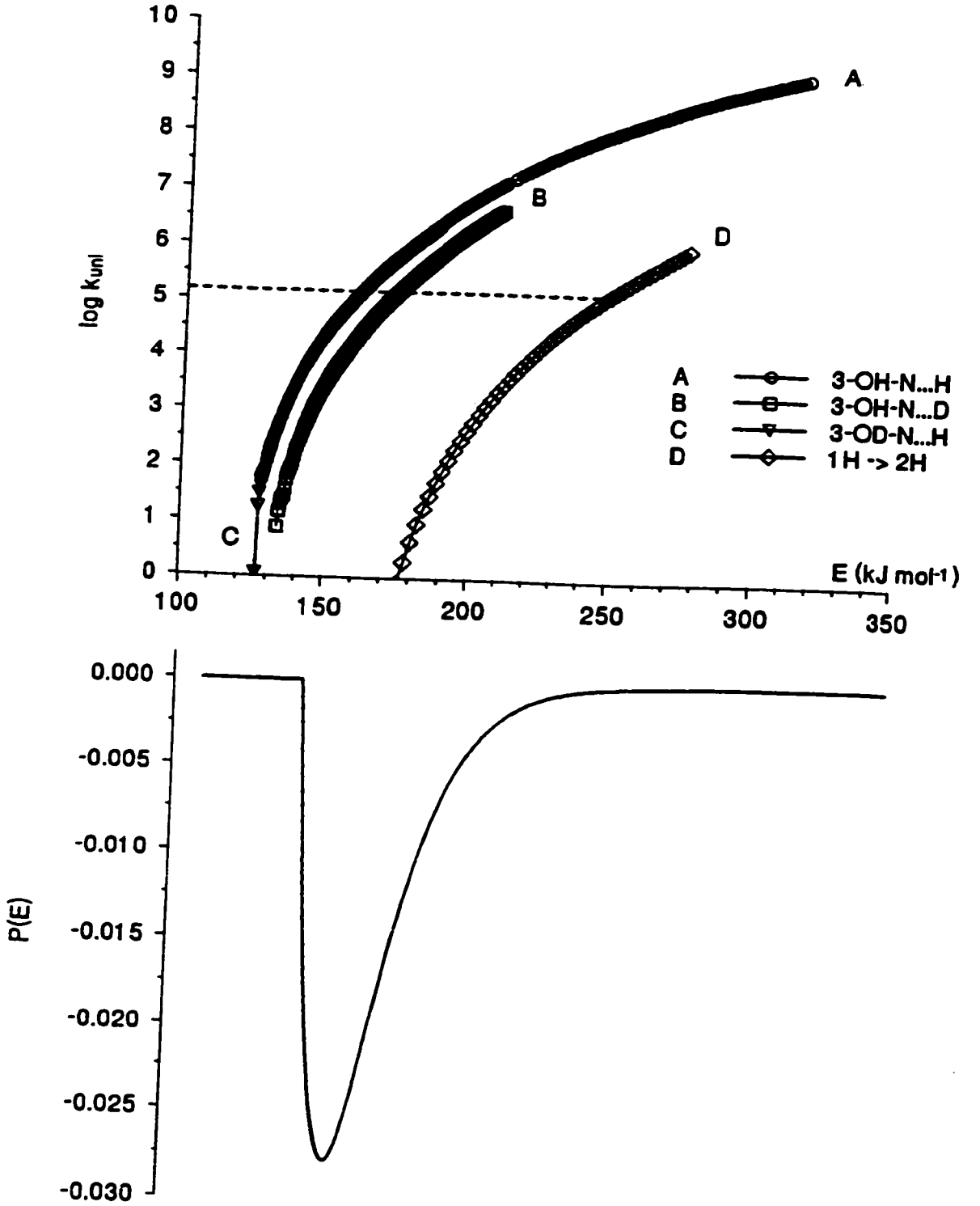

Figure 15. Top: RRKM calculated unimolecular rate constant for N-(H,D) bond dissociation of **3aH•**, **3aHOD•**, **3aD•**, and **3aH•** → **3bH•** isomerization. The broken line shows log *k* for 50% dissociation. Bottom: Best fit internal energy distribution function for **3aH•**.

The k(E) curves indicated substantial primary isotope effects from the loss of D from **3aDOD•**. In contrast, the effects of OD on the loss of H from **3aHOD•** were negligible. (Figure 15) The kinetic effects can be described[45] by eq. 6 and 7 where the energy distributions in **3aD•** and **3aH•** ($P_H(E)$ and $P_D(E)$) were approximated by a single P(E) function (eq.8).

$$[\mathbf{3aH\bullet}] = \{[\mathbf{3aH\bullet}] + [\mathbf{3aH\bullet} - H]\} \int P_H(E)e^{-k_H(E)\tau}dE \quad (6)$$

$$[\mathbf{3aDOD\bullet}] = \{[\mathbf{3aDOD\bullet}] + [\mathbf{3aDOD\bullet} - D]\} \int P_D(E)e^{-k_D(E)\tau}dE \quad (7)$$

$$P(E) = \frac{4(E-E_0)\,e^{-2(E-E_0)/W}}{W^2} \quad (8)$$

Equations 6 and 7 made it possible to fit the experimental **[3aH•]** / **[3aH•** - H] and [**3aD•**] / [**3aD•** -D] abundance ratios with the calculated k_H(E) and k_D(E) by using the dissociation times τ = 4.67 and 4.70 μs for **3aH•** and **3aD•** respectively and a P(E) function (eq. 8), where E_0 = 145 kJ /mol was an energy shift and W = 26.5 kJ/mol was the width parameter. Applying the P(E) function from eq 8 showed: **[3aH•]** / **[3aH•** - H] = 0.48 (calculated), 0.49 (measured); and **[3aD•]** / **[3aD•** -D] = 1.45 (calculated), 1.49 (measured). The best-fit distribution function showed a maximum at 158 kJ/mol and a full width at half-maximum of 33 kJ/mol. (Figure 15). These properties were reasonable as shown by the following analysis. The internal energy of **3aH•** was composed of both the internal energy of the precursor ion (**3aH$^+$**) and the Franck-Condon energy in vertical electron transfer. Protonation of **3** with $(CH_3)_2C\text{-}OH^+$ was 110 kJ/mol exothermic, but only ~85% of the excess reaction energy went into the ion, as predicted by the reaction dynamics simulations of Uggerud.[46] The internal energy in **3aH$^+$** was therefore composed of the vibrational energy of **3** (38 kJ/mol at 473 K) and the fraction of protonation exothermicity, 0.85 × 110 = 94 kJ/mol. This is an upper bound for the internal energy of the ion since the ion underwent several cooling collisions with acetone molecules in the ion source making the percentage of energy impartted to the ion less than 85%. The

Franck-Condon energy in vertical neutralization of **3aH**$^+$ was calculated as 27 kJ/mol. The upper bound for the mean internal energy in **3aH•** was therefore 38 + 94 + 27 = 159 kJ/mol, which compared favorably with the maximum of the fitted P(E) function (158 kJ/mol).

Other types of energy distribution functions were also tried but could not predict an experimentally reasonable energy. Symmetrical (Gaussian) and inverted Boltzmann-like P(E) functions could roughly fit the experimental data only when assuming distribution maxima at energies between 210 and 230 kJ/mol. Such energy distributions were difficult to justify on the basis of the ion and electron-transfer energetics.

Since energetically and kinetically the major dissociation pathway expected from **3aH•** is loss of H, it is surprising that the NRMS spectra showed such predominant ring cleavages. Ring fragmentations can occur competitively with hydrogen dissociations in **3aH•** above 230 kJ/mol of internal energy, from **3** formed by loss of H, and/or in **3**$^{+\bullet}$ and **3aH**$^+$ following collisional reionization. However, both **3** and **3aH**$^+$ were substantially stable, as shown by the strong survivor ion in the NR spectrums of **3** and **3aH**$^+$ the latter, which showed a very abundant survivor ion, [**3aH**$^+$] = (25%) (Figure 9). To promote ring cleavage in **3aH**$^+$ formed by the **3aH•** → **3** → **3**$^{+\bullet}$ → reaction sequence would require that the energy driving these dissociations be carried over from highly energetic **3** formed by dissociation of excited **3aH•**. However, this was incompatible with the analysis of isotope effects on loss of H, which indicated internal energies in dissociating **3aH•** would form **3** with ~30 kJ/mol of average internal energy. This is significantly less than what would be needed to drive ring cleavages. It therefore appeared that the occurrence of ring cleavages upon NR cannot be logically explained by consecutive dissociations, e.g., **3aH•** → **3** → **3**$^{+\bullet}$ ring fragments, but must be due to competitive dissociations in **3aH•**. Since the potential energy surface of the ground electronic state of **3aH•** favored loss of H, the more endothermic ring cleavages must not have occurred in the ground state, but rather must have occurred on the surface of an excited state.[47]

Excited States:

The energetics of the lowest excited states of **3aH•** were addressed by Configuration Interaction Singles (CIS/6-311G(2d,p)) calculations.[48] Out of the five excited states investigated, the lowest two states in **3aH•**, A and B, were due to excitation of the odd electron from the 26α SOMO. The CIS wave function for the A state is shown in Figure 16, and the B state was described by $= 0.908(27\alpha) - 0.303(28\alpha)$. These outer excited states can be formed directly by electron transfer to **3aH$^+$**, whereby the electron is captured within the virtual orbitals of the ion. Both the A and B electronic states had low oscillator strengths for radiative transitions to the ground (X) state, as shown for the A state in Figure 16, which also depicts the calculated adiabatic and vertical ionization energies of **3aH•**. The calculated radiative lifetimes for the A and B states, $\tau_{ij} = 1/A_{ij}$, where A_{ij} is the Einstein coefficient, were 0.4 and 3.4 μs for the A → X and B → X transitions, respectively. Hence, the states were sufficiently long-lived to undergo dissociations or internal conversion to a highly vibrationally excited ground electronic state **3aH•**. The excitation-deexcitation of the A and B states showed substantial Franck-Condon effects. Those for the A state are summarized in Figure 16. For the B state the X → B excitation of relaxed **3aH•** required 4.80 eV, while excitation of (X)**3aH•** formed by vertical neutralization of **3aH$^+$** required 3.7 eV. This suggested that the potential energy surfaces of the A and B states were shifted with respect to that of the X state. Such shifts should favor internal conversion to form the vibrationally hot X state because of the proximity of the potential energy surfaces.[49] It is currently unknown whether ring cleavages occurred adiabatically in electronic excited states of **3aH•** or in a vibrationally hot ground state. It is also conceivable but not proven that the electronic energy in the A or B state can be used to produce an open-ring photoisomer of **3aH•** which will then dissociate extensively upon collisional ionization. Although the details of energy storage and conversion in **3aH•** remain to be elucidated, the existence of long-lived outer excited electronic states of **3aH•** provides a mechanism for the formation of high-energy **3aH•** in which ring cleavages are energetically possible.

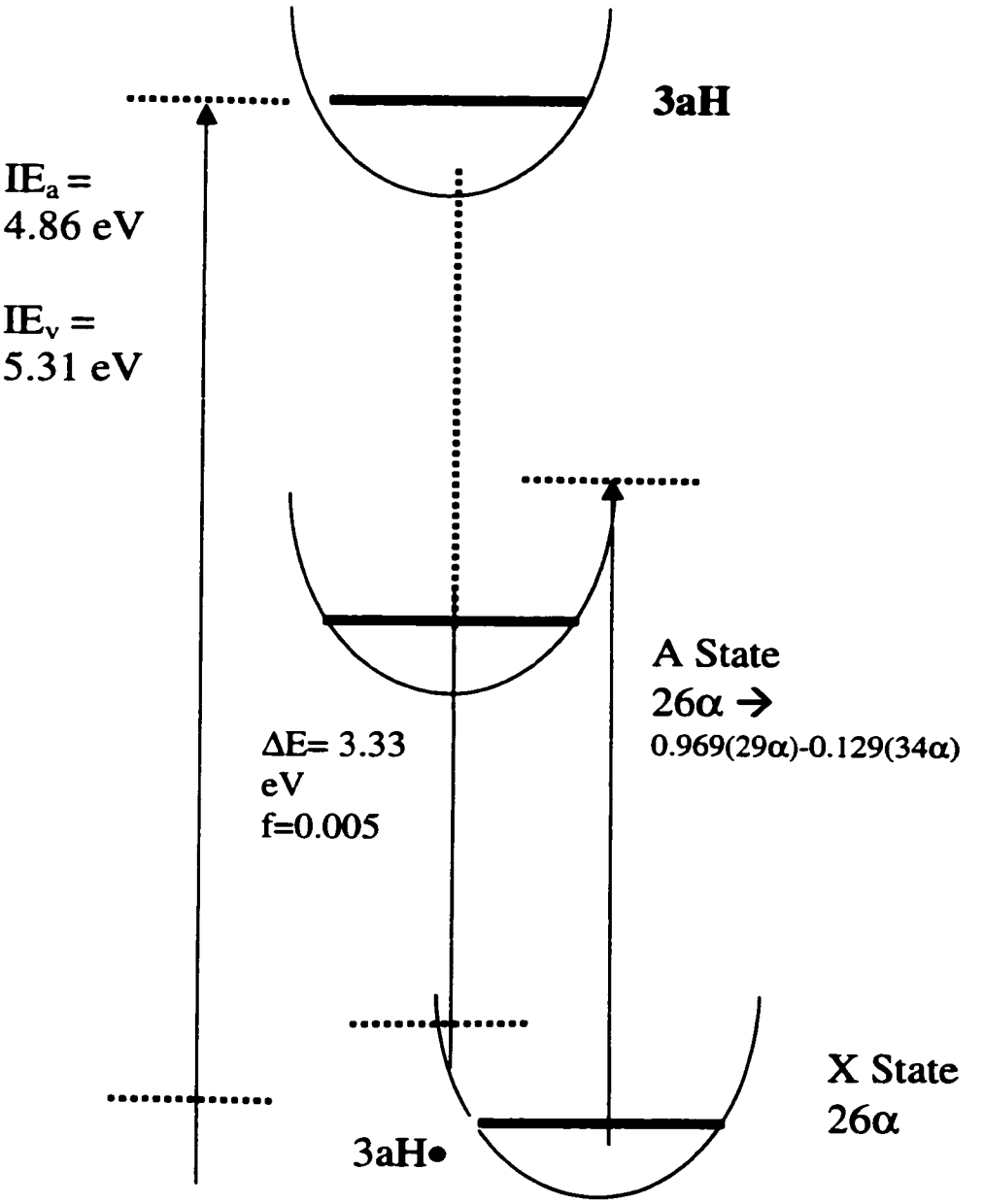

Figure 16. Potential energy diagram for ionization and X → A electronic excitation in **3aH•**. Excitation energies and oscillator strengths are from CIS/6-311G(2d,p) calculations. Ionization energies are from averaged PMP2 + B3LYP/6-311G(2d,p) calculations.

Conclusions:

3-Hydroxy-(1H)-pyridinium radical (**3aH•**) was the most stable isomer of the hydrogen atom adducts to 3-hydroxypyridine. Radical **3aH•** was formed as a stable species by vertical neutralization of cation $\mathbf{3aH^+}$. Loss of hydrogen atom from **3aH•** was the lowest-energy dissociation. In the gas phase this dissociation showed a substantial kinetic shift and primary deuterium isotope effect that increased the kinetic stability of **3aH•** and **3aD•**. Ring-cleavage dissociations of **3aH•** were substantially more endothermic than loss of hydrogen atom and could proceed competitively in **3aH•** formed in excited electronic states. Other hydrogen atom adducts to the pyridine nucleus in 3-hydroxypyridine were calculated to be stable radicals that required substantial energy barriers to isomerizations by 1,2-hydrogen atom migrations.

Chapter IV. 2-Hydroxypyridine

Once the 3-hydroxypyridine (**3**) system was studied by experimental and theoretical methods, the more complex 2-hydroxypyridine (**1**) and 2-(1H)pyridone (**2**) system was investigated to further understand the gas phase tautomerization of the **1,2** system. The work from this chapter has been previously published in *J. Phys. Chem. A* **1999**, 103, 6268.

Numerous ion and radical structures are discussed in the following text. For clarity, a system has been developed. 2-Hydroxypyridine, 2-(1H)pyridone, and 3-hydroxypyridine are referred to as **1,2,3**, respectively. $\mathbf{1}^+$, $\mathbf{2}^+$, and $\mathbf{3}^+$ refers ions of **1,2**, and **3**, whereas radicals are **1•**, **2•**, and **3•**. Protonated ions are referenced as $\mathbf{1aH}^+$, where **1** refers to 2-hydroxypyridine, the **H** refers to protonation with an H atom, the charge designates an ion, and **a** refers to position where the proton resides. The **a** refers to protonation at the nitrogen, **b,c,d,e**, and **f** refer to the ring positions C2, C3, C4, C5 and C6 respectively. The **g** refers to the oxygen position. To refer to a radical, the charge has been replaced by a dot (i.e. **2aH•**), and to indicate the addition of a deuterium, the H has been replaced by a D (i.e. $\mathbf{2aD}^+$). It should be noted that **2** can not be protonated at the C2 site, so an ion or radical does not exist with a proton residing at the C2 position. In the cases of radicals and ions which have both hydrogen and oxygen incorporated in the molecule, the OH or OD position is referred to explicitly. For example, **1aHOD•** indicates the same radical as **1aH•** except the OH position has been labeled with a deuterium.

Every calculation was performed with both *ab initio* theory and density functional theory. Both energies are reported, with the *ab initio* calculation always reported first (e.g. 323/346 kJ/mol). This corresponds to MP2 / B3LYP. Unless otherwise indicated, the basis set is 6-311G(2d,p).

Abstract:

Isomeric radicals corresponding to hydrogen atom adducts to 2-hydroxypyridine (**1**) and 2-(1H)pyridone (**2**) were investigated using neutralization-reionization mass spectrometry and combined *ab initio* and density functional theory (DFT) calculations. Gas-phase protonation of **1** and **2** occurred preferentially at the nitrogen and oxygen atoms respectively to give a single 2-hydroxypyridinium ion product. These ions (**1aH**$^+$ or **2gH**$^+$) are identical but for simplicity, **1aH**$^+$ will be used exclusively hereafter. The calculated topical proton in **1** were 922, 602, 777, 649, 786, 694, and 746 kJ/mol for the N1, C2, C3, C4, C5, C6, and OH positions respectively. The topical proton affinities in **2** were 756, 824, 815, 692, and 930 kJ/mol for the N1, C3, C5 and C6, and carbonyl oxygen positions, respectively. The 2-hydroxy-(1H)pyridinium radical (**1aH•**) was generated by collisional neutralization of **1aH**$^+$ and found to be stable on the 4.67 μs time scale. Radical **1aH•** dissociated by losses of the hydroxyl and amine hydrogen atoms, and by ring cleavages. MP2 and B3LYP calculations with the 6-311G(2d,p) basis set established the 298K relative energies of hydrogen atom adducts derived from **1,2** as **2cH•** (most stable, 0), < **2fH•**(+20) < **1cH•** (+37) < **2dH•** (+59) < **2eH•** (+60) < **1eH•** (+62) < **1aH•** (+67) < **1fH•** (+76) < **1dH•** (+86) < **1bH•** (+107) < **2aH•** (+139 kJ/mol). The radicals **2bH•** and **1gH•** were found to be unstable and dissociated by ring openings and loss of H respectively. RRKM calculations on the effective QCISD(T)/6-311+G(2d,p) potential energy surface showed cleavages of the O-H and N-H bonds in **1aH•** to be the lowest energy dissociations occurring in an ~10:1 ratio. **1** was calculated to be 4.7 kJ/mol more stable then **2** in the gas phase at 0K. Fitting the experimental and calculated isotope effects for the dissociations seen from deuterium labeled radicals yielded a distribution function for the internal energy in the ground electronic state of **1aH•** formed by collisional electron transfer. The maximum of the internal energy distribution in the ground state **1aH•** (129 kJ/mol) was found to be expressed accurately by a combination of the internal energy of the precursor ion and the Franck-Condon energy gained upon vertical electron transfer. The three lowest excited electronic states in **1aH•** were found by CIS/6-311G(2d,p) calculations to be outer states resulting from

excitation of the unpaired electron in **1aH•** or electron capture in **1aH$^+$**. The energetics and radiative lifetimes of the outer excited states in **1aH•** allowed interpretation of the highly endothermic ring-cleavage dissociations seen in the NRMS spectra. The unimolecular chemistry of **1aH•** can be explained by a bimodal energy distribution due to a combination of the ground and excited electronic states upon femtosecond collisional electron transfer.

Results and Discussion

Ion Stability:

The ions of **1,2** were investigated using MP2 and B3LYP calculations at the 6-311G(2d,p) basis set. The results are shown in Table 5. The most stable ion from both sets of calculations was that of **1aH$^+$** by over 100 kJ/mol. This is similar to the trend seen for the **3** system which also had a broad range of ion energetics. The trends for ion stabilities remain constant until the 6th and 7th in the series, where PMP2 predicts the **1gH$^+$** ion to be more stable then the **2aH$^+$**, whereas B3LYP reverses this.

Table 5. Ion Stabilities of **1,2**

Ion Structure	Symbol	Relative Stability MP2 / B3LYP	Ranking MP2	Ranking B3LYP
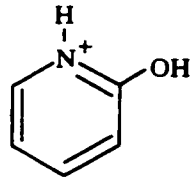	**1aH$^+$**	0 / 0	1	1
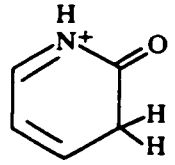	**2cH$^+$**	112 / 100	2	2
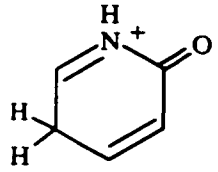	**2eH$^+$**	118 / 113	3	3
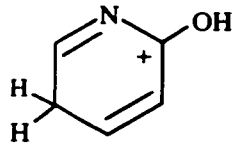	**1eH$^+$**	145 / 128	4	4

Ion Structure	Symbol	Relative Stability MP2 / B3LYP	Ranking MP2	Ranking B3LYP
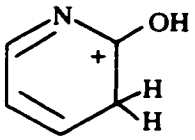	**1cH$^+$**	155 / 136	5	5
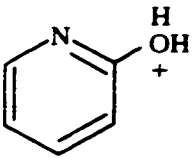	**1gH$^+$**	170 / 183	6	7
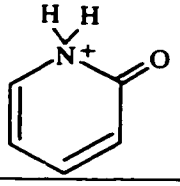	**2aH$^+$**	174 / 173	7	6
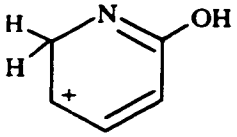	**1fH$^+$**	240 / 217	8	8
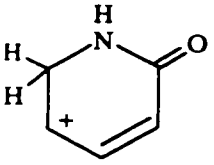	**2fH$^+$**	252 / 222	9	9
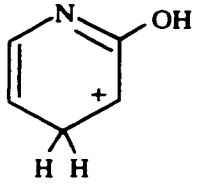	**1dH$^+$**	283 / 265	10	10
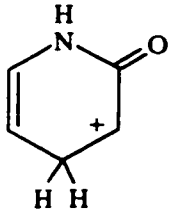	**2dH$^+$**	283 / 265	11	11
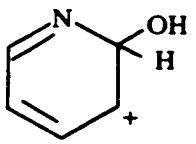	**1bH$^+$**	331 / 311	12	12

Ion Formation and Dissociation:

Precursor cations for the generation of transient radicals were produced by gas-phase protonation of 2-hydroxypyridine consisting of a mixture of **1** and **2**. The protonation exothermicities were defined by the proton affinities (PA) of **1** and **2** and those of the reagent conjugate bases[35], methane (544 kJ/mol), water (690 kJ/mol), acetone (812 kJ/mol), and ammonia (854 kJ/mol) (Eq. 9).

$$-\Delta H_r = PA(\mathbf{1},\mathbf{2}) - PA(\text{reagent}) \qquad (9)$$

Since only exothermic protonations are kinetically competitive in ion-molecule reactions in the gas-phase[36], the protonation sites were determined by the proton affinities at each site for **1** and **2**. The proton affinity of **1/2** has not been experimentally determined[37] but an estimate from core electron binding energies[50] placed the gas-phase basicity of **1/2** close to that of pyridine (PA = 924 kJ/mol).[35] The PA of each site in **1** and **2** by MP2 and B3LYP/6-311G(2d,p) calculations are shown. (Figure 17) The calculated proton affinity values showed that the nitrogen atom in **1** (PA = 927 / 933 kJ/mol) and the carbonyl oxygen in **2** (PA = 914 / 931 kJ/mol) were the most basic sites (MP2/B3LYP).

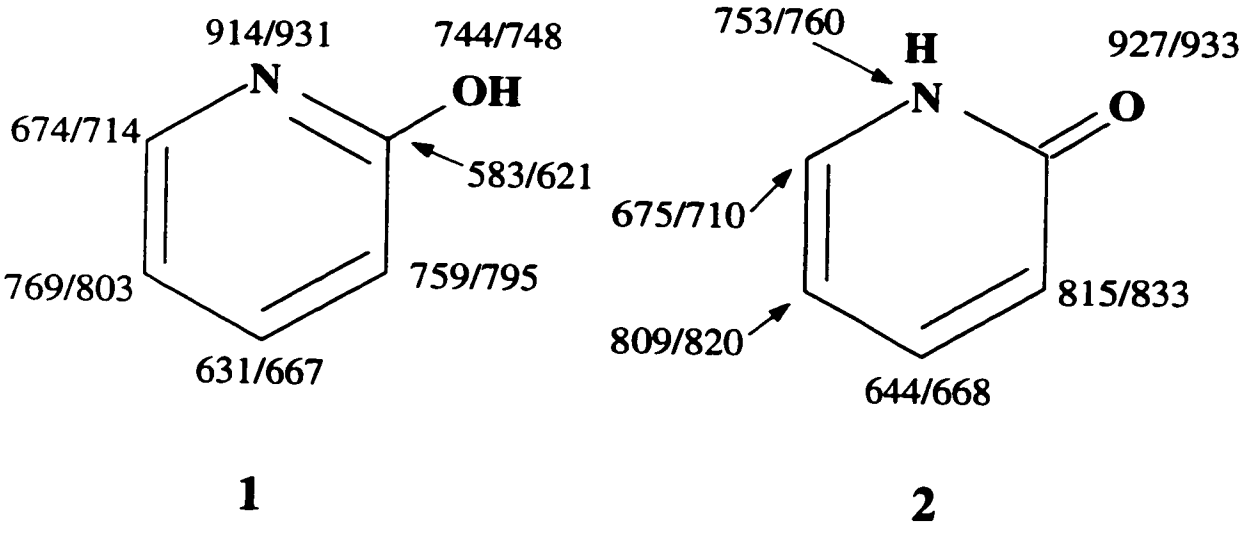

Figure 17. Proton Affinity of **1,2**.

This value falls in between the estimated DFT calculations which bracket the proton affinities of **1** and **2** between 916 and 963 kJ/mol.[51] The other positions in **1** and **2** were substantially less basic (Table 6). Protonation at C4 of **2** to form **2dH$^+$** did not result in a stable ion. Instead, upon attempted geometry optimization **2dH$^+$** rearranged to **2cH$^+$**. It would be expected that **2cH$^+$** would be substantially stabilized over **2dH$^+$** due to the α-oxocarbenium structure of **2cH$^+$**.

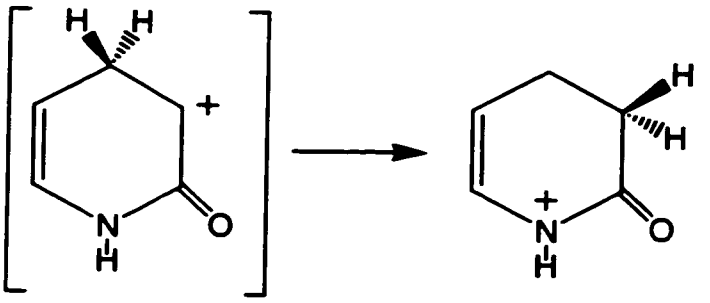

2dH$^+$ **2cH$^+$**

Figure 18. Rearrangement of **2dH$^+$ to 2cH$^+$.**

The calculated proton affinities were used to predict the protonation sites in **1** and **2**. NH_4^+ must attack the most basic site in **1** and **2** exclusively to produce the most stable ion isomer **1aH$^+$**, from both **1** and **2**. This single ion product eliminated the potential problem of determining tautomeric mixtures of **1** and **2**. (Figure 19) Exothermic protonation with $(CH_3)_2C\text{-}OH^+$ was predicted to be completely selective in **1** to form **1aH$^+$**. However, protonation of **2** with $(CH_3)_2C\text{-}OH^+$ at the oxygen site is expected to be predominate to form **1aH$^+$**, but protonations at the C3 and C5 sites were marginally exothermic and could possibly result in formation of **2dH$^+$** and **2fH$^+$** in addition to **1aH$^+$**. Since the formation of **2dH$^+$** and **2fH$^+$** is directly related upon the population of **2** in the ion source, the composition of **1/2** mixture at the ion source temperature was of interest. (Table 6.)

The composition of the **1/2** mixture in the temperature range of the ion source during protonation (200-250°C) was assessed from ΔG_T values obtained by combined MP2 and B3LYP/6-311G(2d,p) and effective QCISD(T)/6-311+G(2d,p) relative energies and HF/6-31G(d,p) zero point corrections, enthalpies, and entropies. Both sets of calculations predicted **1/2** mixture > 2. According to the higher level of theory QCISD(T) calculations which gave ΔH_0(**2**) - ΔH_0(**1**) = 4.7 kJ/mol at 0 K, the fraction of **1** was 73-71% at 473-523 K. These results were in very good general agreement with the few experimental determinations of **1/2** from gas-phase equilibria, which gave ratios ranging from 1.5 to 3.99 (60 - 80%) at various temperatures.[17] Most previous high-level theoretical calculations also predict **1** to be the predominate isomer in the gas phase, although the calculated energy difference depended on the theory used.[52]

Since **2** was a minor component of the **1/2** mixture and protonation at C3 and C5 was less efficient than at oxygen, the contaminant with **2dH**$^+$ and **2fH**$^+$ upon protonation with $(CH_3)_2C\text{-}OH^+$ should be negligible, and the precursor ion would consist mainly of **1aH**$^+$. Based on energetics alone, protonation with H_3O^+ could be less selective, and the strongest gas-phase acid CH_5^+ could nominally attack any site in either **1** or **2** (Table 6).

Table 6. Exothermicity of **1,2** in kJ/mol. MP2/B3LYP

	NH_4^+	$(CH_3)_2COH^+$	H_3O^+	CH_5^+
1				
Nitrogen	61/79	102/119	217/234	363/380
C-2	NA	NA	NA	32/70
C-3	NA	NA	62/98	208/244
C-4	NA	NA	NA	80/116
C-5	NA	NA	72/106	218/252
C-6	NA	NA	-24/17	123/163
Oxygen	NA	NA	47/51	193/197
2				
Nitrogen	NA	NA	56/63	202/209
C-3	NA	3/21	118/136	264/282
C-4	NA	NA	NA	93/117
C-5	NA	-3/8	112/123	258/269
C-6	NA	NA	-22/13	124/159
Oxygen	74/80	115/121	230/236	376/382

NA indicates the reaction is endothermic, and therefore too slow to be occurring in the ion source. Negative numbers are also endothermic reactions, and are included when there are differences between MP2 and B3LYP.

Deuterium labeling in the gas-phase ions was achieved by two methods and could be used to achieve either complete or partial labeling of the basic hydrogens in the system. First, exchanging gas-phase acids, such as ND_4^+/ND_3 and D_3O^+/D_2O were used to prepare **1aDOD$^+$** by exchange of the acidic N-H and O-H protons in **1** and **2** for deuterium, followed by gas-phase addition of a deuterium. This yields a single isotopomer (**1aDOD$^+$**) from both **1** and **2** (Figure 19)

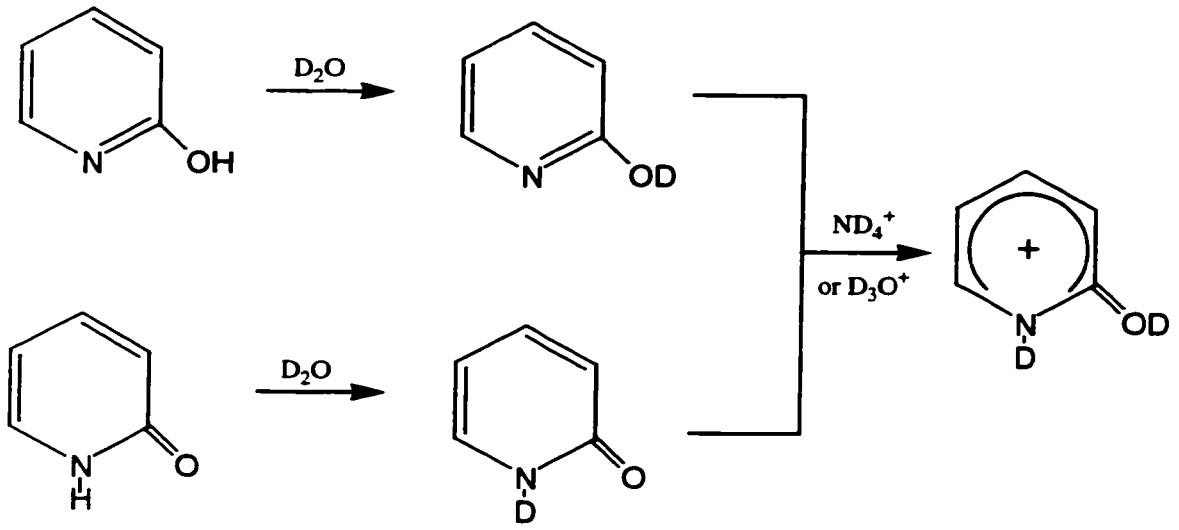

Figure 19. Formation of a single ion product from **1,2**.

Second, partial labeling was accomplished by solution H/D exchange of the acidic O-H and N-H protons followed by gas-phase addition of a H/D with non-exchanging acids, such as $(CD_3)_2COD^+$ or CD_5^+. When preparing the partially labeled ions, the ratio of **1/2** in the ion source will effect the ratio of mixed partially labeled products formed. For example, solution exchange of the basic site in **1** will form **1OD**. When followed by protonation by $(CH_3)_2COH^+$, the expected product of **1aHOD$^+$**. On the other hand, solution exchange of **2** forms **2ND**. When this is followed by gas-phase protonation, the expected product is **1aDOH$^+$**. The ratio of **1aHOD$^+$/1aDOH$^+$** is directly related to the ratio of **1/2** in the ion source as discussed. A different mixture with a reversed ratio of

1aHOD$^+$ and **1aDOH$^+$** was prepared by gas-phase addition of a deuterium to **1,2**. (Figure 20).

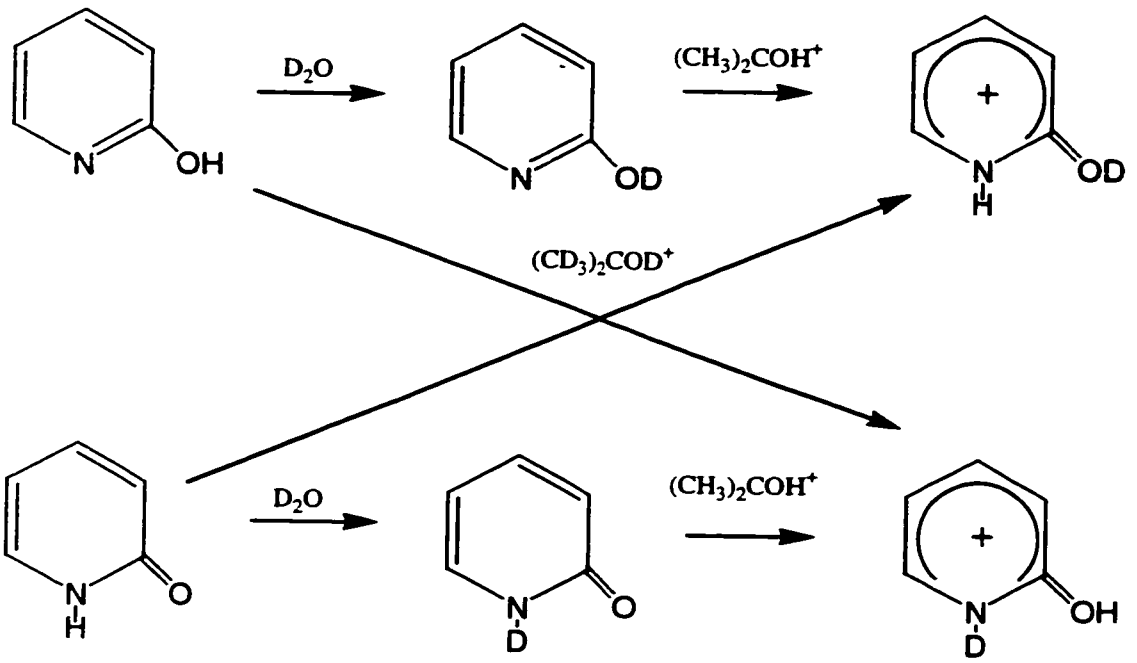

Figure 20. Partial labeling of **1,2**.

The gas-phase chemistry of **1aH$^+$** and its isotopomers **1aDOD$^+$**, **1aDOH$^+$**, and **1aHOD$^+$** were investigated through collisionally activated dissociated spectra (CAD) (Figure 21). The major dissociations were loss of H, H_2O, COH, and ring cleavages forming the $C_4H_{2-4}^+/C_3H_{0-2}N^+$, $C_3H_{1-2}^+/C_2NH_{0-2}^+$, and $HCNH^+$ ions. Hydrogen atom loss involved hydrogens from positions besides the basic sites, as revealed by deuterium labeling. For example, **1aDOD$^+$** (from addition of a deuterium to **1OD** and **2ND** with $(CD_3)_2COD^+$) lost H / D in a 73:27 ratio.

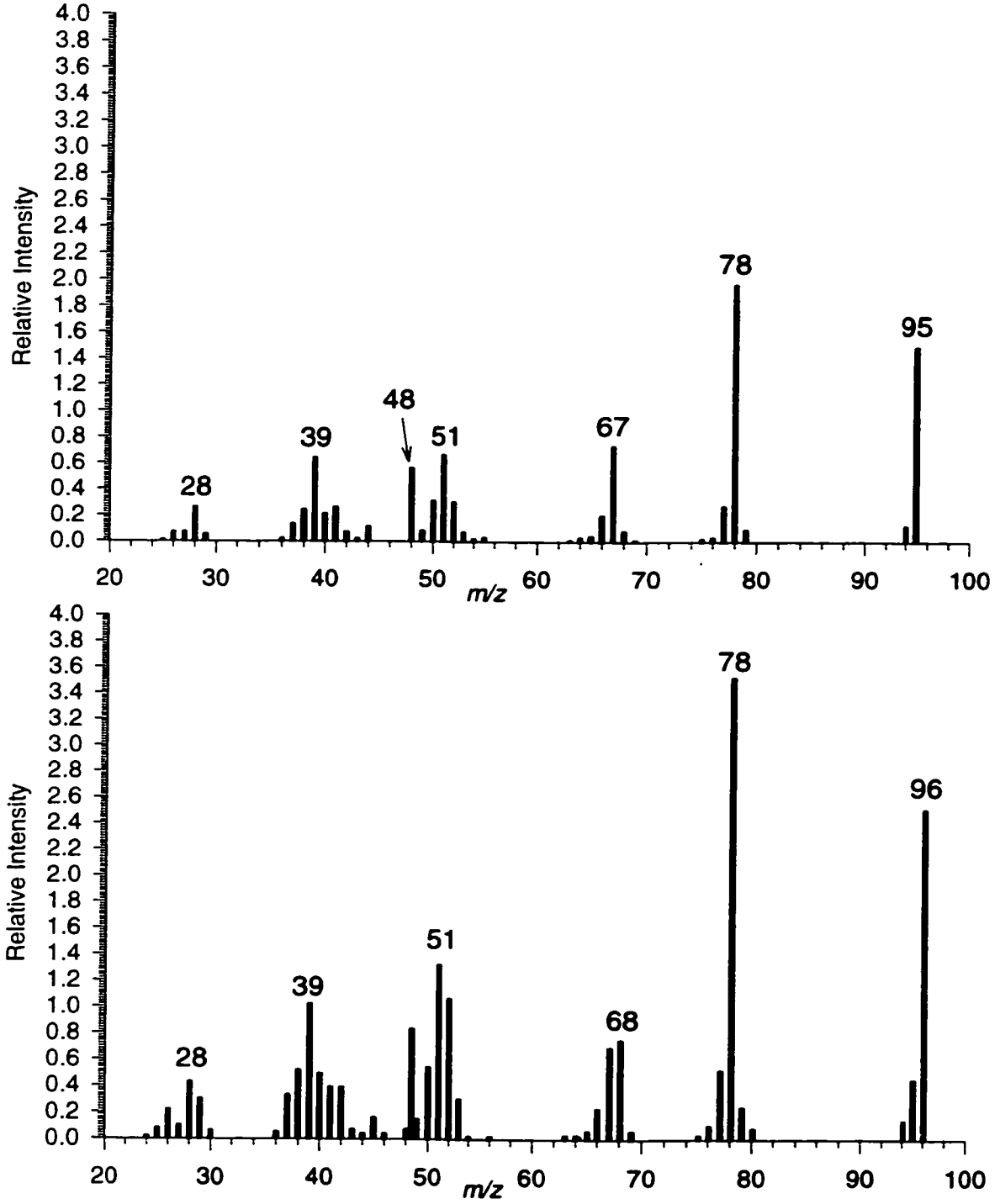

Figure 21. CAD spectra of (top) **1aH**$^+$ and (bottom) **1aDOH**$^+$/**1aHOD**$^+$ from addition of a deuterium by $(CD_3)_2COD^+$. Air is used as a collision gas at 70% T.

This was only slightly higher than the 67/33 ratio (4H/2D in the system) expected from a random loss of H or D from any position. CAD of **1aHOD**$^+$ and **1aDOH**$^+$ showed loss of H / D in 83:17 and 85:15 ratios respectively, as compared to with the 83:17 ratio from a purely statistical loss (5H/1D in the system). This indicates that the loss of H from **1aH**$^+$ involved hydrogen atoms from positions other then the most basic site in the molecule. Some or all of the ring hydrogens must have been lost as well to make the ration for H/D loss nearly statistical. Available thermochemical data allows estimates of the thresholds for the dissociations, **1aH**$^+$ → **1**$^{+\bullet}$ + **H**• and **1aH**$^+$ → **2**$^{+\bullet}$ + **H**• as 425 and 480 kJ/mol respectively. This is substantially higher then the typical energy barriers for proton migration in protonated aromatic ion (100-150 kJ/mol).[44] Therefore extensive hydrogen scrambling in **1aH**$^+$ is expected to precede loss of H in dissociating ions.

In summary, the CAD measurements identified small neutral species that were formed by ion dissociations which could present interferences in the study of radical dissociations following collisional electron transfer.

Radical Formation and Dissociation:

Collisional neutralization – reionization of **1aH**$^+$ formed a fraction of radicals **1aH**• that gave rise to nondissociating (or survivor) ions in the NRMS spectra. This establishes that **1aH**• were stable species on the time scale of the experiment, which was 4.67 μs. The fraction of survivor ions depended on the internal energy of the precursor ions, which were in turn limited by the corresponding protonation exothermicities. **1aH**$^+$ prepared by protonation with NH_4^+, $(CH_3)_2COH^+$ and H_3O^+ yielded survivor intensities between 2.2-3.5% of the sum of all ion intensities in the NR spectrum. The most energetic protonation with CH_5^+ yielded substantially smaller fractions of survivor ions (0.3%). The major dissociations from **1aH**• were losses of H (*m/z* 95), expulsion of COH to form pyrrole (*m/z* 67), and ring cleavage resulting in the formation of small fragments C_2H_2/CN (*m/z* 26) HC=NH (*m/z* 28) and $C_2H_{0-3}/C_2H_{0-3}N$ (*m/z* 36-41). Some of these dissociations were also seen as ionic dissociations in the CAD experiments, although the product ion relative intensities in the CAD and NR spectra were different.

Isotope effects on stability of **1aH•** were observed for **1aDOD•** prepared by solution exchange of the basic sites followed by gas-phase addition of a deuterium by ND_4^+ and $(CD_3)_2COD^+$, **[1aDOD•]** / **[1aH•]** = 1.46 and 3.1 respectively. In contrast, negligible isotope effects were observed for the relative abundances of **1aDOD•** in NR of ions prepared by deuteration with D_3O^+ and CD_5^+. Deuterium labeling in **1aHOD•**, **1aDOH•**, and **1aDOD•** allowed distinction between some reaction mechanisms specific to neutral dissociations. (Figure 23, Table 7). **1aDOD$^+$** was prepared by exchange of the basic deuterium followed by gas-phase addition of an additional deuterium, one incorporated by collisions with the walls of the ion source and one by gas-phase deuteration by ND_4^+ / ND_3. **1aDOD$^+$** showed loss of D / H in a 52:48 ratio. (Figure 23, Table 7). This differed greatly from the ion dissociations which preferred loss of H preferentially. Collisional activation of radicals **1aDOD•** through collisions with helium resulted in an overall increase of dissociations and also an increased specificity for D loss. When 30% of **1aDOD•** was allowed to undergo collisional activation, the loss of D and H occurred in a 69:31 ratio, whereas on collisional activation of 50%, the ratio increased to 87:13. This points to a highly specific loss of H / D from the N-(H,D) and O-(H,D) positions in neutral **1aH•** and the isotopomers. This is vastly differing behavior then that seen from the ions where statistical loss indicated non-specificity from all sites.

Another explanation would presume that the intermediate radicals were energized by collisional activation, but the observed dissociations occurred from the ionic dissociations after collisional reionization. Therefore, the effect on the H / D loss by increasing the number of collisions in the CAD spectra of **1aHOD$^+$** was examined. At 70% ion beam transmittance, Poisson distribution predicts 83% single collisions while at 50% transmittance, the single collision rate drops to 69%. The fractions for the H/D loss from **1aHOD$^+$** did not change beyond the experimental error (±2%). Therefore, CAD ion dissociations were shown to be insensitive to the mode of ion excitation. This is in agreement with the prediction that loss of H from **1aH$^+$** which require an estimated 425 and 480 kJ/mol to form **1$^{+\bullet}$** and **2$^{+\bullet}$** respectively at the thermochemical threshold at 298 K. Such high-energy dissociations are typically insensitive to variations of internal

energy in the dissociating ion. NR of **1aDOD$^+$** prepared by gas-phase addition of a deuterium by $(CD_3)_2COD^+$ on **1OD** and **2ND** showed a 47:53 ratio for loss of H/D which did not differ substantially from that for **1aDOD$^+$** prepared by the weaker gas-phase acid ND_4^+. (See Table 7). The loss of H can be attributed to nonspecific, post-reionization dissociations of **1aDOD$^+$** similar to those discussed above.

The relative abundances of products due to loss of H and D from **1aDOD•** were fitted in the mass balanced equation 10 where D_{NRMS}, D_N, and D_i are the normalized fractions for loss of D from combined NR, neutral, and post-reionization ion dissociations respectively and α_N is the fractional contribution of the neutral dissociations.

$$D_{NRMS} = (1 - \alpha N)D_i + \alpha_N D_N \qquad (10)$$

The value of $D_i = 0.27$ was taken from the CAD spectra of **1aDOD$^+$**. The value of D_N was estimated as > 0.9 based on the NCR spectrum of **1aDOD** which showed predominantly neutral dissociations. Based on these assumptions, equation 10 predicted that upon NR the loss of H,D from **1aDOD** was composed of 28% neutral and 72% post-reionization ion dissociation for **1aDOD$^+$** prepared by deuteration and exchange with ND_4^+/ND_3. Very similar fractions (27% neutral and 73% post-reionization ion dissociations) were obtained for **1aDOD$^+$** prepared by addition of a deuterium with $(CD_3)_2COD^+$ which composed of a mixture of **1OD** and **2ND**.

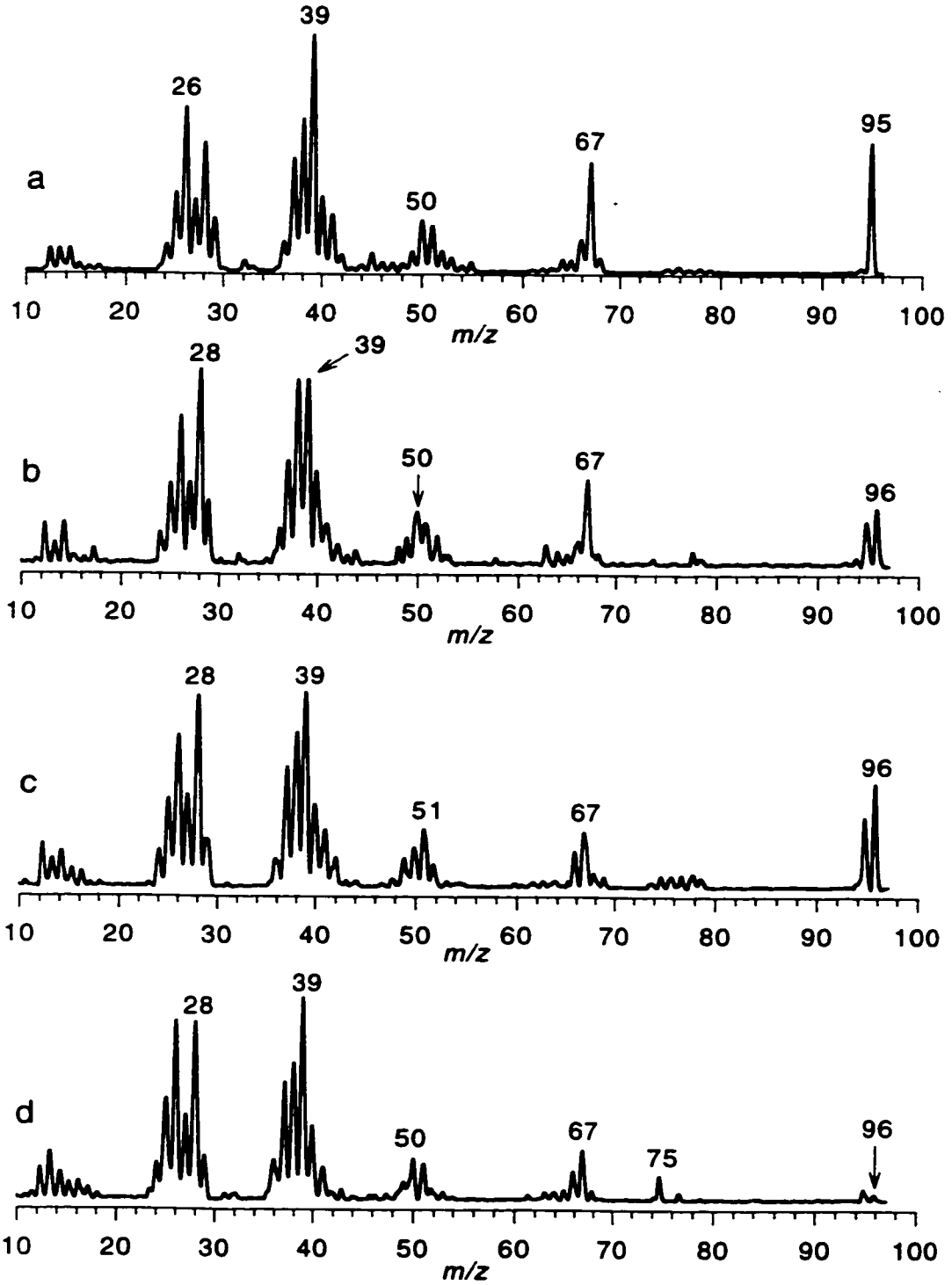

Figure 22. NRMS of a)$\mathbf{1}^{+\bullet}$, $\mathbf{2}^{+\bullet}$ and $\mathbf{1aH}^{+}$ prepared by b) NH_4^+ c) H_3O^+ d) CH_5^+

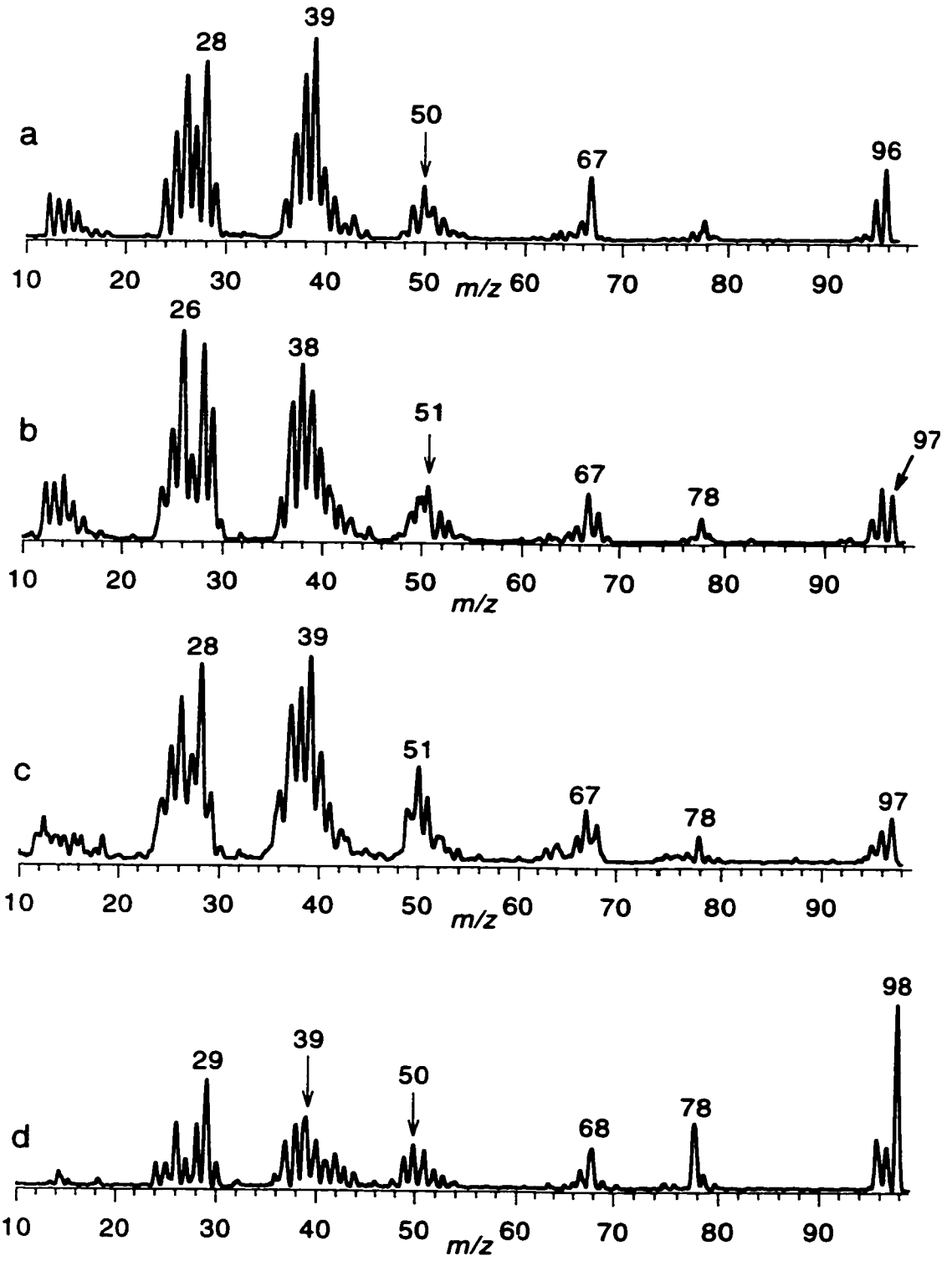

Figure 23. NRMS of a) **1aH**$^+$ b) predominantly **1aDOH**$^+$ c) predominantly **1aHOD**$^+$ d) **1aDOD**$^+$

Table 7. Summary of NRMS experiments for **1,2**

Protonation Reagent	**Ion Structures**	**Loss of D / H** -D % -H	
ND_4^+	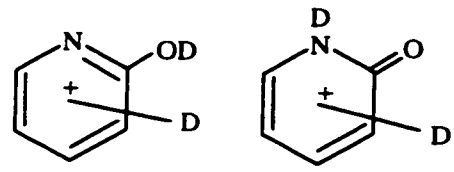	52 $(86)_{NCR}$	48 $(14)_{NCR}$
$(CD_3)_2COD^+$ (from acetone d-6)	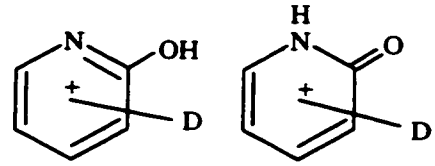	34	66
$(CH_3)_2COH^+$	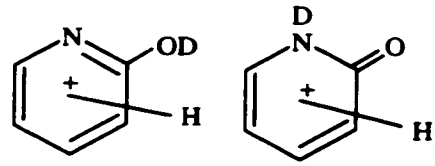	34	66
$(CD_3)_2COD^+$ (from acetone d-6)	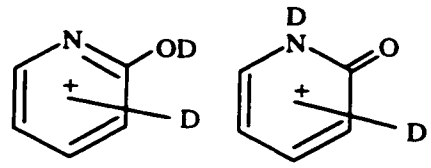	47 $(50)_{NCR}$	53 $(50)_{NCR}$
D_3O^+ (from D_2O)	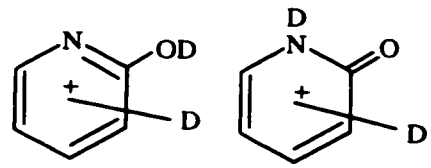	99	1
CD_5^+ (from CD_4)	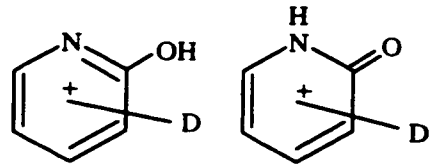	49	51
CH_5^+	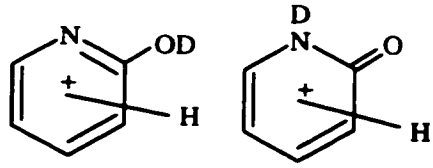	47	53

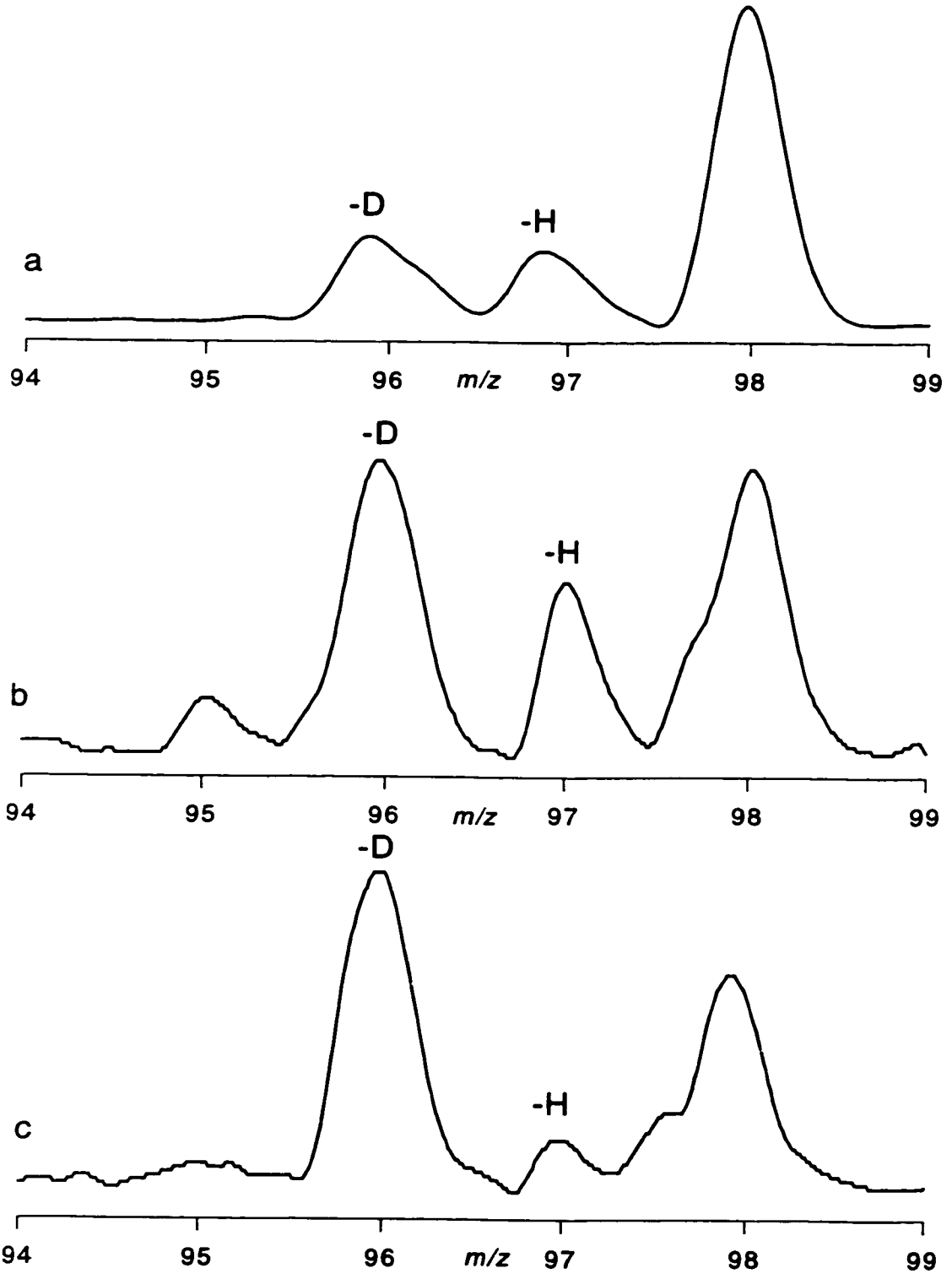

Figure 24. NR and NCR mass spectra of **1aDOD**$^+$ prepared by exchange and addition of a gas-phase deuterium by ND_4^+ a) NR spectrum b) NCR, He 70%T c) NCR He 50%T

NR of the partially labeled ions **1aHOD**$^+$ and **1aDOH**$^+$ showed similar losses of H and D in an approximate 2:1 ratio. However, in this case a clear-cut distinction of the ND and OD bond cleavages could not be made due to both the ion preparations in each case gave mixtures of **1aDOH**$^+$ and **1aHOD**$^+$ and the losses of H and D were affected by kinetic isotope effects, as discussed below.

NR of the **1aDOD**$^+$ from solution exchange of the basic sites followed by gas-phase addition of a deuterium by D_2O/D_3O^+ showed highly specific loss of D (99%). (Table 7). This result showed that isomers other then **1aDOD**$^+$ were not present in the ion beam, since adding a deuterium at sites C3 through C6 would have resulted in increased fractions for loss of H upon NR. For example, if the C3 site had a deuterium added through gas-phase addition, there would now be both an H and D on C3. If there was a loss from this site, barring any isotope effects, the D and the H would be expected to be lost in a 1:1 ratio. Addition of a deuterium by D_3O^+ could occur exothermically at C3,C5, and O in **1** and at N, C3 and C5 in **2**. The fact that loss of hydrogen was not substantially increased by the stronger gas-phase acids indicate that C3 and C5 deuterated ions were not present. If these ions were formed, they underwent exothermic D^+ transfer to the more basic N and O positions in neutral **1** and **2** in the ion source.

The most exothermic addition of a deuterium was with CD_5^+ and showed a yet different result. Deuteration with CD_5^+ showed loss of H and D in ~ 50:50 ratio regardless of the mode of ion preparation. (Table 7). The exothermicity of protonation with CH_5^+ (or CD_5^+) was sufficient to cause extensive isomerization by H^+ or D^+ migrations in nondissociating ions. The energy barriers for such isomerizations can be estimated at < 150 kJ/mol.[44] This is less than the dissociation energy in **1aH**$^+$ and its isomers showing ion isomerization could occur during the flight time between the ion source and neutralization cell (20-40 μs). This region is essentially collision-free and the less stable ion isomers would not be depleted efficiently by ion-molecule reactions.

In addition to loss of a hydrogen atom, NR also indicated ring cleavages occurred that gave rise to small fragments of the C_3H_{0-3}, $C_2H_{0-2}N$, C_2H_{0-2}, and $CH_{0-2}N$ groups. These fragments also appeared in the NR mass spectrum of **1,2**. However, the relative

abundance of survivor $\mathbf{1}^{+\bullet}$ and $\mathbf{2}^{+\bullet}$ (5.2%) from NR of the cation-radical was greater that the relative abundances of $\mathbf{1}^{+\bullet}$ and $\mathbf{2}^{+\bullet}$ from NR of $\mathbf{1aH}^{+}$ (0.6-3.3%). This difference could arise if **1aH•** underwent ring-cleavage dissociations or if **1** was formed from **1aH•** with substantial internal energy that drove the molecular or post-reionization dissociations. Since the products of ring-cleavages dissociations of **1aH•**, $\mathbf{1aH}^{+}$, and $\mathbf{1}^{+\bullet}$ overlapped, the spectra alone would not allow distinction of these processes in the species involved. Therefore, further investigation was needed. The dissociation energetics and kinetics were investigated by a combination of *ab initio*, DFT, and RRKM calculations.

Radical Energetics:

Geometry optimizations yielded local energy minima for radicals **1aH•** - **1gH•** derived from **1** and **2aH•** - **1aH•** (or **2gH•**) derived from **2**. The ordering of relative stabilities for radicals **1aH•** - **1gH•** and **2aH•** - **1aH•** differed from that of the corresponding cations. According to the averaged PMP2 and B3LYP energies, **1cH•** was the most stable structure among the radicals derived from **1**, followed by **1eH•**, **1aH•**, **1fH•**, **1dH•**, and **1bH•**. (Table 8) Radical **2cH•** derived from **2** was the global minimum among the species studied. The optimized structure for radicals from **1,2** are shown in Figure 24 and 25. The most stable ion $\mathbf{1aH}^{+}$ was the sixth most stable radical at 68 and 65 kJ/mol (MP2/B3LYP). This is unlike what was seen for **3** where the most stable ion was also the most stable radicals. Therefore, the possibility of radical rearrangement became of particular importance.

Table 8. Radical Stabilities from UMP2 / B3LYP calculations.

Radical Structure	Symbol	Relative Stability UMP2 / B3LYP	Ranking UMP2	Ranking B3LYP
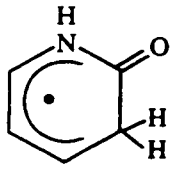	2cH•	0 / 0	1	1
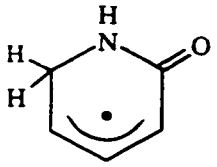	2fH•	19 / 20	2	2
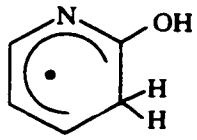	2cH•	35 / 40	3	3
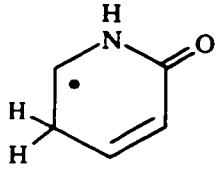	2eH•	61 / 59	4	4
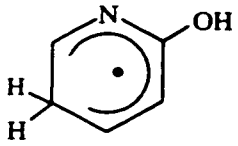	1eH•	63 / 61	5	5
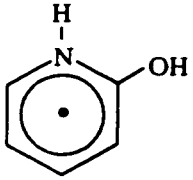	1aH•	68 / 65	6	6
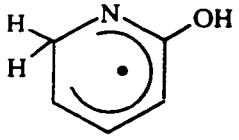	1fH•	75 / 77	7	7
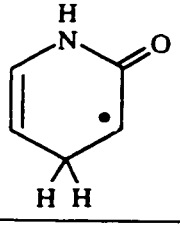	2dH•	86 / 86	8	8

Radical Structure	Symbol	Relative Stability UMP2 / B3LYP	Ranking UMP2	Ranking B3LYP
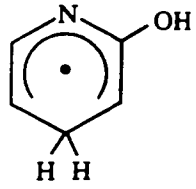	1dH•	86 / 86	9	9
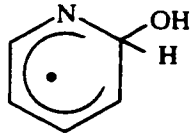	1bH•	104 / 109	10	10
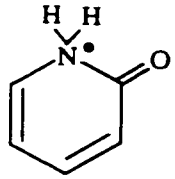	2aH•	145 / 133	11	11

The relative stabilities in the 2-pyridone (**2**) series over the 2-hydroxypyridine (**1**) series can be related to the electronic structure of the isomeric radicals as documented by the spin densities at each site calculated for **2cH•** through **2fH•** by UHF/6-311+G(2d,p). The most stable isomer **2cH•** is an allylic radical substituted by a weak electron-donating acylamino group. The spin densities showed that the unpaired electron was mainly delocalized over the C4 and C6 allylic termini. Spin polarization of the β-atomic orbitals at C4 and C5, which resulted in negative spin densities, was related to spin contamination[54] of the UHF wave function. The slightly less stable **2fH•** is an allylic radical substituted by a weak electron withdrawing amide group, as depicted by delocalization of spin densities at C3 and C5. (Figure 24). The lower energy of **2fH•** suggested that the acylaminoallyl structure was more favorable. Likewise, radicals **2dH•** and **2eH•** contained the α-aminoalkyl and α-carbonylalkyl radical systems, as documented by localization of the spin densities at C6 and C3 respectively. In radicals **2dH•** - **2fH•** the electron withdrawing effect of the carbonyl oxygen resulted in

substantial spin densities at the O atom. Radicals **2dH•** - **2fH•** can be viewed as also containing contributions of structures with oxygen centered radicals. In general, electron-donating groups tend to stabilize allkyl radicals[54] while electron-withdrawing substituents are destabilizing.[55] A combination results in the minor stabilizing effect seen.[56] These effects were only moderate for the acylamino group in **2cH•** and **2eH•** and the amide groups in **2dH•** and **2fH•** and gave rise to only modest differences in the radical relative enthalpies.

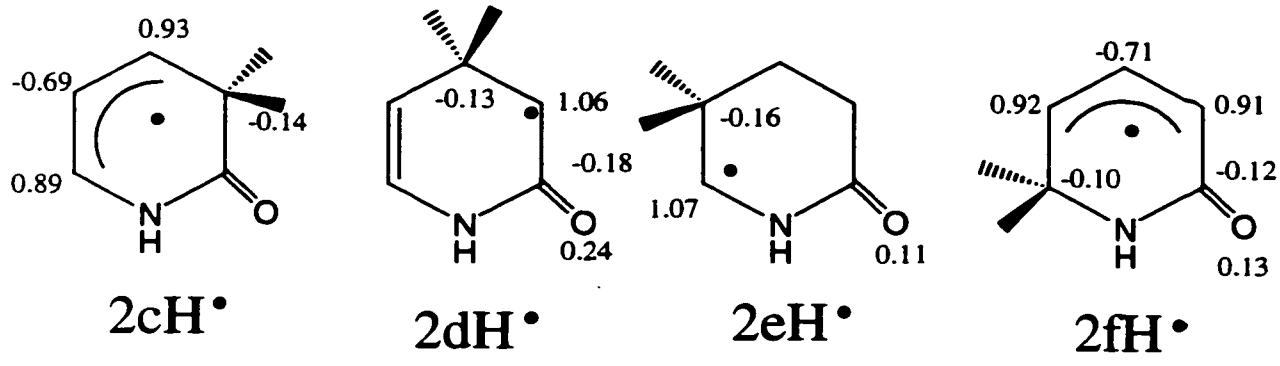

Figure 25. UHF/6-311+G(2d,p) calculated spin densities for **2cH•** - **1fH•**

Radical **2aH•** was calculated to exist as a marginally stable structure whose dissociation to **2** and H required 8 kJ/mol at 298 K. This thermodynamic stability of **2aH•** was somewhat surprising because of the well-known metastability or instability of aliphatic and alicyclic hypervalent ammonium radicals.[57] However, the calculated charge and spin densities in **2aH•** indicated that the radical exists as a zwitterionic form[58] with a positively charged ammonium group (+0.20) and a dienone anion-radical system with negative charges at the oxygen atom and C6. (Figure 26).

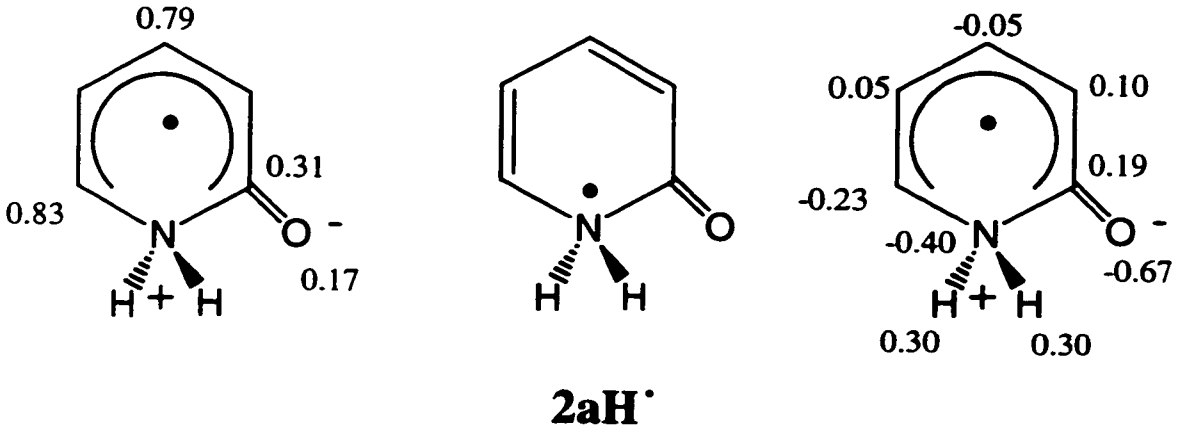

2aH•

Figure 26. UHF/6-311+G(2d,p) calculated total atomic charge (left) and spin densities (right) in **2aH•**.

A similar electronic structure was previously found for the 2-pyrimidylammonium and 4-pyrimidylammonium radicals, which both were local energy minima but were metastable with respect to cleavages of the N-H bonds.[58] The thermodynamic stability of **2aH•** can be attributed to the efficient stabilization of the negative charge by the electron-withdrawing dienone system[59] which removed the destabilizing electron density from the ammonium hydrogen atoms.[60] The low stability of **2bH•** (which breaks the N1-C2 bond upon optimization) can be attributed to the facile opening of the dihydropyridine ring.

Franck-Condon energies (E_{FC}) were also calculated for vertical electron capture in ions **1aH$^+$** - **1gH$^+$** and **2aH$^+$** - **1aH$^+$** (**2gH$^+$**). The E_{FC} values which gauge the mismatch between equilibrium geometry of the ion and that of the radical ranged from 1 kJ/mol (**1fH•**) to 51 kJ/mol (**2eH•**). In general, the Franck-Condon energies resulted from a combination of small differences in several bond lengths and angles in the pyridine ring of the cations and radicals. The Franck-Condon energy accompanying vertical ionization of **1aH•** was also moderate (40 kJ/mol) and by far insufficient to promote dissociation of reionized **1aH$^+$**. Radicals **1aH•** - **1fH•** and **2aH•** - **2fH•** represented the isomeric products of hydrogen atom adduction to **1** and **2** respectively. The reaction enthalpies, $-\Delta H_{add} = \Delta H_{dis}$ are shown in Table 6. Additions to all positions in **1** were exothermic.

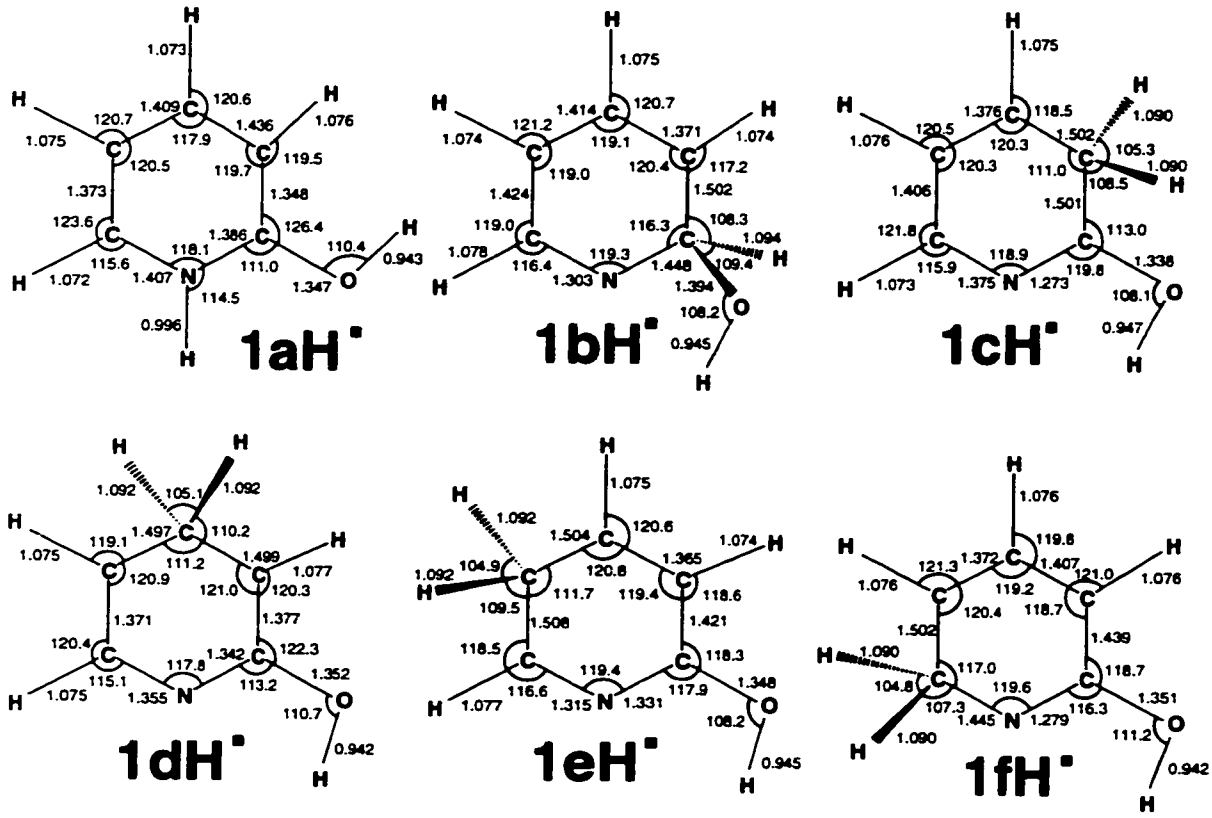

Figure 27. Optimized geometries from radicals derived from **1**.

However, the C-H bonds in **1bH•** – **1fH•** and the N-H bond in **1aH•** were weak, indicating that the radicals could be prone to facile dissociation to **1** unless they were kinetically stabilized by potential energy barriers to loss of H. The C-H bonds in radicals **2cH•** - **2fH•** were on average stronger then those in **1aH•** - **1fH•**, which reflects the greater stability of the former and the higher threshold for the formation of **2** compared with **1**.

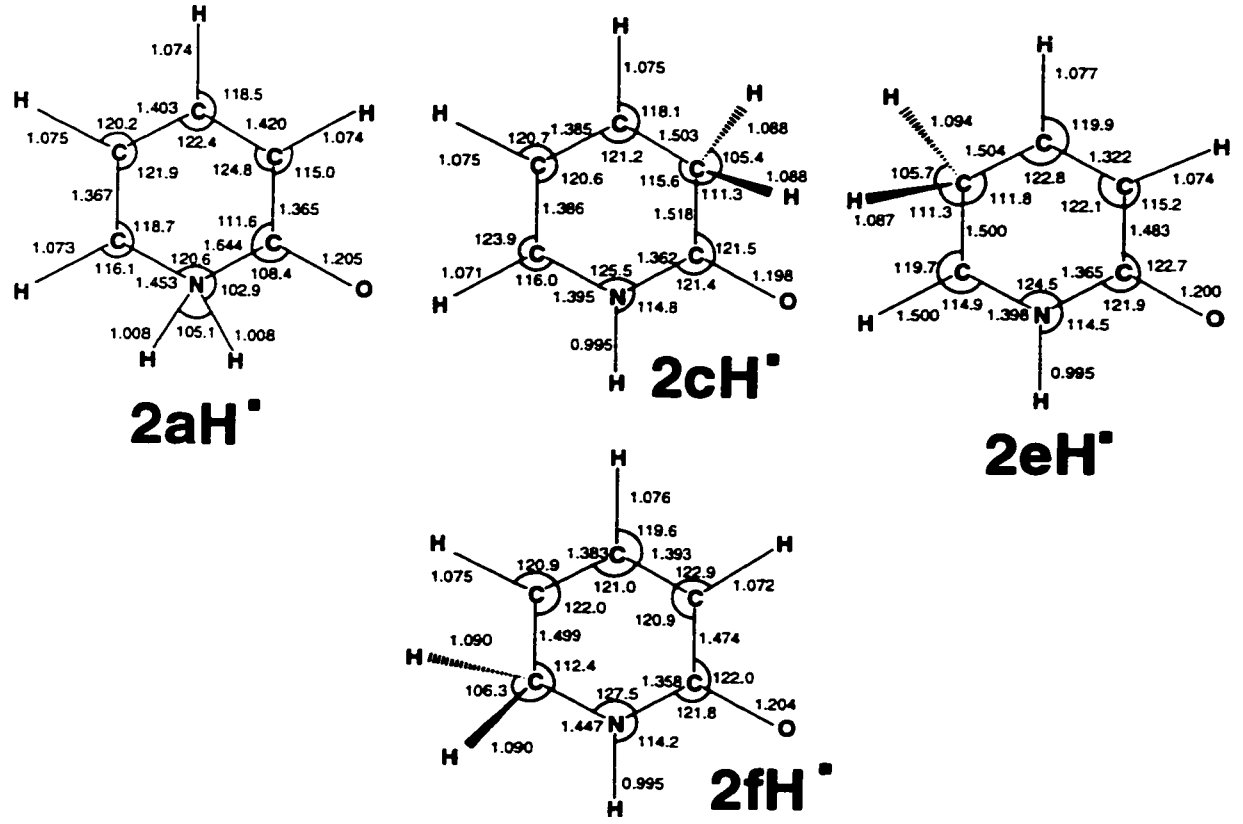

Figure 28. Optimized geometries from radicals derived from 2.

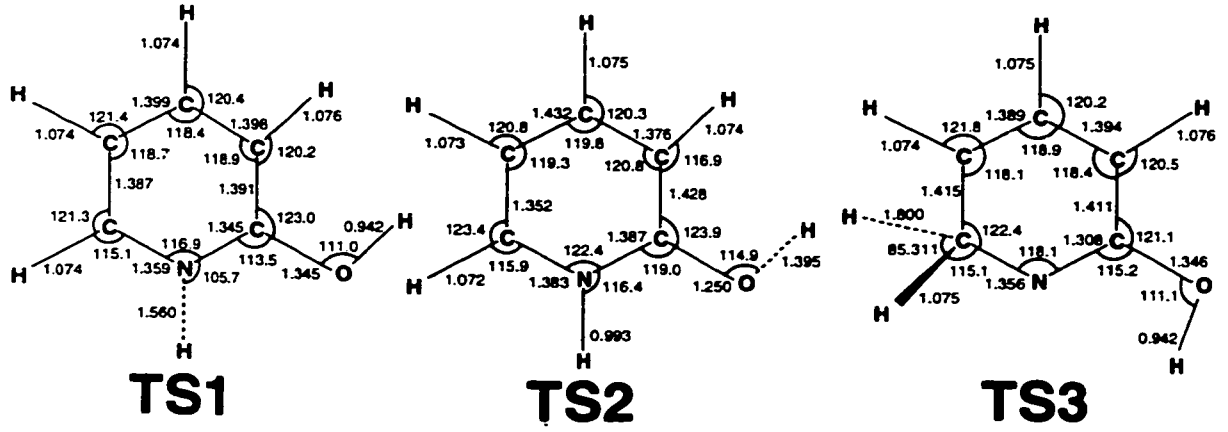

Figure 29. Optimized geometries for the transition states.

Transition State Energetics:

Radical dissociations and rearrangements were also addressed by calculations to obtain the relevant potential energy barriers. The relative energies at 0 K are summarized in a potential energy profile. (See Figure 30)

Dissociations of N-H bond in **1aH•** showed a transition state at d(N-H) = 1.560Å. The energy barrier (E_{N-H}) for **TS1** was calculated by averaged PMP2 and B3LYP and effective QCISD(T) at 120 and 136 kJ/mol above **1aH•** respectively. The value of E_{N-H} depended on both the basis set and the level of correlation energy treatment.(See Figure 30). Increasing the basis set in the PMP2 and B3LYP calculations resulted in a small increase of E_{N-H} by 3.7 kJ/mol for PMP2 energies calculated with the 6-31G(d,p) and the 6-311+G(2d,p) basis sets. The QCISD(T) energy showed another increase by 12.5 kJ/mol compared with the PMP2 energy. Interestingly, the B3LYP and PMP2 values for E_{N-H} were practically identical for the larger basis sets used. The calculations also pointed to substantial activation energy for the addition of a hydrogen atom to a nitrogen atom in **1**, E_{N-H} = 48 and 61 kJ/mol by averaged PMP2 and B3LYP and QCISD(T) respectively. The dissociation energy of the N-H bond in **1aH•** at 298 K BDE(N-H) was calculated as 74 and 78 kJ/mol by the two methods described.

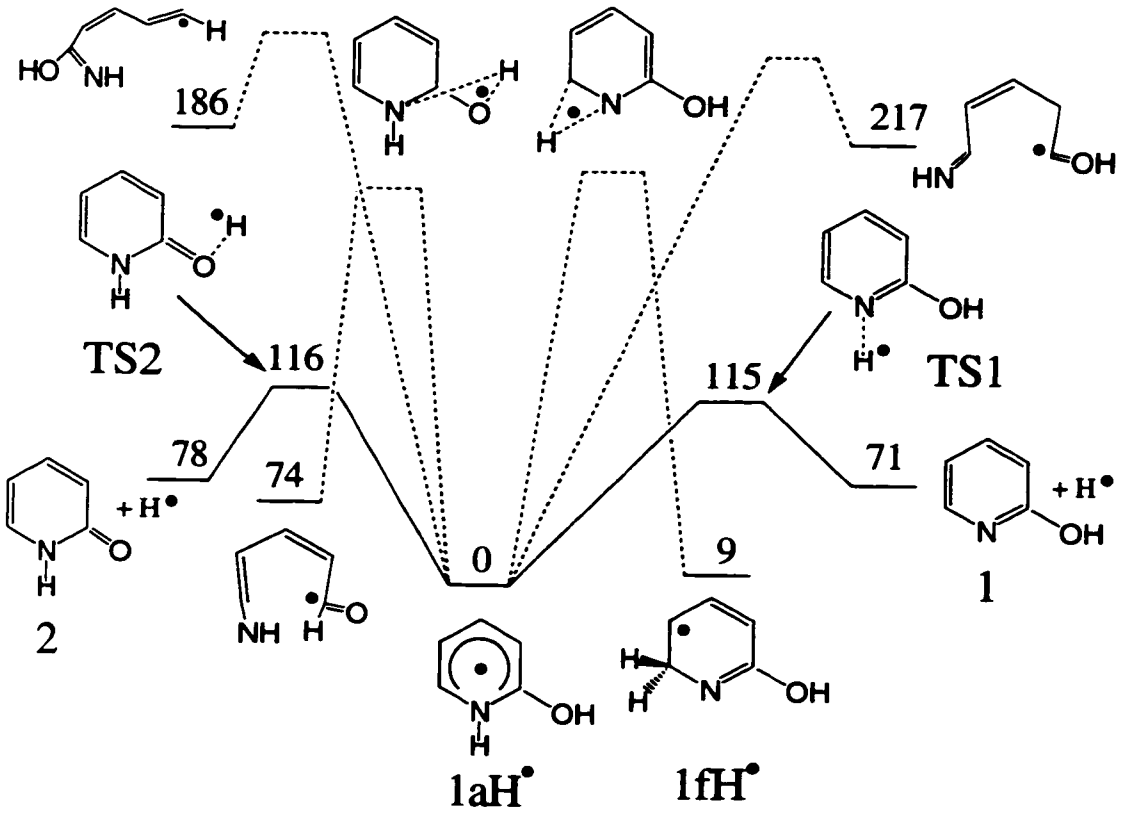

Figure 30. Potential energy profile for dissociations and isomerizations of **1aH•**

Dissociation of the O-H bond in **1aH•** reached an early transition state at d(O-H) = 1.395 (**TS2**). The **TS2** energy ($E_{O\text{-}H}$) was calculated at 116 and 125 kJ/mol above **1aH•** by the averaged PMP2 and B3LYP and QCISD(T) respectively. The differing values of $E_{O\text{-}H}$ depending on theory resulted from a combination of several factors. First, the B3LYP activation energies were systematically 14-16 kJ/mol lower than those from the PMP2 calculations. Increasing the basis set resulted in a slight (~ 0.5 kJ/mol) lowering of the $E_{O\text{-}H}$, while improving the correlation energy treatment by QCISD(T) increased the

$E_{O\text{-}H}$ by 4 kJ/mol. The calculated $E_{O\text{-}H}$ provided the activation for the addition of a hydrogen atom to the carbonyl oxygen in **2**, E_{O+H} = 38 and 46 kJ/mol respectively for the two sets of calculations. It is interesting to note that the transition states for both the O-H bond cleavage and formation had lower energies that the corresponding ones for the N-H bond cleavage and formation. These small energy differences affected the kinetics of the competing dissociations of **1aH•** and additions of H to **1** and **2**, as discussed below.

Table 9. Transition State and Dissociation Energies

	TS1	TS2	1 + H[b]	2 + H[b]
PMP2 6-31G(d,p)	119	126	50	63
PMP2 6-311G(2d,p)	119	124	53	66
B3LYP 6-311G(2d,p)	120	107	94	96
PMP2 6-311+G(2d,p)	123	121	58	70
B3LYP 6-311+G(2d,p)	124	107	98	99
QCISD(T) 6-31G(d,p)	132	130	70	77
QCISD(T) 6-311+G(2d,p)[a]	136	125	78	83

In kJ/mol relative to **1aH•** including zero-point corrections. a) Effective values from eq. 4. b) at 298 K including thermal vibrational, rotational, and translational corrections.

A transition state was also sought for hydrogen migrations that would isomerize **1aH•** → **1fH•** and **1aH•** → **2cH•**. The potential energy surface for the migration of the N-H hydrogen to C6 was mapped systematically by UHF/6-31G(d,p) calculations for fixed N···H distances between 1.45 and 2.1 Å. An important feature of the potential energy surface was a valley along the N-H dissociation coordinate reaching a saddle point at *d*(N-H) = 1.560 Å and another valley along the C6-H dissociation coordinate. The latter had a saddle point at *d*(C6-H) = 1.80 Å (**TS3**) corresponding to a late transition state for C6-H bond cleavage which was 106 kJ/mol above **1fH•**. The valleys were separated by a ridge whose height decreased continuously with increasing N···H and C6···H distances. Even at *d*(N-H) = 2.1 Å the crest of the ridge showed a negative gradient along the N···H coordinate. This indicates that attempts by **1aH•** to climb the ridge en route to rearrangement to **1fH•** would instead accelerate the motion along the N···H dissociation coordinate and lead to dissociation. Single-point calculations of the crest energy at d(N-H) = 1.560 Å yielded ΔE = 74 kJ/mol which was the height of the ridge above **TS1**. A frequency analysis at this point showed two imaginary frequencies. The calculations indicated that a 1,2-hydrogen rearrangement from N to C6 was energetically impossible in **1aH•** up to 74 kJ/mol above the transition state for dissociation. In addition, even if the first-order saddle points had existed at some larger N···H distance, the rearrangement would have been disfavored due to the repulsive portion of the potential energy surface past **TS1** would impart translational energy to the leaving hydrogen atom to move along the N···H coordinate.

A transition state for the 1,3-migration of the O-H hydrogen atom to C3 in **1aH•** was also investigated by UHF/6-31G(d,p) calculations. Upon moving the hydrogen atom toward C3, the potential energy surface showed a negative energy gradient along the O-H coordinate for all O···H distances investigated 1.35 – 2.1 Å. The gradient decreased with the increasing O···H bond dissociation. No first-order saddle points were found for the hydrogen migration; in contrast, the potential energy surface along the attempted

rearrangement pathways was repulsive in the O···H coordinate and if accessed would result in dissociation rather than rearrangement. It can be concluded that a **1aH•** → **2cH•** rearrangement was kinetically disfavored against dissociation to **2** and a hydrogen atom.

Dissociation Kinetics:

The calculated activation energies allowed the unimolecular rate constants (k_{uni}) to be estimated for N-(H,D) and O-(H,D) bond dissociations in **1aH•** and its isotopomers and to assess the pertinent isotope effects. Since the activation energies obtained at the various levels of theory differed by several kJ/mol, the RRKM calculated rate constants differed by 2-3 orders of magnitude for the differing sets of energies. However, relative rate constants for the competitive losses of N-H and O-H hydrogen atoms showed consistent trends as did the calculated isotope effects.

The calculated log(k_{uni}) for the N-H and O-H hydrogen atoms dissociations in **1aH•** are shown. Both sets of calculations predicted moderate kinetic shifts (ΔE_{kin}) for the dissociations. The kinetic shifts were due to the fact that achieving dissociation on the time scale of the measurements (4.67 μs) required appropriate k_{uni}, e.g. log(k_{uni}) = 5.17 for 50% dissociation. On the basis set of the combined PMP2/B3LYP and QCISD(T) calculations, 50% dissociation of **1aH•** by cleavage of the O-H bond was expected to show ΔE_{kin} = 24 and 30 kJ/mol respectively. The extra energy provided additional kinetic stabilization for **1aH•** with internal energies between $E_{a,O-H}$ (116-125kJ/mol) and $E_{a,O-H}$ + ΔE_{kin} (140 – 156 kJ/mol).

To evaluate the RRKM rate constants, kinetic isotope effects were calculated for the various combinations of H and D losses from **1aDOD•**, **1aDOH•**, and **1aHOD•** and compared with experiment. The calculated k_{uni} for the N-H and O-H bond cleavages in **1aH•** denoted as k_{N-H} and k_{O-H} respectively, and N-D and O-D bond cleavages in **1aDOD•** denoted as k_{N-D} and k_{O-D} respectively were population averaged with a Boltzmann-like internal energy distribution function, *P(E)* (eq.11) and used to calculate the flux of radicals nondissociating on the time scale of the experiment (τ = 4.67 μs). A

single distribution function was considered for **1aH•** and **1aDOD•** to simplify the calculations.

$$P(E) = \frac{4(E-E_0)\, e^{-2(E-E_0)/W}}{W^2} \quad (11)$$

$$[\mathbf{1aH\bullet}] = \{[\mathbf{1aH\bullet}] + [\mathbf{1aH\bullet} - H]\} \int P(E) e^{-(k_{N\text{-}H}+k_{O\text{-}H})\tau}\, dE \quad (12)$$

$$[\mathbf{1aDOD\bullet}] = \{[\mathbf{1aDOD\bullet}] + [\mathbf{1aDOD\bullet} - D]\} \int P(E) e^{-(k_{N\text{-}D}+k_{O\text{-}D})\tau}\, dE \quad (13)$$

Since loss of H from the hydroxyl group in **1aH•** to yield **2** was the lowest energy dissociation, the kinetics were evaluated from the fluxes of **1aH•** and **2** and similarly for the labeled derivatives. The fluxes were presumed to be proportional to the integrated peak intensities in the NR spectra, i.e. **[1aH•]** at *m/z* 96, **[1aDOD•]** at *m/z* 98, **[1,2]** at *m/z* 95, and **[2-ND]** at *m/z* 96. This presumed that **1aH•** and **2** had similar ionization cross sections. Such an assumption was reasonably justified by the fact that ionization cross section in general scale with the number of atoms, and **1aH•** and **2** differed by a single hydrogen atom which contributed a small increment.[61] Another assumption inherent to this treatment of dissociation kinetics was that consecutive dissociations of reionization $\mathbf{1aH}^+$ and $\mathbf{2}^{+\bullet}$ occurred to a similar extent, so the measured relative abundances were not skewed by subsequent ion dissociations. The calculated **[1aH•]** and **[1aDOD•]** relative intensities were least-squares fitted to the experimental relative abundances of the corresponding NR ions. The latter were taken from the NR spectra of precursors generated by low-energy protonation with NH_4^+ or deuteration-exchange with ND_3/ND_4^+, **[1aH•]**/{**[1aH•]** + **[2]**} = 0.498 and **[1aDOD•]**/{**[1aDOD•]** + **[2-ND]**} = 0.623. The fit yielded the width (W) and position (E_0) parameters for the internal energy distribution function. The best fit for k_{uni} based on the QCISD(T) calculated energies was W= 49 kJ/mol and E_0 = 105 kJ/mol, which resulted in **[1aH•]**/{**[1aH•]** + **[2]**} = 0.496 and **[1aDOD•]**/{**[1aDOD•]** + **[2-ND]**} = 0.621. The best fit for k_{uni} based on the PMP2/B3LYP calculated energies was W= 28 kJ/mol and E_0 = 100 kJ/mol. The *P*(E)

functions showed maxima, $E_{max} = E_0 + W/2$, at E_{max} = 129 and 114 kJ/mol and full widths at half-maximum, ΔE_{fwhm} = 59 and 34 kJ/mol respectively.(See Figure 31). The calculated energy distribution maxima were reasonable as followed from an energy analysis. The internal energy of **1aH•** (E_{int}) was composed of the internal energy in the precursor ion (**1aH$^+$**) and the Franck-Condon energy upon neutralization (E_{FC} = 31 kJ/mol). The ion energy consisted of the thermal energy in the precursor molecules (38 kJ/mol at 200°C) and 85% fraction of the protonated exothermicity according to the calculations of Uggerud.[46]

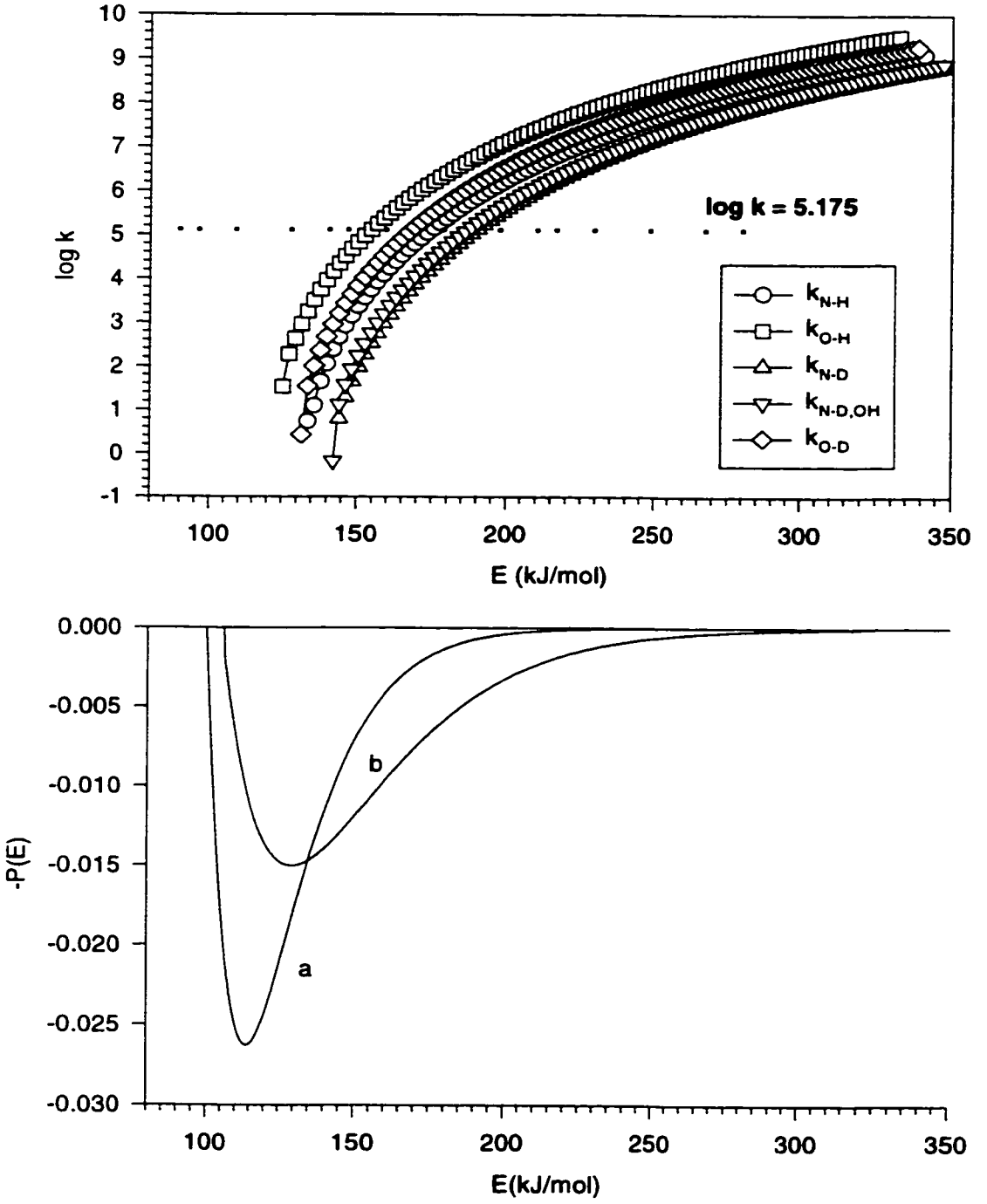

Figure 31. RRKM calculated unimolecular rate constants for the loss of H and D from **1aH•** and **1aDOD•** and the best-fit energy distribution function. The rate constants are based on the effective QCISD(T)/6-311+G(2d,p) activation energies, UHF/6-31G(d,p) moments of inertia and scaled harmonic frequencies.

The latter was estimated by Boltzmann-averaging PA(**1**) – PA(NH_3) = 69 kJ/mol and PA(**2**) – PA(NH_3) = 76 kJ/mol over the populations of **1** (73%) and **2** (27%) at the ion source temperature (200°C). The estimate yielded an average E_{int} = 129 kJ/mol in **1aH•** in close agreement with the *P*(E) maximum obtained by fitting the QCISD(T) energies (129 kJ/mol). A similar estimate was made for the energy distribution in **1aH•** by neutralization of **1aH$^+$** from the more exothermic protonation with $(CH_3)_2C\text{-}OH^+$, $E_{int} \leq$ 164 kJ/mol.

The estimated E_{int} represented an upper energy bound, because the precursor ions underwent several tens of collisions with the NH_3 reagent gas in the ion source. However, recent measurements of intermolecular energy transfer by Dai et al.[62] indicated that the energy transfer per collision becomes very small (<50 cm^{-1}) for hot molecules with internal energies below ca. 200 kJ/mol. It is therefore probable that moderate vibrational excitation in **1aH$^+$** attained by exothermic protonation was not depleted substantially by ion-molecule collisions.

The internal energy distribution functions, in conjunction with the RRKM rate constants further allowed the determination of the branching ratios for the formation of **1** and **2** by competitive dissociations of **1aH•**. The neutral fluxes of **1** and **2** were expressed by eq 14 and 15 respectively. The formations of **1OD** and **2ND** from **1aDOD•** followed similar equations, where τ = 4.72 μs, and the pertinent k_{uni} were $k_{N\text{-}D}$ and $k_{O\text{-}D}$. The $k_{N\text{-}H}/k_{O\text{-}H}$ branching ratios calculated using the QCISD(T) energies did not depend strongly on the internal energy distribution in **1aH•**, e.g. $k_{N\text{-}H}/k_{O\text{-}H}$ = 0.101 and 0.108 for E_{max} = 129 and 164 kJ/mol respectively. The branching ratios were also very similar for dissociations of the labeled radicals **1aDOD•**. The $k_{N\text{-}D}/k_{O\text{-}D}$ = 0.097 and 0.102 for E_{max} = 129 and 164 kJ/mol respectively. The branching ratios based on the combined PMP2/B3LYP energies gave somewhat higher values. The $k_{N\text{-}H}/k_{O\text{-}H}$ = 0.289 and 0.306 for E_{max} = 114 and 149 kJ/mol respectively.

$$[\mathbf{1}] = \int k_{N\text{-}H}[\mathbf{1aH}\bullet]dt = \int dt \int P(E) k_{N\text{-}H}(E) e^{-(k_{N\text{-}H}+k_{O\text{-}H})\tau} dE = \quad (14)$$

$$\int \frac{k_{N\text{-}H}(E)\,P(E)}{k_{N\text{-}H}(E) + k_{O\text{-}H}(E)} [\,1 - e^{-(k_{N\text{-}H}+k_{O\text{-}H})\tau}]\, dE$$

$$[\mathbf{2}] = \int k_{O\text{-}H}[\mathbf{1aH}\bullet]dt = \int dt \int P(E) k_{O\text{-}H}(E) e^{-(k_{N\text{-}H}+k_{O\text{-}H})\tau} dE = \quad (15)$$

$$\int \frac{k_{O\text{-}H}(E)\,P(E)}{k_{N\text{-}H}(E) + k_{O\text{-}H}(E)} [\,1 - e^{-(k_{N\text{-}H}+k_{O\text{-}H})\tau}]\, dE$$

Hence, both sets of calculations predicted preferential formation of **2** upon the lowest energy dissociations of **1aH•**. The higher level of QCISD(T) energies predicted a higher specificity in the formation of **2** from **1aH•**.

Excited States of 1aH•:

The potential-energy surface for the ground electronic state of **1aH•** clearly indicated that loss of H to form **2** and **1** should be the lowest energy dissociations. However, the NR mass spectrum of **1aH•** showed substantial formation of small fragments due to ring-cleavage dissociations similar to that seen in **3**. The latter could not be entirely accounted for by consecutive dissociations of **1**, **2**, or $\mathbf{1,2}^{+\bullet}$ due to the fact that consecutive dissociation showed much less dissociation upon NR. It was also clear that the internal energy distribution of **1aH•** dissociating by loss of H did not allow formation of hot **2** and **1** which would promote consecutive ring-cleavage dissociations in neutral molecules or cation radicals formed by collisional ionization. Dissociations of reionized $\mathbf{1aH}^{+}$ proceeded mostly by elimination of water, whereas products of ring-cleavage dissociations from the radical were less abundant. This pointed to the possibility of ring-cleavage dissociations of **1aH•** from ionic dissociations. However, to be competitive with the H loss, the ring cleavages must occur in very hot radicals of $E_{int} > 220$ kJ/mol which appeared to be incompatible with the internal energy distributions derived from the isotope effects on loss of H and D. A possible mechanism for energy to be deposited in a

fraction of **1aH•** through excited electronic states formed upon collisional electron transfer. Since the latter process is non-resonant the electron can be captured in any of the unoccupied orbitals to form the ground or an excited electronic state of the radical. Only those excited states which are kinetically significant and that have enough energy for ring-cleavage dissociations to occur while also having radiative lifetimes compatible with the time scale of the dissociations are relevant.

The five lowest excited states in **1aH•** were investigated with CIS/6-311G(2d,p) calculations for radicals formed by vertical electron transfer and for those with the relaxed geometry of the ground (X) state. The use of CIS was justified by the substantial energy gap between the doubly occupied 25α orbital and the singly occupied 26α SOMO (ΔE = 3.89 eV) which was greater than the X → A excitation energy (3.54 eV). Single-electron excitations in **1aH•** therefore could involve electron promotion from the 26α SOMO to the appropriate combination of virtual orbitals. Such "outer" excited states were also expected to be formed upon vertical electron capture in **1aH$^+$**. The properties of the first excited state in **1aH•** are shown. (Figure 32).

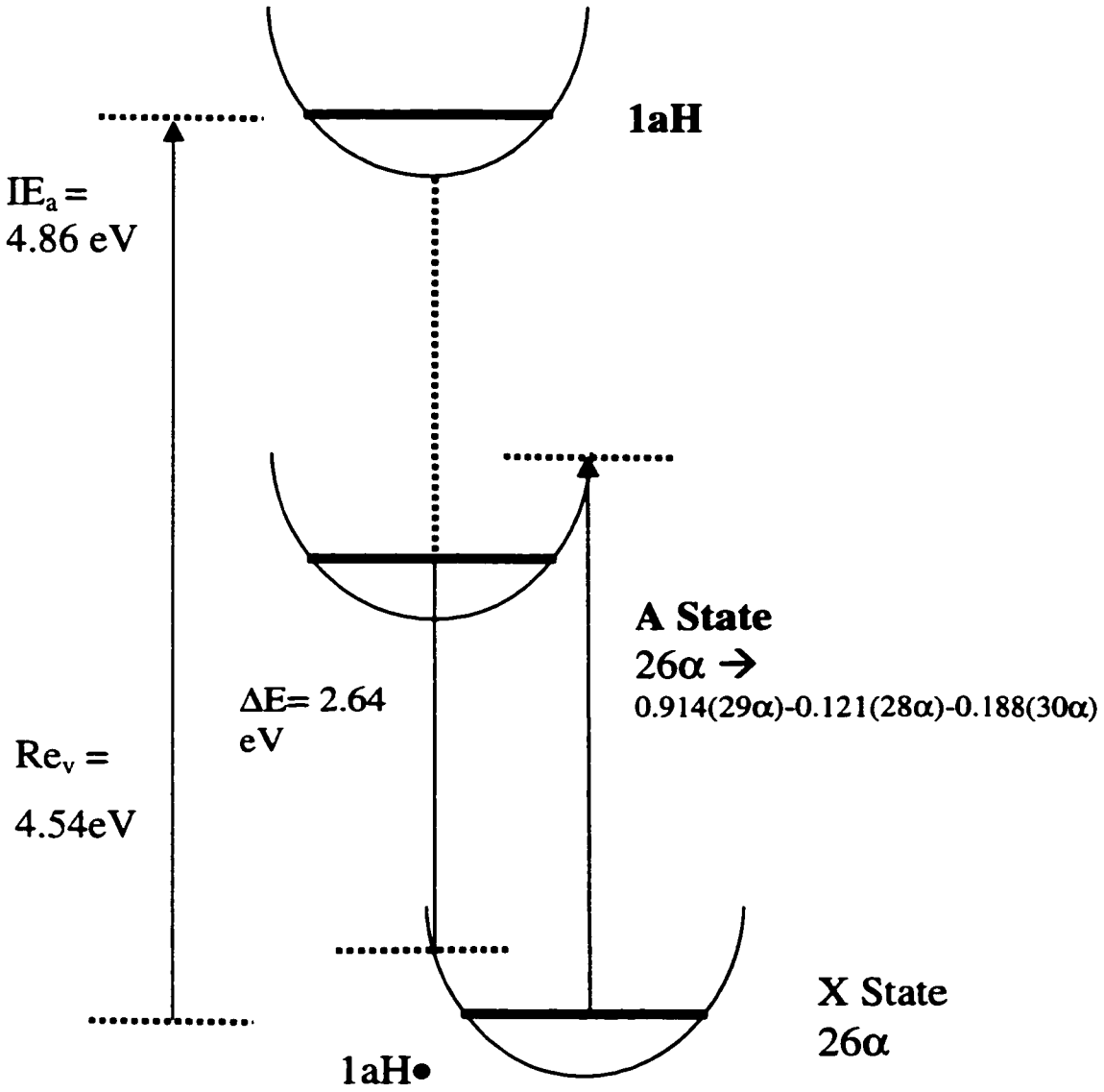

Figure 32. Potential energy diagram for the X and A states in **1aH•**

The potential energy surfaces for the X and A states were shifted, such that the excitation energy in relaxed (X) **1aH•**, ΔE = 3.54 eV was greater that in **1aH•** formed by vertical neutralization of ions in $\mathbf{1aH^+}$, ΔE = 2.64 eV. This shift may facilitate internal conversion of the A state to vibrationally excited X states due to the proximity of the potential energy surfaces.[49] The available energy (255 kJ/mol) was sufficient to promote ring opening in **1aH•**. In addition, the calculated radiative lifetime of the A state, $\tau_{ij} = 1/A_{ij}$ = 0.47 μs, was sufficiently long to allow ring-cleavage dissociations proceeding directly from the A state. Two higher states, B and C, of ΔE = 3.98 and 4.43eV respectively were also outer excited states due to promotion of the 26α electron to combinations of the 27α through 30α virtual orbitals. The calculated radiative lifetimes were 4.8 and 2.3 μs for the B and C states respectively, which were sufficient for unimolecular dissociations to occur. Figure 31 also shows the calculated adiabatic ionization energy of **1aH•** at 0 K, I_{ca} = 4.86 eV from combined PMP2/B3LYP/6-311G(2d,p) calculations.

Although the details of the potential energy surfaces for the A,B,C and higher excited electronic states were unknown, the excitation energies and radiative lifetimes suggested that highly endothermic ring dissociations could occur in vertically neutralized **1aH•**. Internal conversion of the excited states to the X state can be expected to produce the latter with a bimodal distribution of internal energy. The low-energy part of the *P*(E) function is due to both the Franck-Condon effects in the formation of the X state and the precursor ion internal energy, as discussed. The high-energy part of the *P*(E) function is governed by the energy gap between the excited state and the ground state of **1aH•**.

Conclusions:

The experimental and computational data were in agreement that the 2-hydroxy-(1H) pyridinium radical (**1aH•**) was a stable species in the gas phase. Hydrogen atom additions to the N-atom in **1** and to the carbonyl oxygen in **2** had potential energy barriers with addition of a hydrogen atom to **2** was found to be energetically preferred. Radical **1aH•** acquired a bimodal internal energy distribution when formed by collisional electron transfer in the gas phase. The low-energy part of the energy distribution had components of both the internal energy from the precursor ion and the Franck-Condon energy upon vertical electron transfer. The high-energy portion of the energy distribution was due to the formation of long-lived outer excited states that either dissociated adiabatically by ring-cleavage or underwent internal conversion to a vibrationally excited ground electronic state. This system (**1**,**2**) and that of the related **3** radicals pointed out that bimodal energy distributions in molecules and radicals due to populations of excited electronic states upon femtosecond collisional electron transfer may be more common than previously believed.

Chapter V. Uracil

Once the 3-hydroxypyridine (**3**) system and 2-hydroxypyridine/2-(1H) pyridone (**1,2**) model systems were investigated, it was possible to address an even more complex system. **1,2** was chosen as a model system since it has some of the same structural features of the heterocyclic ring in uracil, thymine, and cytosine. It was now possible to understand a system that has six gas-phase tautomers, six potentially basic sites, and possible gas-phase isomerization. In this chapter, uracil ions and radicals were studied predominantly through computational methods such as *ab initio* and DFT to study reaction energetics and RRKM to study reaction kinetics.

Numerous ion and radical structures are discussed in the following text, which are even more complicated since uracil has at least 6 different tautomers and several ions and radicals derived from each of these tautomers. For clarity, a system has been developed. The ring sites (1,2,3,4,5,6) refer to N1, C2, N3, C4, C5, and C6 respectively. Since there are 2 oxygen sites, O7 is the oxygen off C2, and O8 is oxygen off C4. Since there are 6 uracil tautomers, addition of hydrogen through gas-phase protonation yields numerous possibilities. However, naming the 3 sites where the hydrogens reside in addition to the charge information can give the detailed information as to the structure. For example, **113**$^{\bullet}$ depicts a uracil radical with 2 hydrogens on the N1 position, and the third on the N3. To indicate different uracil tautomers only 2 hydrogens are needed.

Every calculation was performed with both ab initio theory and DFT theory. Uracil calculations were run at higher basis sets then either **1,2** or **3**. The basis set used for single point energies was 6-311+G(2d,p). In addition, QCISD calculations were performed as well and also listed.

Abstract:

Isomeric radicals corresponding to hydrogen atom adducts to uracil were investigated by neutralization – reionization mass spectrometry and combined ab initio and density functional theory calculations. Of the six tautomers of uracil investigated, the most stable tautomer was the species with hydrogens bonded to N1 and N3 (**13**). Gas-phase protonation of **13** occurred preferentially at O8. The calculated proton affinities for 13 were 726, 734, 787, 820 and 851 kJ/mol for the N1, N3, C5, O7, and O8 positions respectively. Protonation at C6 was found to form an unstable ion that rearranged the hydrogen to be on C5. The (uracil + H)$^{\bullet}$ radicals were generated by collisional neutralization of (uracil + H)$^{+}$ ion and found to be stable on the 5.1 μs time scale. (Uracil + H)$^{\bullet}$ dissociated by loss of hydrogen and ring cleavages. QCISD extrapolated to the 6-311+G(2d,p) basis set found **135•** to be the most stable radical followed by **136•**, **357•**, **138•** and **367•** at 10, 41, 43, and 62 kJ/mol at 0 K respectively. Transition states for loss of hydrogen and ring cleavages were investigated for **138•** and **137•** with the lowest energy dissociation being ring cleavage of the N3-C4 bond in **137•**. RRKM calculations using the effective QCISD/6-311+G(2d,p) energies for **138•** showed loss of hydrogen from O8 was the most facile fragmentation pathway, whereas cleavage of the N3-C4 bond was the most facile reaction from **137•**.

Results and Discussion

Tautomer Stability:

Six tautomers of uracil were studied using numerous computational methods. Geometries were optimized and frequencies were generated using the Hartree-Fock level of theory at the 6-31G(d,p) basis set. The optimized structures are shown in Figure 33.

Single point energies were obtained from MP2 (frozen core) and B3LYP calculations with both the 6-311G(2d,p) and 6-311+G(2d,p) basis sets. QCISD calculations were also performed and extrapolated (eq. 4) to the 6-311+G(2d,p) basis set. (Figure 34). The tautomer depicted as 'uracil' in numerous biochemistry[20] texts (**13**) was the most stable by 46 kJ/mol (QCISD, 0 K), depending on the level of theory. Tautomers **37**, **78**, and **18** are in close proximity to each other at 46, 53, and 50 kJ/mol respectively (QCISD, 0 K). Tautomer **17** is higher still at 76 kJ/mol, and **38** is the least stable tautomer at 102 kJ/mol. The energy difference between **13** and the rest of the tautomers is sufficiently high that gas-phase isomerization is not likely.

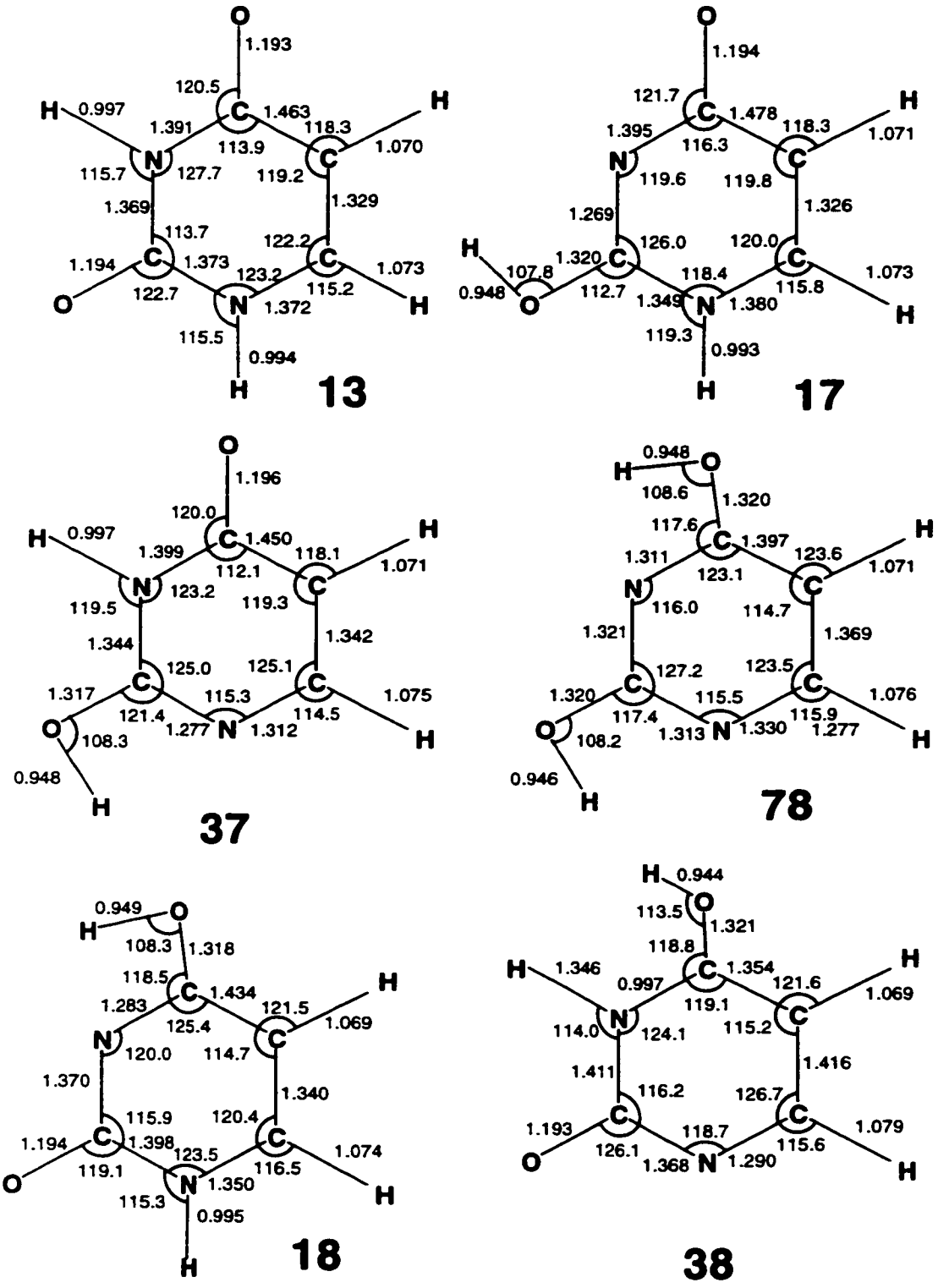

Figure 33. Optimized structure for uracil tautomers

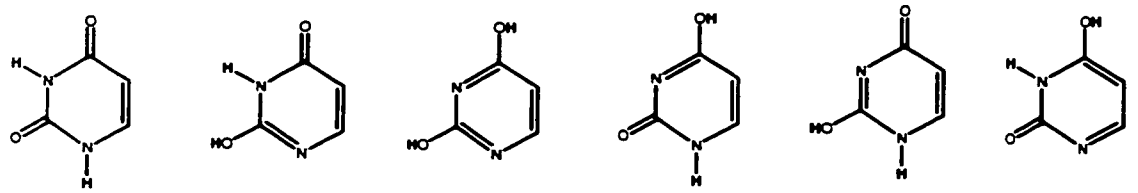

	13	37	78	18	17	38
1)	0/0	43/47	43/52	47/49	78/82	100/99
2)	0/0	43/46	43/52	47/49	75/80	99/98
3)	0	46	52	50	77	103
4)	0	46	53	50	76	102

1) MP2/B3LYP 6-311G(2d,p) 298K
2) MP2/B3LYP 6-311+G(2d,p) 298K
3) QCISD 6-311+G(2d,p) 298K
4) QCISD 6-311+G(2d,p) 0K

Figure 34. Energetics of uracil tautomers

The ratio of species present at the ion source temperature (523 K) determined by ΔG calculations showed that there is expected to be less then 0.1% of any tautomer present besides **13**. This simplifies the tautomer problem significantly. While there are numerous tautomers possible, energetically **13** is the predominant species and contributions to the ion beam from other tautomers are negligible.

Ion Stability:

The ions derived from six tautomers of uracil were studied using several computational methods. Geometries were optimized and frequencies generated at the 6-31G(d,p) basis set. The optimized structures for the most stable ions are shown in Figure 34.

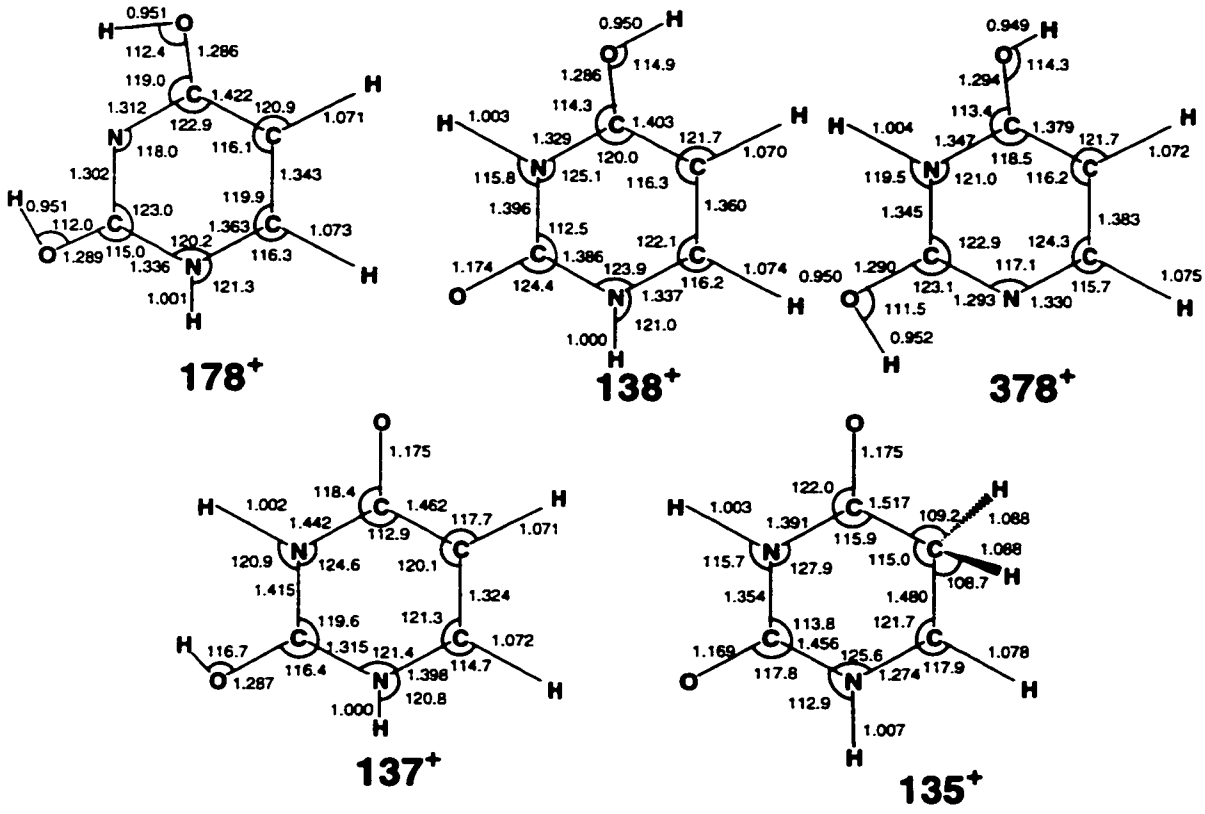

Figure 35. Optimized structure for the five most stable ions

Nearly all ions derived from any uracil tautomer were examined by MP2 and B3LYP at both the 6-311G(2d,p) and 6-311+G(2d,p) basis sets. (Figure 36) The most stable five ions optimized are shown in Figure 33. A few ions (**778**$^+$ and **788**$^+$) were not able to be optimized and were excluded while other (discussed later) rearranged to form more stable ions.

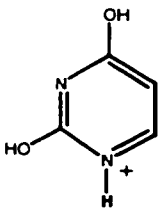

178$^+$

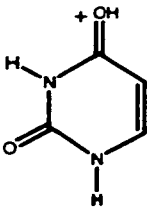

138$^+$

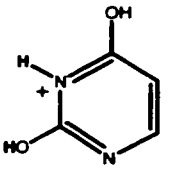

378$^+$

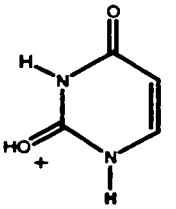

137$^+$

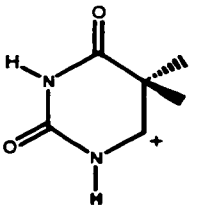

135$^+$

	178$^+$	138$^+$	378$^+$	137$^+$	135$^+$
1)	0/0	9/5	32/31	44/45	83/86
2)	0/0	9/5	32/31	44/45	83/86
3)	0	7	33	39	72
4)	0	7	33	38	71

1) MP2/B3LYP 6-311G(2d,p) 298K
2) MP2/B3LYP 6-311+G(2d,p) 298K
3) QCISD 6-311+G(2d,p) 298K
4) QCISD 6-311+G(2d,p) 0K

Figure 36. Uracil ion energetics.

The most stable ion is **178**$^+$ regardless of theory. This is followed by **138**$^+$, **137**$^+$, **378**$^+$, and **135**$^+$ at 7, 33, 38, and 71 kJ/mol respectively (QCISD, 0 K). An interesting feature of the ion stability series is the most stable ion (**178**$^+$) can not be made from the most stable tautomer (**13**) without a hydrogen rearrangement, which is predicted to be highly endothermic. Therefore, while **178**$^+$ is the most stable ion, **138**$^+$ and **137**$^+$ are more relevant as ions formed in the ion source and consequently will be precursors to the radicals formed in the neutralization cell. Another interesting feature for uracil as compared to the model compounds is that the ion relative energies are much closer to one another, with the difference between the most stable and second most stable ion being only 7 kJ/mol. However, since these ions weren't derived from the same tautomer, this result could be coincident. However, ion **178**$^+$ (0 kJ/mol) and **378**$^+$ (33 kJ/mol) both derived from **78** are significant closer in energy than the model compounds where the energy difference was well over 100 kJ/mol indicating that an H^+ addition to uracil is less site specific than for either model system investigated. This observation was also true for the **13** uracil tautomer. Ion **138**$^+$ (7 kJ/mol) and **137**$^+$ (39 kJ/mol) were also significantly closer in energy than the model compounds.

It is interesting that a few ions (**368**$^+$, **136**$^+$, **368**$^+$, **168**$^+$, **and 678**$^+$) (not shown in Figure 36) could not be optimized, but rather rearranged to form more stable ions (**138**$^+$, **135**$^+$, **358**$^+$, **158**$^+$, and **578**$^+$ respectively). (Figure 37). The rearrangement of **368**$^+$ → **138**$^+$ and the rearrangement of **136**$^+$ → **135**$^+$ are both shown in Figure 37. All of the ions which rearranged had two hydrogens on the C6 position, and rearranged by moving the hydrogen either onto N1 or C5. This result is not too surprising in view that **368**$^+$, **136**$^+$, **368**$^+$, **168**$^+$, **and 678**$^+$ are α-oxocarbenium ions which can be expected to be substantially destabilized.[33] Only one ion was optimized which had two hydrogens on C6 and this ion was found to be highly unstable at 369 / 334 kJ/mol (6-311G(2d,p)).

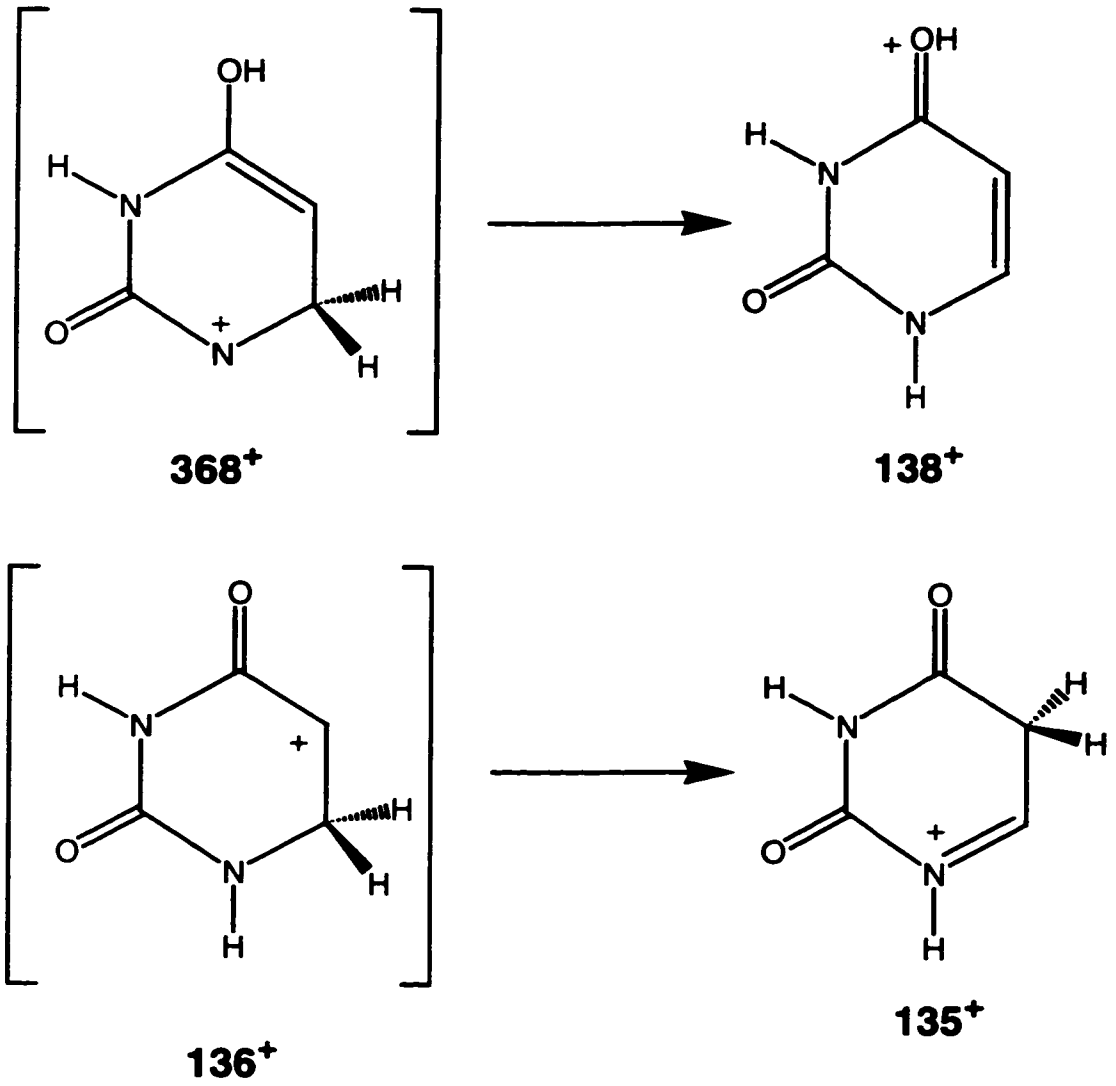

Figure 37. **368**$^{+}$ rearranges to form **138**$^{+}$ and **136**$^{+}$ → **135**$^{+}$

Ion Formation and Dissociations:

The proton affinities for each site in all of the uracil tautomers are listed in Figure 38. Higher-level calculations were only preformed on the most stable tautomer (**13**) as that is the only species expected to be present in the ion source based on ΔG calculations. The two most basic sites for the **13** tautomer is the O8 position with a range of 848-878 kJ/mol depending on the level of theory followed by the O7 position at 813-838 kJ/mol.

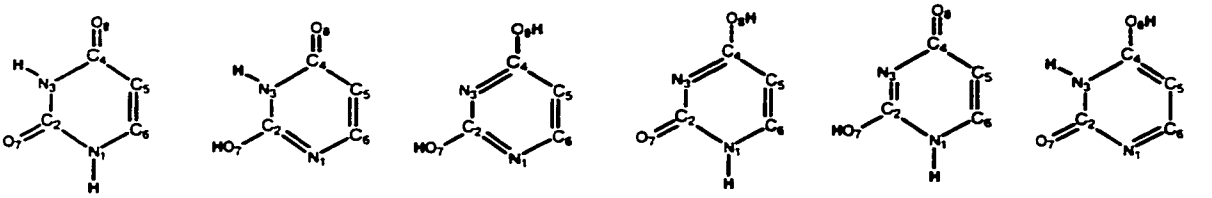

MP2/B3LYP 6/311G(2d,p) 298K

1-3-1 735 / 734	3-7-1 874 / 884	7-8-1 917 / 935	1-8-1 754 / 760	1-7-1 726 / 729	3-8-1 953 / 965
1-3-3 750 / 753	3-7-3 723 / 730	7-8-3 885 / 899	1-8-3 901 / 916	1-7-3 908 / 919	3-8-3 754 / 761
1-3-5 792 / 797	3-7-5 815 / 830	7-8-5 788 / 813	1-8-5 804 / 812	1-7-5 784 / 797	3-8-5 835 / 839
1-3-6 NA made 1-3-5	3-7-6 NA made 3-7-5	7-8-6 NA made 7-8-5	1-8-6 NA made 1-8-5	1-7-6 583 / 631	3-8-6 NA made 3-8-1
1-3-7 831 / 838	3-7-7 583 / 590	7-8-7 NA	1-8-7 923 / 932	1-7-7 726 / 729	3-8-7 925 / 934
1-3-8 865 / 878	3-7-8 868 / 881	7-8-8 NA	1-8-8 700 / 710	1-7-8 952 / 965	3-8-8 904 / 914

MP2/B3LYP 6/311+G(2d,p) 298K

1-3-1 718 / 718	3-7-1 856 / 868	7-8-1 901 / 920	1-8-7 901 / 920	1-7-8 933 / 947	3-8-1 935 / 949
1-3-3 732 / 737	3-7-8 851 / 866	7-8-3 869 / 890	1-8-3 836 / 851	1-7-3 889 / 902	3-8-7 907 / 918
1-3-5 775 / 782					
1-3-6 NA made 1-3-5					
1-3-7 813 / 822					
1-3-8 848 / 857					

QCISD 6/311+G(2d,p) 298K

1-3-1 731	3-7-1 871	7-8-1 916	1-8-7 916	1-7-8 902	3-8-1 94
1-3-3 738	3-7-8 859	7-8-3 884	1-8-3 897	1-7-3 941	3-8-7 91
1-3-5 792					
1-3-6 NA made 1-3-5					
1-3-7 825					
1-3-8 857					

QCISD 6/311+G(2d,p) 0K

1-3-1 726	3-7-1 866	7-8-1 911	1-8-7 911	1-7-8 896	3-8-1 941
1-3-3 734	3-7-8 854	7-8-3 878	1-8-3 892	1-7-3 935	3-8-7 910
1-3-5 787					
1-3-6 NA made 1-3-5					
1-3-7 820					
1-3-8 851					

Figure 38. Proton affinities for different sites of uracil tautomers

Protonation of the most basic site in **13** by NH_4^+ (PA = 854 kJ/mol) would yield a single gas-phase ion $\mathbf{138}^+$. Protonation with $(CH_3)_2COH^+$ (PA = 812 kJ/mol) could yield two gas-phase ions, $\mathbf{138}^+$ mixed with $\mathbf{137}^+$. (Table 10) Stable (uracil + H)$^+$ ions were obtained in each case and used to generate radicals by collisional electron transfer.

Table 10. Exothermicity of **13** and various gas phase acids (kJ/mol)

Uracil 13	NH_4^+	$(CH_3)_2COH^+$
N1	NA	NA
N3	NA	NA
C5	NA	NA
C6	NA	NA
O7	NA	19/26
O8	11/24	53/66

NA means the reaction is endothermic, and therefore too slow to occur in the ion source
MP2/B3LYP 6-311G(2d,p)

To elucidate ion dissociations, CAD were investigated for (uracil + H)$^+$ by protonation with $(CH_3)_2COH^+$. (Figure 39) The major dissociation channels were by loss of H (*m/z* 112), NH_3 (*m/z* 96), H_2O (*m/z* 95), HN=CH or HCO (*m/z* 84) and HNCO (*m/z* 70). (Figure 40) CAD spectra were also obtained for uracil deuterated with $(CH_3)_2COD^+$. This would incorporate **1** deuterium in the uracil added by the gas-phase acid. It is interesting to note that when the only deuterium incorporated in the uracil molecule, the loss of H/D is 87/13. This is actually less deuterium loss than statistically expected. If all hydrogen sites were lost equally, the ratio of H/D would be 4:1. However, we actually lost less deuterium than that, possibly indicating isotope effect in the ions.

In summary, the CAD spectra provides signatures for ion dissociations which can later be distinguished from radical dissociations in the NR spectra. In particular, the ion dissociations were characterized by non-specific loss of hydrogen atom from (uracil + $H)^+$. In addition, small neutral fragments from CAD precursors were identified.

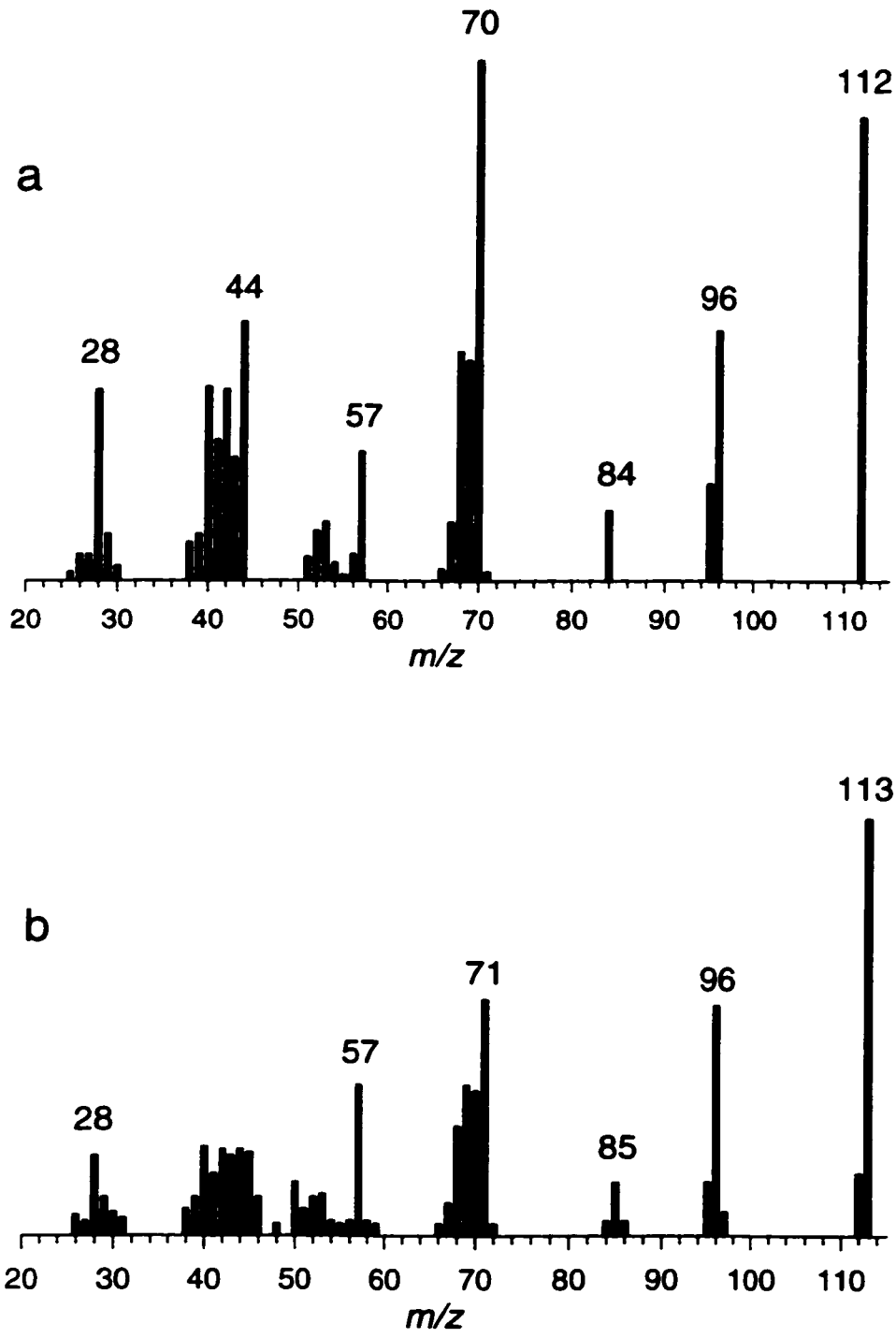

Figure 39. a) Collision-activated dissociation (CAD) mass spectra of (uracil + H)$^+$ at 10keV ion kinetic energy. Air at 50% T was used as a collision gas. b) CAD mass spectra of (uracil + D)$^+$ at 10keV ion kinetic energy. Air at 50% T was used as a collision gas.

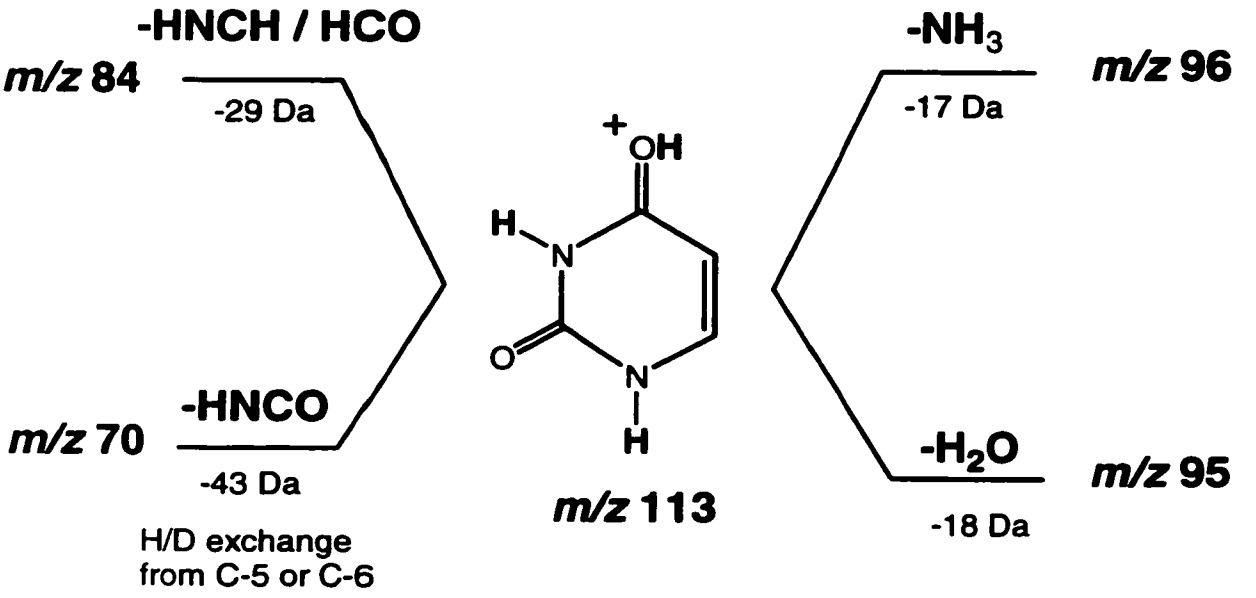

Figure 40. Major ionic dissociations for uracil as seen from CAD spectra

Formation and Dissociations of Radicals (uracil + H)•:

Uracil cation-radical was collisionally neutralized and studied by neutralization – reionization mass spectrometry. The NR spectra (Figure 41a) showed a strong non-dissociating (or survivor ions) signal (*m/z* 112) which indicated that fractions of intermediate uracil molecules were formed that had lifetimes greater than the flight time between neutralization and reionization (~ 5.1 μs). Upon collisional activation of the neutrals with He at 50% beam transmittance, the NCR spectra was obtained. The NCR spectra (Figure 41b) is interesting in how similar it is to the NR spectra. This indicates that the molecules do not dissociate differently under activated conditions, indicating the molecules may be sufficiently stable to sustain excess energy through collisions without fragmentation.

The d-2 labeled uracil (deuterium incorporated on both nitrogen sites) was also examined by neutralization – reionization mass spectrometry. (Figure 42c) This spectrum (shown Figure 39) shows the major dissociation pathway is loss of DNCO (*m/z* 70). From **13** uracil, which is only expected uracil tautomer to be present in the ion source, there are 3 pathways which would all result in loss of DNCO. (Figure 41) There could be a loss of D-N1-C2-O7, as shown in pathway a, or a loss of O7-C2-N3-D (pathway b) or from a loss of D-N3-C2-O8 (pathway c). Which fragmentation pathway occurred can not be determined based on deuterium labeling alone, and if necessary C^{13}, N^{15}, or O^{18} labeling would have to be incorporated to determine the exact mechanism of loss.

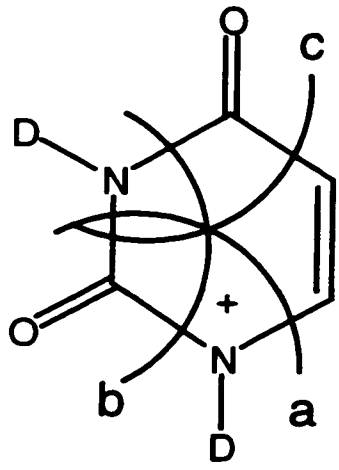

Figure 41. Three different fragmentation pathways for loss of DNCO from d-2 uracil

Collisional neutralization of (uracil + H)$^+$ formed a fraction of radicals (uracil + H)• that gave rise to nondissociating (or survivor) ions. (Figure 42) Deuterium labeling was used to distinguish the reaction mechanism specific to neutral loss. D2-**138**$^+$ prepared by gas-phase addition of deuterium following addition of two deuterium by surface reactions showed loss of D and H in an 84:16 ratio. (Table 11) Partial labeling of **13** showed an interesting result. When one deuterium was incorporated in **13** by gas-phase addition with acetone, the ratio of loss of D to H was 60:40. This is substantially higher then a random loss of D to H which would predict a ratio of 20:80, and considerably higher than the 13:87 loss seen for the ions. This indicates that the radical losses deuterium selectively. However, it is possible to have a mixed product of **138**$^+$ and **137**$^+$ based on ion energetics. It appears the radical loses deuterium predominantly from the site of addition. When the complementary labeling experiment was performed, with 2 deuteriums incorporated were on both nitrogen sites and one hydrogen was added by gas-

phase addition, the predominant loss was hydrogen. The ratio of loss of deuterium to hydrogen was 26 to 74. Again, it is energetically favorable to have a mixed product of **138**$^{+}$ and **137**$^{+}$ by protonation of **13** with acetone.

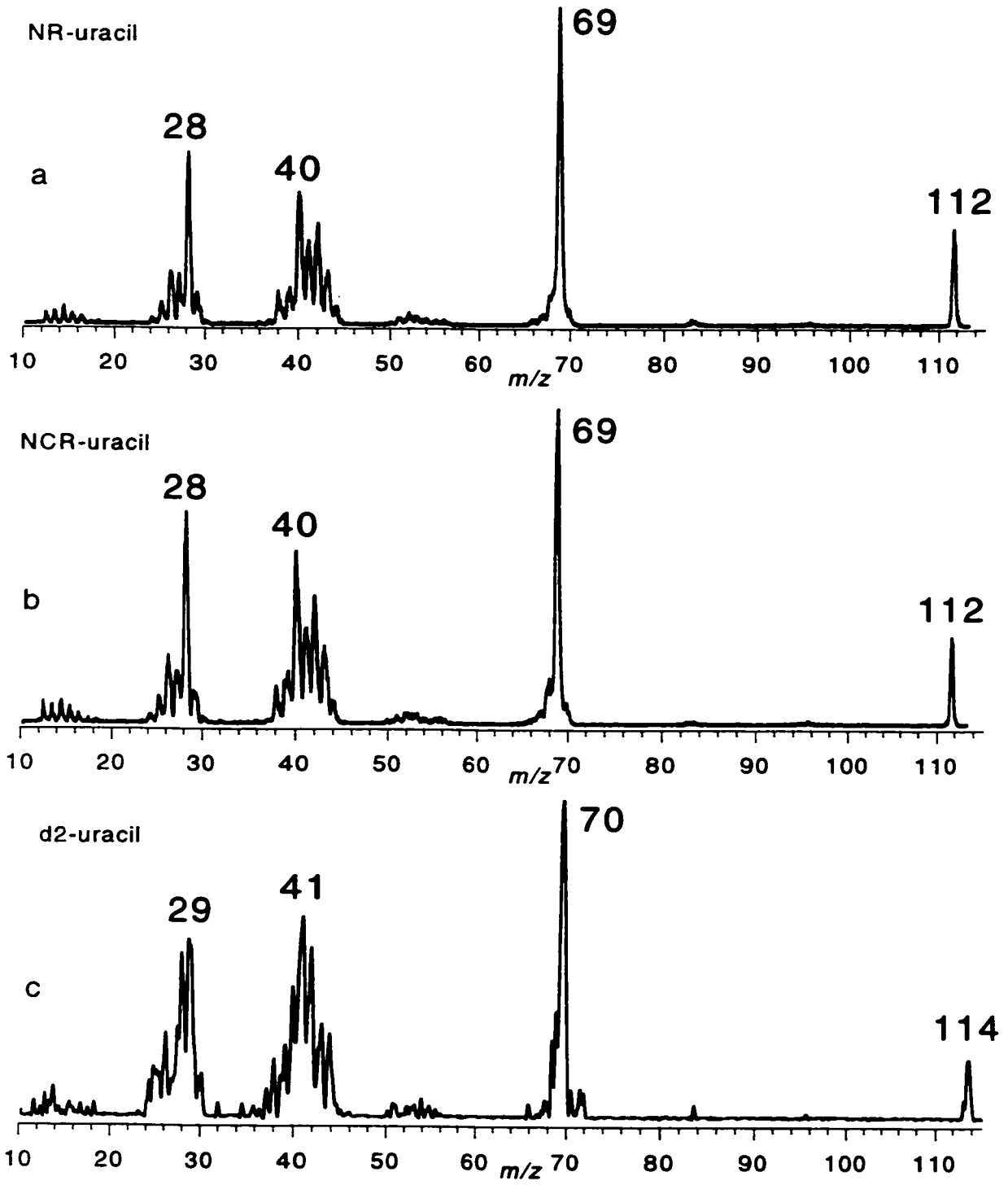

Figure 42. top) NR of uracil middle) NCR (50%He) of uracil bottom) NR of d2-uracil

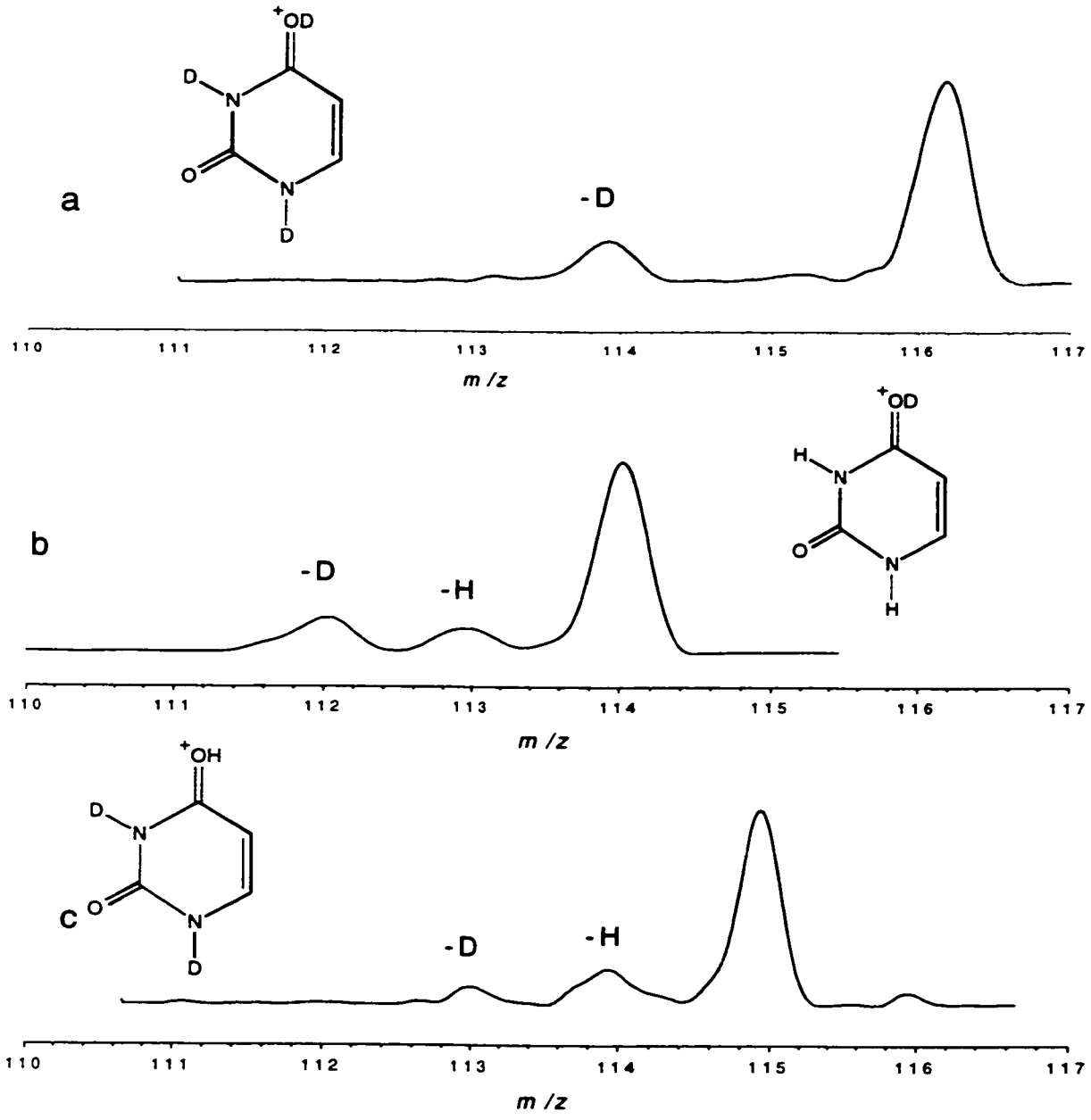

Figure 43. Neutralization (CH_3SSCH_3, 70%T) – reionization (O_2, 70%T) of (a, top) **138•** by protonation of **13** with ND_4^+, (b, middle) **138•** by protonation of **13** with $(CD_3)_2C$-OD^+, (c, bottom) **138•** by protonation of d2-**13** with $(CH_3)_2C$-OH^+.

Table 11. Summary of NRMS data

Protonation Reagent	Ion Structure	Loss of D / H	
		-D %	-H
ND_4^+	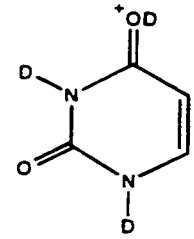	84	16
$(CD_3)_2COD^+$	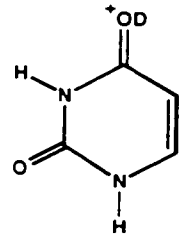	60	40
$(CH_3)_2COH^+$	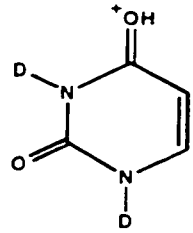	26	74

In addition to loss of hydrogen atoms, NR also induced ring cleavages that gave rise to small fragments similar to those seen in the ions as shown in Figure 43. The predominant ring cleavage was loss of HNCO (43 Da) resulting in C_3H_4NO at *m/z* 70. Unlike the CAD spectra, the ring cleavages are predominant in the NR spectra with *m/z* 70 as the base peak in the spectra. It is interesting that (uracil + H)• dissociates by competing channels, one by loss of H, and the other by ring cleavages. A deeper insight was sought about these competing reaction, and was further investigated using *ab initio*, DFT, and RRKM kinetic calculations.

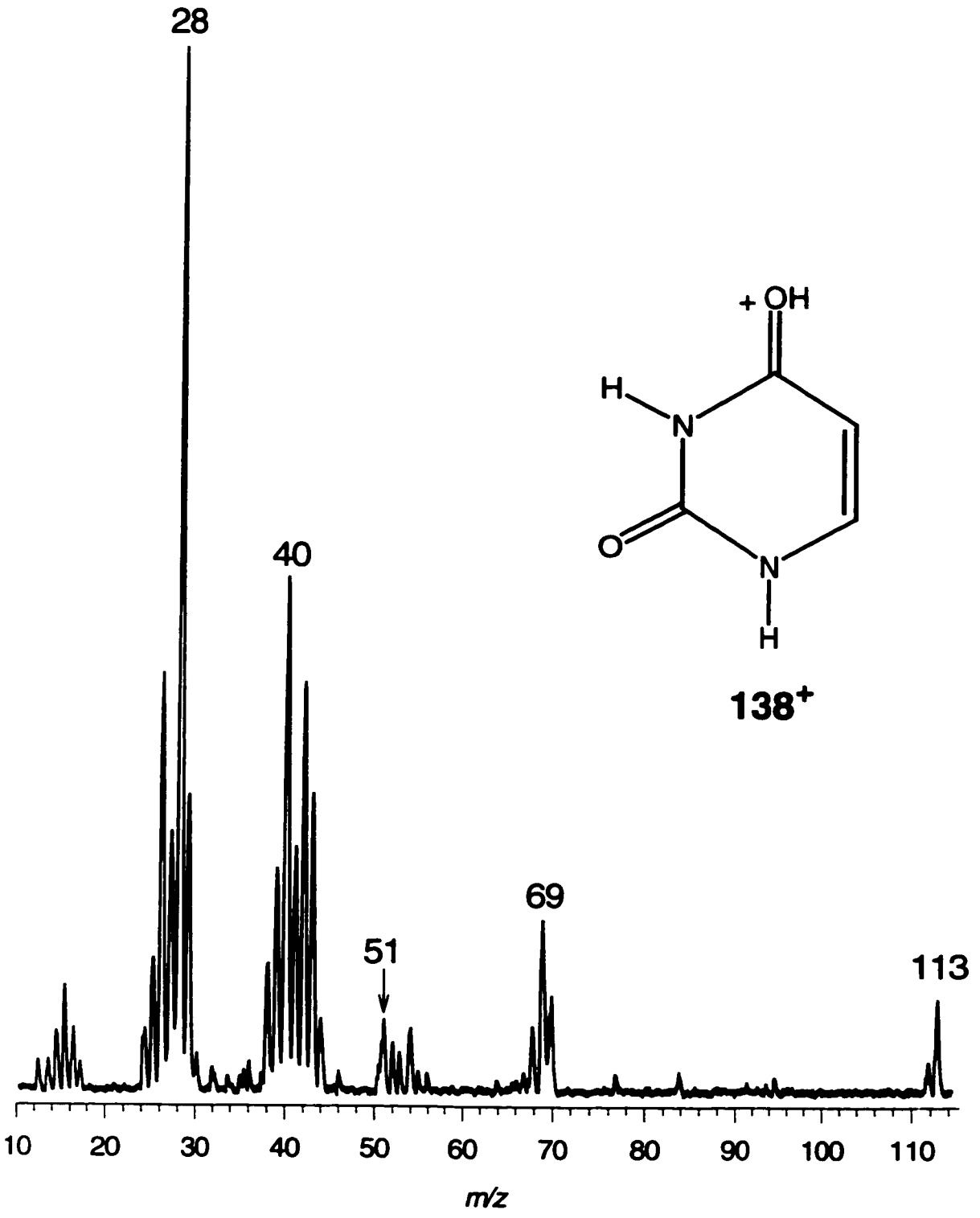

Figure 44. NRMS spectra of **13** protonated with NH_4^+, full spectra

Radical Energetics:

To further investigate **138•** and **137•**, *ab initio* and DFT calculations were used to study the relative energies of radicals derived from any tautomer of uracil in the ground electronic state. RRKM was used to investigate the dissociation kinetics from ring cleavages and hydrogen elimination reactions in order to further understand the dissociation pathways of uracil radicals.

The radicals derived from six tautomers of uracil were studied by several computational methods. Geometries were optimized and frequencies generated with UHF and with the 6-31G(d,p) basis set. The optimized structures for the most stable radicals are shown in Figure 44.

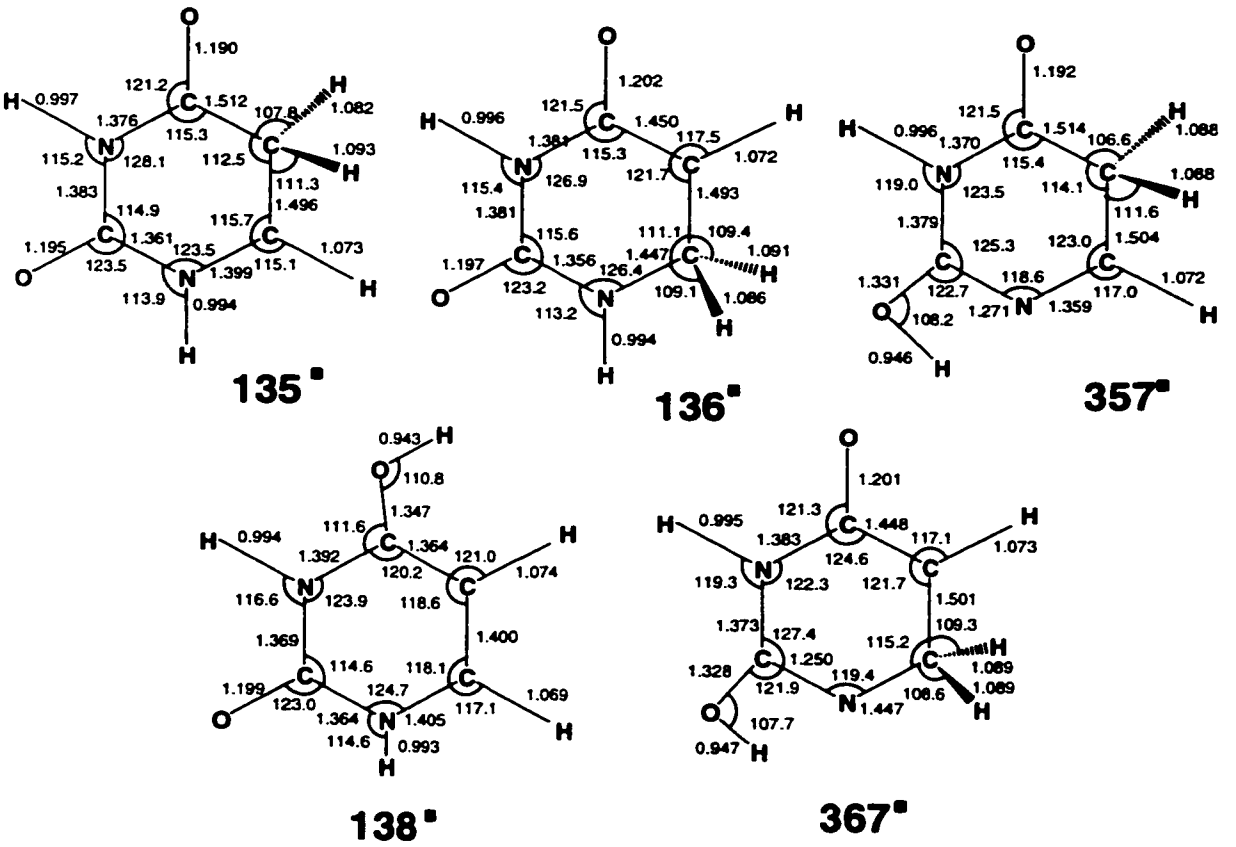

Figure 45. Optimized structures for the most stable radical structures

All (uracil + H)• radicals from the uracil tautomers were investigated and it was found that the stability ordering of the radicals differed significantly from the ions. The most stable radical was **135•** for all levels of theory, followed by **136•**, **357•**, **138•**, and **367•** at 10, 41, 43, and 62 kJ/mol respectively (QCISD, 0 K). (Figure 46) It is also interesting to note that the radical corresponding to the most exothermically formed ion in the ion source (**138•**) was ranked fourth most stable at 46 kJ/mol (QCISD, 0 K) above **135•**. The other ion expected to form under stronger gas-phase conditions, such as protonation with acetone (**137•**) was 101 kJ/mol less stable than **135•** (QCISD, 0 K) indicating radical rearrangement could be energetically feasible to form the more stable radicals. It is also interesting that the most stable radicals (**135•**, **136•**, and **357•**) all have hydrogen additions on the ring carbon, and not on the more basic nitrogen and oxygen sites. The energy differences between ions and the energy difference between radicals are very similar. This would indicate uracil has less site specificity for both H^+ and $H^\bullet$ than that seen for the both **3** and **1,2** where H+ addition was much more site specific.

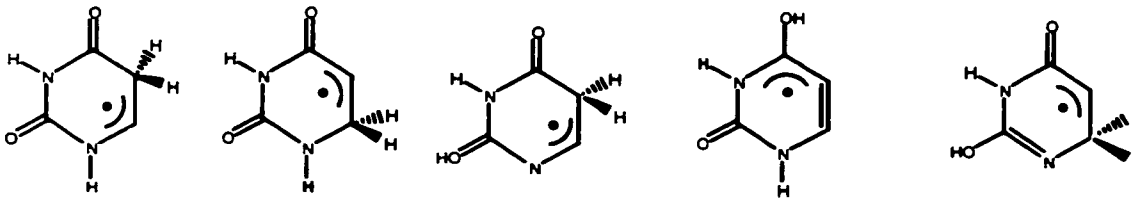

	135 •	136 •	357 •	138 •	367 •
1)	0/0	11/9	41/39	48/41	65/65
2)	0/0	10/9	40/38	42/36	63/63
3)	0	10	42	46	63
4)	0	10	41	43	62

1) MP2/B3LYP 6-311G(2d,p) 298K
2) MP2/B3LYP 6-311+G(2d,p) 298K
3) QCISD 6-311+G(2d,p) 298K
4) QCISD 6-311+G(2d,p) 0K

Figure 46. Radical Energetics

Transition State Energies:

Radical dissociations by hydrogen elimination and ring cleavage were also addressed by various computational methods for **138•** and **137•**. The relative energies for **138•** by loss of hydrogen elimination are shown in Figure 46. There are two sets of calculations shown for hydrogen elimination from **138•**. The first is the extrapolated QCISD as described in eq. 4 from projected MP2 (PMP2) calculations. The second is also extrapolated QCISD, but used restricted open shelled MP2 calculations (ROMP2) rather than the projected. The restricted open-shelled MP2 method is spin accurate and is not contamination from higher order spin states. The projected MP2 calculation is encumbered by higher spin states and thus corrects the energy for the excess spin. In the following discussion, both QCISD energies will be shown as $QCISD_{PMP2}$ / $QCISD_{ROMP2}$ at 0 K respectively. All transition state calculations were optimized at the RHF/6-31+G(d,p), and single points were done at (U)HF/B3LYP 6-311G(2d,p) and (U)HF/B3LYP 6-311+G(2d,p) as well as the extrapolated QCISD with PMP2 and ROMP2. As is sometimes the case, the lower basis set showed a saddle point based on frequency calculation but when higher calculations were performed, the products were even higher than the presumed barrier. However, the optimized structures and kinetic dissociations are shown for these pseudo-barriers for completeness sake, but for discussion of reaction pathways, the energies of the highest point is considered, which for the pseudo-transition states is the reaction products.

The relative energies at 0 K are summarized in a potential energy diagram for loss of hydrogen from **138•**. The lowest energy pathway for **138•** to lose hydrogen is by loss of the O8 hydrogen to form the lowest energy tautomer **13**. Dissociation of the O8-H bond in **138•** showed a transition state at d(O-H) = 1.402 Å. The energy barrier (E_{O-H}) for **TS1** was 130 / 134 kJ/mol (depending on theory) where **13** + H• is at 80 / 83 kJ/mol. (Figure 46) The optimized structure for transition states 1-6 are shown in Figure 48.

Dissociation of the N3-H bond in **138•** reached a transition state at 1.573 Å (**TS2**). The **TS2** energy (E_{N3-H}) was calculated at 189 / 192 kJ/mol above the energy for

138• to form **18** + H• at 131 and 133 kJ/mol above **138•** which is substantially higher than that seen for loss of N1-H bond.

Dissociation of O8-H bond reached a transition state at d(O8-H) = 1.402 Å (**TS3**) based on UHF/6-31+G(d,p) geometry optimizations. However, once the single point energies were calculated, the products at both extrapolated QCISD values were higher in energy than **TS3**. The transitions state **TS3** was found at 150 / 154 kJ/mol above **138•**, while **38** + H• is 182 / 185 kJ/mol above **138•**. Therefore, while there may be a basis set superposition error for the existence of a transition state for loss of the O8 hydrogen, the energy for this cleavage is expected to be the thermochemical energy, or 182 / 185 kJ/mol. The optimized structure for **TS3** at the UHF/6-31+G(d,p) basis set is shown in Figure 47.

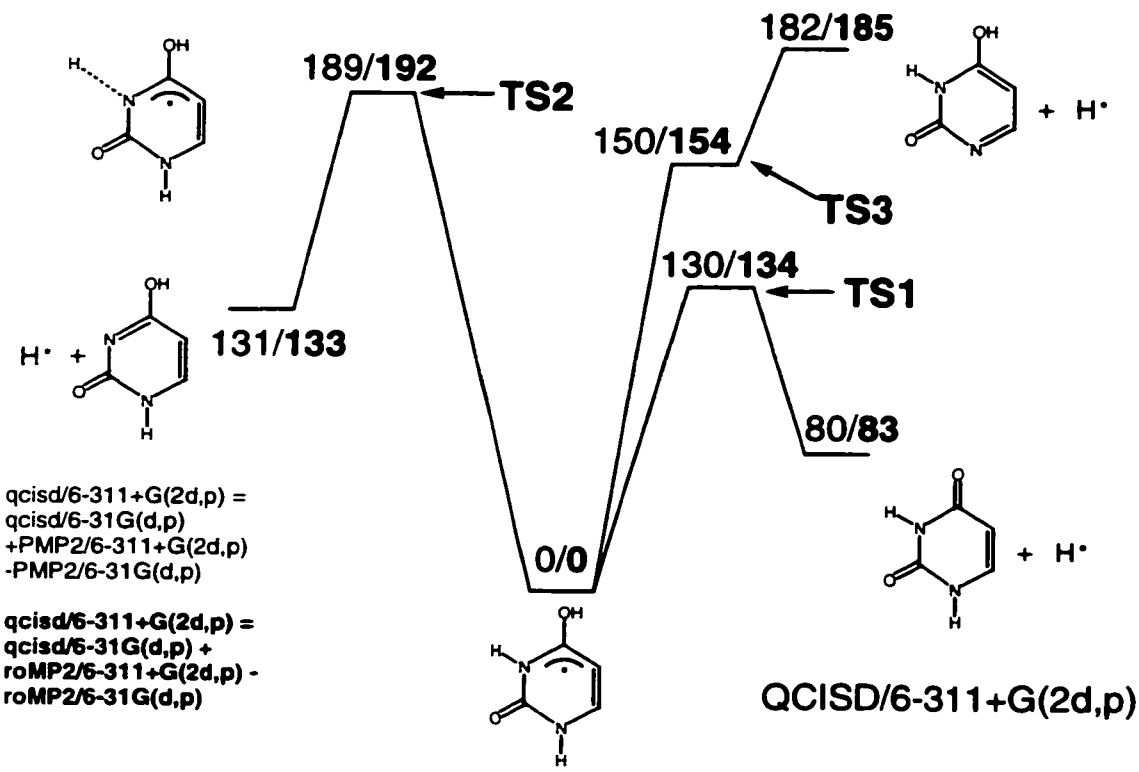

Figure 47. Energetics of hydrogen elimination for **138•**

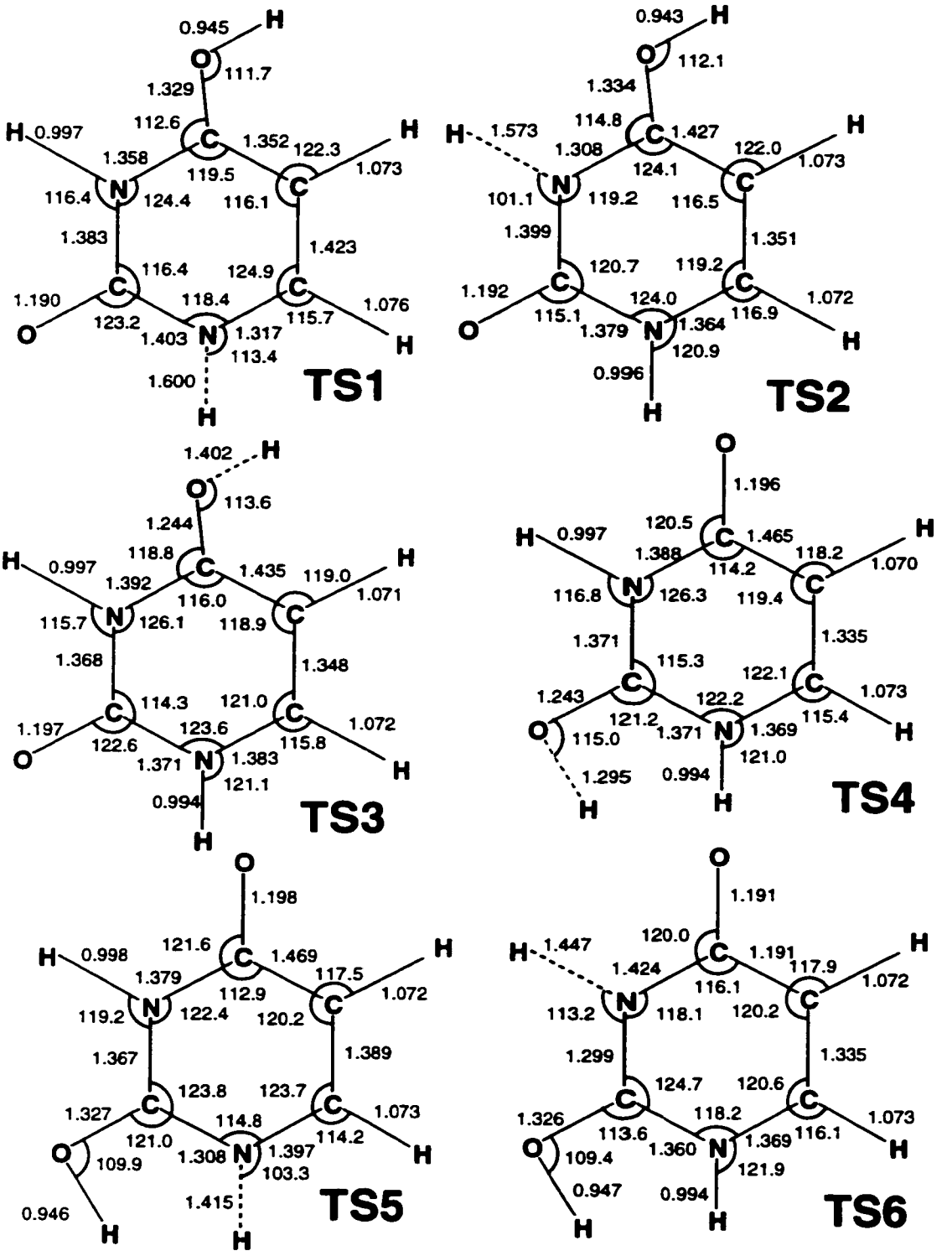

Figure 48. Optimized structures for loss of hydrogen from **138•** and **137•**

The relative energies at 0 K are summarized in a potential energy diagram for loss of hydrogen from **137•**. (Figure 49) There are two pathways for loss of hydrogen **137•** tied for the lowest reaction pathway. Dissociation of the O7-H bond in **137•** showed an early transition state at d(O-H) = 1.295 Å. The energy barrier ($E_{O\text{-}H}$) for **TS4** was 119 / 108 kJ/mol (depending on theory) where **13** + H• is at 23 / 12 kJ/mol above **137•**. (Figure 49) Dissociation of the N1-H bond in **137•** reached a transition state at 1.415 Å. The energy barrier ($E_{N1\text{-}H}$) for **TS5** was 119 / 109 kJ/mol with the products of **37** + H• at 69 / 58 kJ/mol.

Dissociation of the N3-H bond in **137•** reached a transition state at d(N3-H) = 1.447 Å (**TS6**). The **TS6** energy ($E_{N3\text{-}H}$) was calculated at 142 / 131 kJ/mol above the energy for **137•** to form **18** + H• at 99 and 88 kJ/mol above **137•** which is substantially higher than that seen for loss of either the N1-H or O7-H hydrogen.

In summary, the lowest energy barrier for hydrogen elimination from either **138•** or **137•** was a tie between losing the O7-H or the N1-H from **137•** at ~ 119 / 109 kJ/mol. The lowest hydrogen elimination from **138•** was loss of the O8-H at 130 / 134 kJ/mol to form **13** + H•.

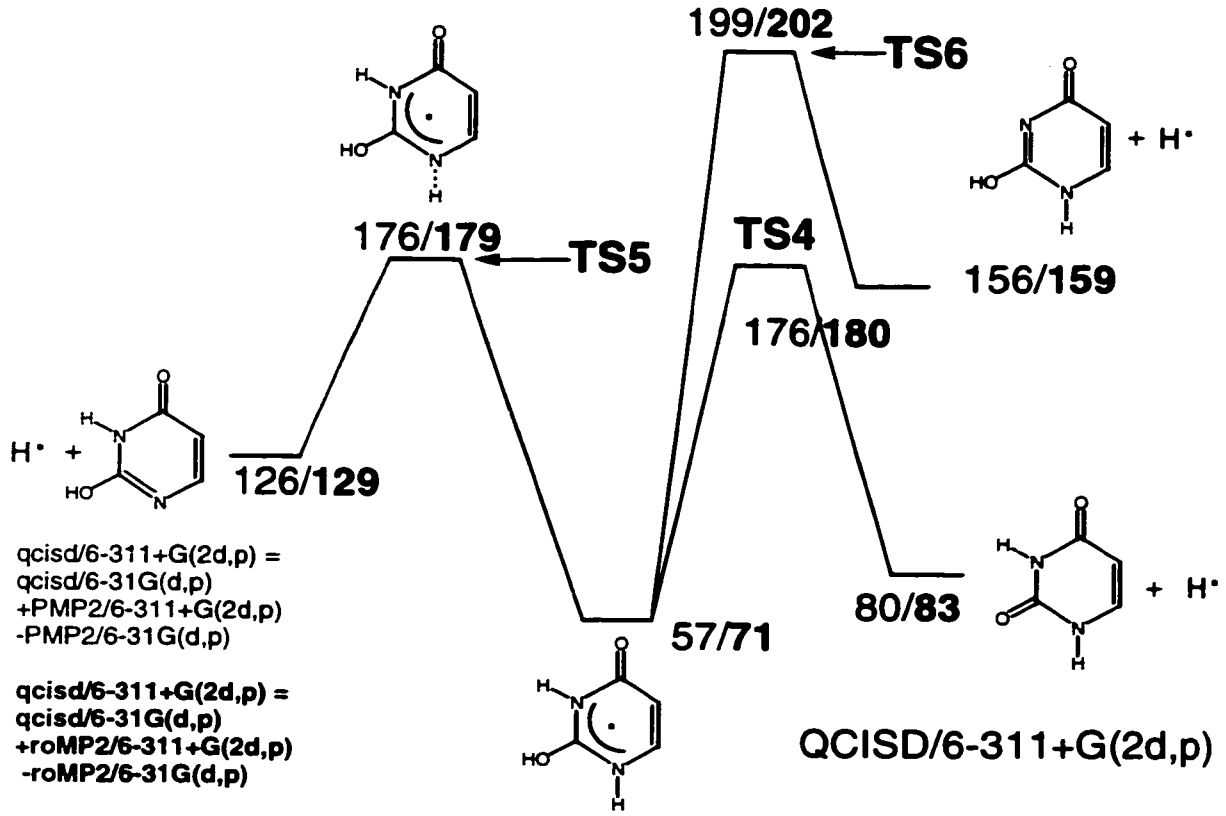

Figure 49. Hydrogen elimination energies for **137•**

Ring-cleavage reactions, which were readily apparent in the NR spectra were also investigated by computational methods. The transition states for bond cleavages were investigated in the same manner as the hydrogen eliminations. The lowest energy transition state was found when bond cleavage for **138•** elongated the N1-C2 bond. This reached a transition state (**TS7**) at d(N1-C2) = 1.870 Å. The (E_{N1-C2}) for **TS7** is 185 / 188 kJ/mol above **138•**. The open ring product is formed by cleaving the N1-C2 bond and rotating the N1 portion about the C5-C6 bond. This open ring product is 146 kJ/mol above **138•**. (Figure 50) The optimized structures for **TS7-TS10** are shown in Figure 51.

The second lowest energy transition state for bond cleavage in **138•** was found when elongating the C2-N3 bond. This reached a transition state (**TS8**) at d(C2-N3) = 2.010 Å. The (E_{C2-N3}) for **TS8** is 193 / 192 kJ/mol above **138•**. The open ring product is formed by cleaving the C2-N3 bond and rotating the C21 portion about the N1-C6 bond. This open ring product is 95 kJ/mol above **138•**.

Two other ring-cleavage fragmentations investigated led to significantly higher energy barriers. Cleavage of the N1-C6 bond reached a transition state at d(N1-C6) = 2.280 Å. The (E_{N1-C6}) for **TS9** was 285 / 287 kJ/mol above **138•**. Cleavage of the C4-C5 bond reached a transition state at d(C4-C5) = 2.500 Å. The (E_{C4-C5}) for **TS10** was 305 / 356 kJ/mol above **138•**. Either of these two ring-cleavage fragmentations were not energetically favored, and thus are not expected to fragment by either of these pathways.

It is interesting to note that the lowest fragmentation pathway for **138•** is the loss of hydrogen from the O8 position at 130 / 134 kJ/mol. The energies for the other fragmentations are fairly similar. Elimination of the N1-H, elimination of the N3-H, cleavage of the N1-C2 bond, and cleavage of the C2-N3 bond are at ~ 182, 189, 185, and 193 kJ/mol respectively ($QCISD_{PMP2}$, 0 K). It is expected that the loss of hydrogen would be the favored pathway, and the energetics from **138•** does not explain the significant ring cleavages seen in the NR spectrum.

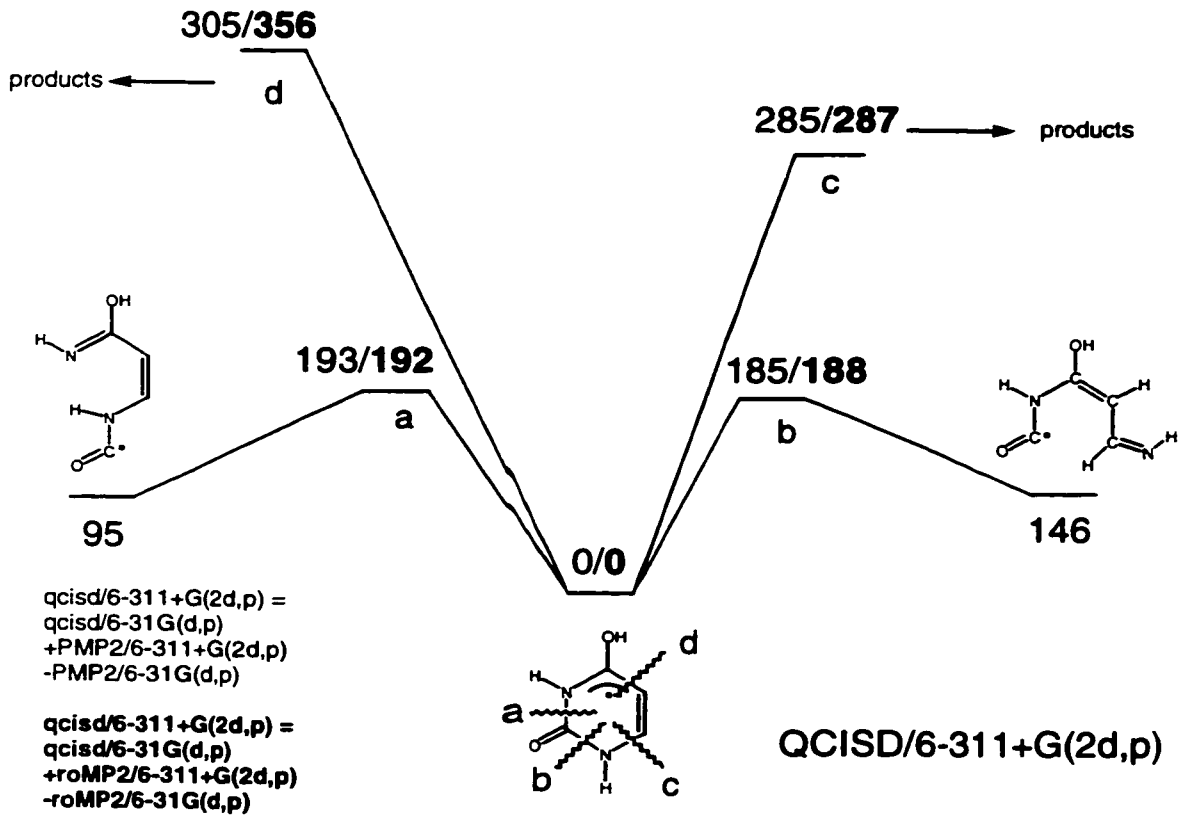

Figure 50. Ring cleavage reactions for **138•**

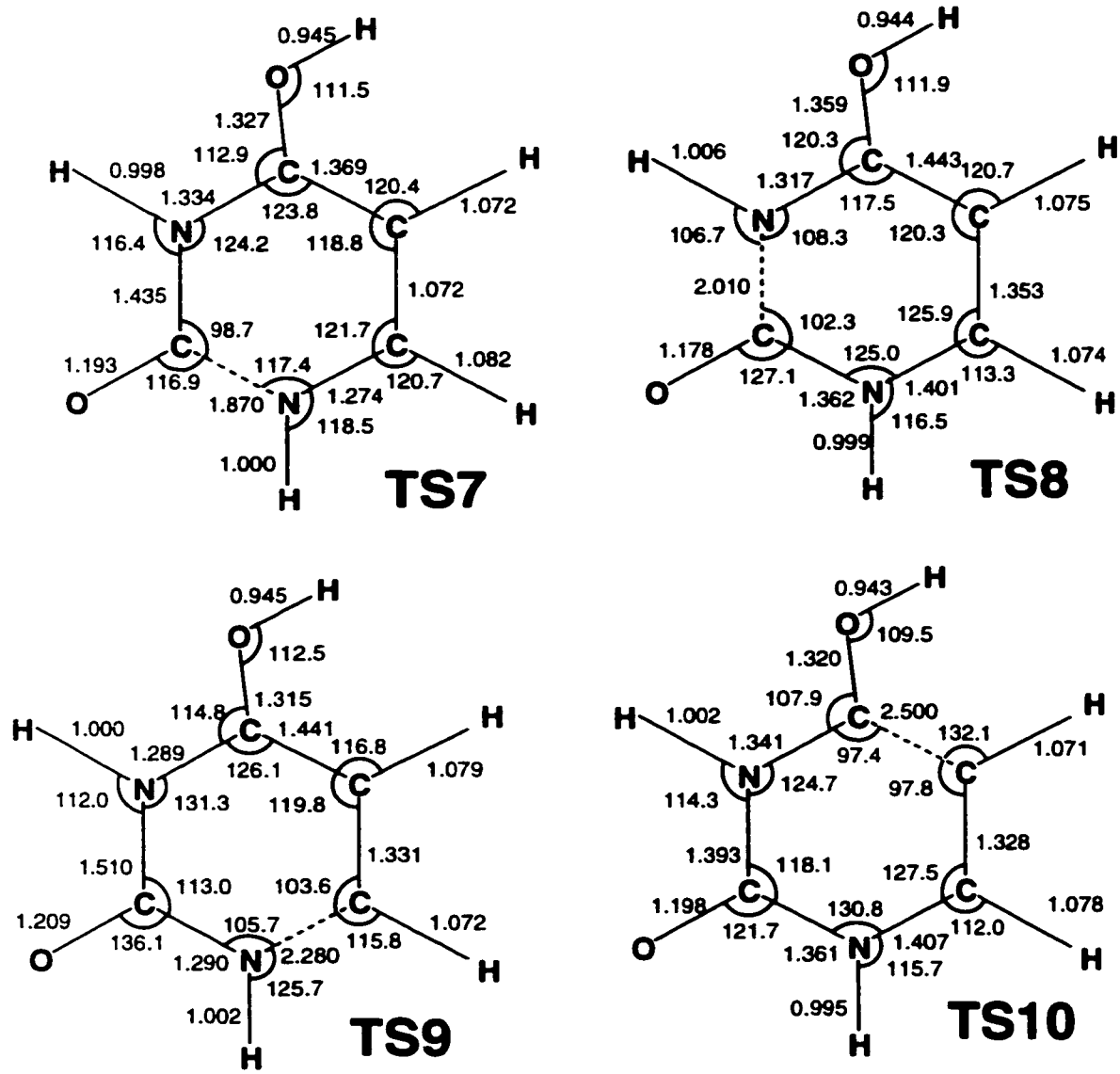

Figure 51. Optimized structure for ring cleavage transition states from **138•**

Energetics of ring cleavage fragmentation pathways from 137• were also investigated and showed an altogether different result. The lowest energy bond cleavage transition state for **137•** is elongating the N3-C4 bond. This reached a transition state (**TS11**) at d(N3-C42) = 1.930 Å. The (E_{N1-C2}) for **TS11** is 89 / 76 kJ/mol above **137•**. The ring cleavage reaction pathway is significantly lower in energy than any of the hydrogen eliminations from **137•**. There are two open ring products shown for cleavage of the N3-C4 bond. (Figure 52). The first with a simply cleavage and no rotation about any bond is 153 kJ/mol above **137•**. (Figure 53) However, a rotation about the N1-C6 bond forms an open ring product at 122 kJ/mol above **137•**. The optimized structure for **TS11-TS14** are shown in Figure 53.

The second lowest energy bond cleavage transition state for **137•** is elongating the N1-C6 bond. This reached a transition state (**TS12**) at d(N1-C6) = 1.930 Å. The (E_{N1-C6}) for **TS12** is 173 / 162 kJ/mol above **137•**.

The third lowest energy bond cleavage transition state for **137•** is elongating the N1-C2 bond. This reached a transition state (**TS13**) at d(N1-C2) = 2.060 Å. The (E_{N1-C6}) for **TS13** is 185 kJ/mol above **137•** ($QCISD_{PMP2}$ 0K). However, the open ring products investigated at this level of theory were higher in energy than **TS13** at 229 kJ/mol. Therefore, in order to cleave this bond, the system must have enough energy to form the products above **TS13**.

The highest energy bond cleavage transition state for **137•** is elongating the C2-N3 bond. This reached a transition state (**TS14**) at d(C2-N3) = 2.220 Å. The (E_{C2-N3}) for **TS14** is 227 / 216 kJ/mol above **137•**. However, the open ring products investigated at this level of theory were higher in energy than **TS14** at 257 kJ/mol. Therefore, in order to cleave this bond, the system must have enough energy to form the products above **TS14**.

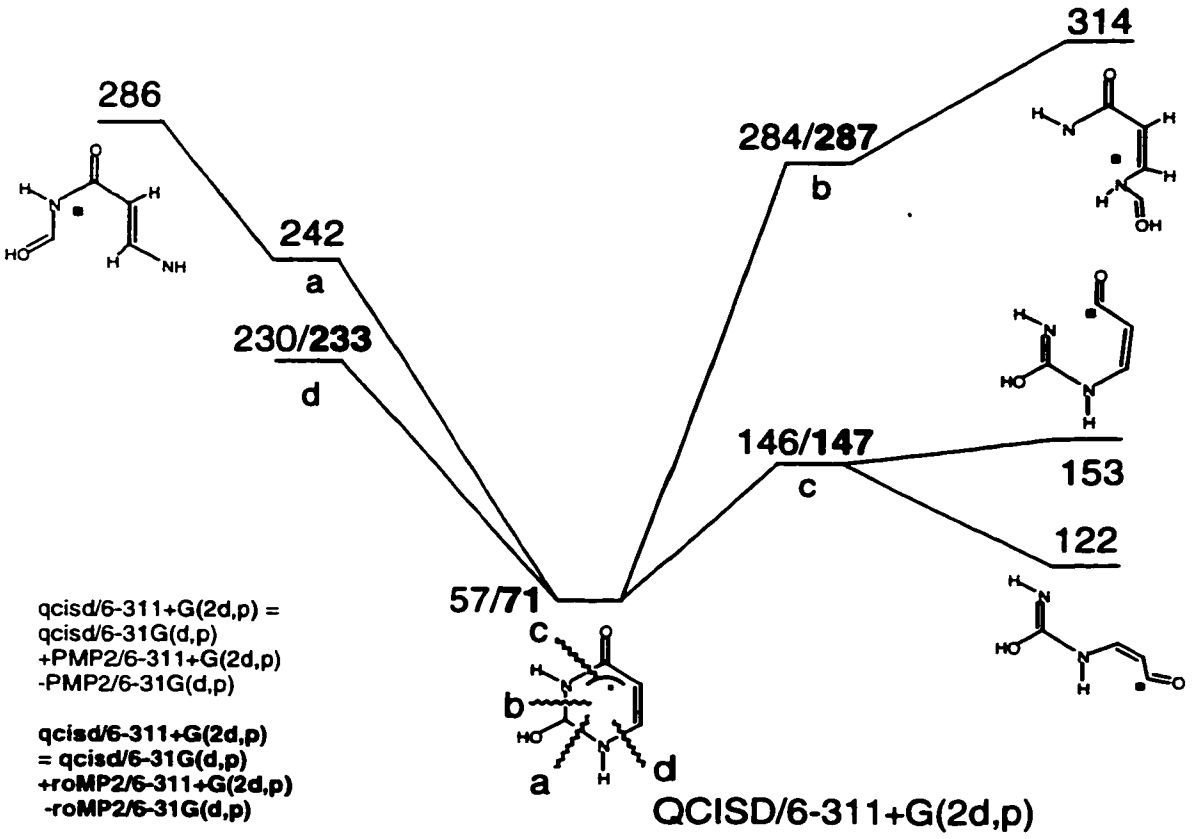

Figure 52. Ring cleavage fragmentation energetics for **137•**

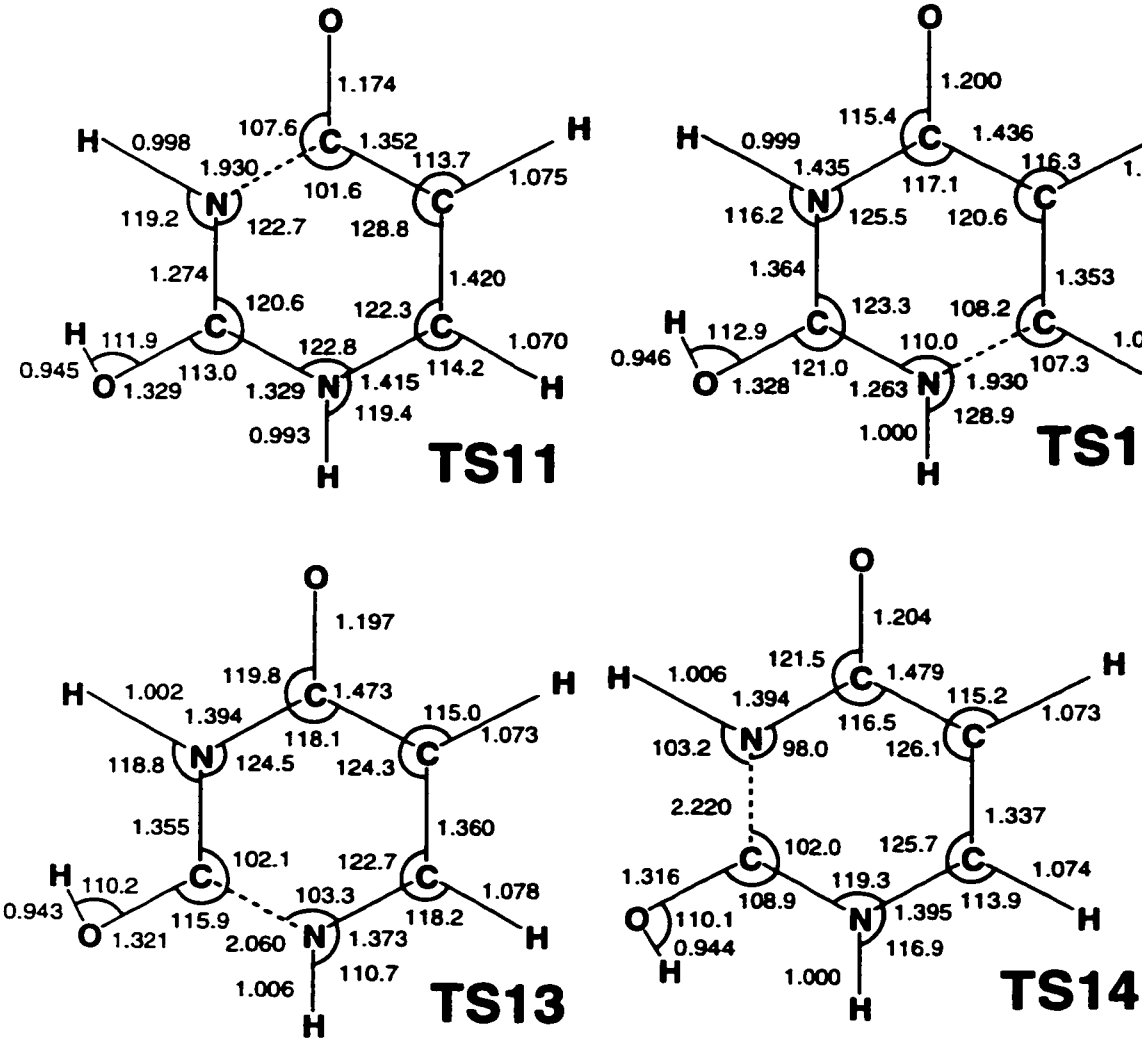

Figure 53. Optimized structure for ring cleavage transition states from **137•**

Table 12. Summary of Transition State energetics

138• Hydrogen elimination	Energy Barrier	137• Hydrogen elimination	Energy Barrier
H-N1	NA (182 / 185)	H-N1	119 / 108
H-N3	189 / 192	H-N3	142 / 131
H-O8	130 / 134	H-O7	119 / 109
Ring cleavage		Ring cleavage	
N1-C2	193 / 192	N1-C2	NA (229 / NA)
C2-N3	185 / 188	C2-N3	NA (227 / 216)
C4-C5	305 / 356	N3-C4	**89 / 76**
N1-C6	285 / 287	N1-C6	173 / 162

NA means not available and no barrier was found. The numbers represents the energy of the product. $QCISD_{PMP2}$ / $QCISD_{ROMP2}$

Breaking of the N3-C4 bond in **137•** has the lowest energy barrier for all reaction pathways investigated at 89 / 76 kJ/mol above **137•**. The second lowest energy pathway for **137•** was either by loss of N1-H or loss of O7-H at ~ 119 / 109 kJ/mol above **137•**. However, breaking the N3-C4 bond does not create any fragmentation since this is an isomer of **137•**. Investigation of the dissociation pathways from **137•** was investigated to determine if any pathway was low enough in energy to compete with the hydrogen elimination pathways. (Figure 54) It was found that while the barrier for the N3-C4 bond cleavage was low (146 kJ/mol), the energies of the various products were in fact much higher. Opening of the ring at the N3-C4 position created two open ring products. The higher energy products was at 153 and was a simple cleavage of the N3-C4 bond while the lower energy product were at 122 kJ/mol and rotating about the N1-C6 bond. However, fragmentation from either of the open ring products was significantly endothermic. (Figure 54)

In conclusion, the lowest energetic pathway for **138•** was cleavage of the O8-hydrogen above any ring cleavage. The lowest activation barrier for **137•** was cleavage of the N3-C4 bond. However, the products are significantly endothermic that hydrogen cleavage from **137•** is also expected to be the preferred fragmentation pathway. In order to understand the reaction pathways more thoroughly, the kinetics of the various reactions must be investigated as well to determine if a ring cleavage is a kinetically viable reaction pathway. To this end, RRKM kinetic calculations were performed on all transition states determined.

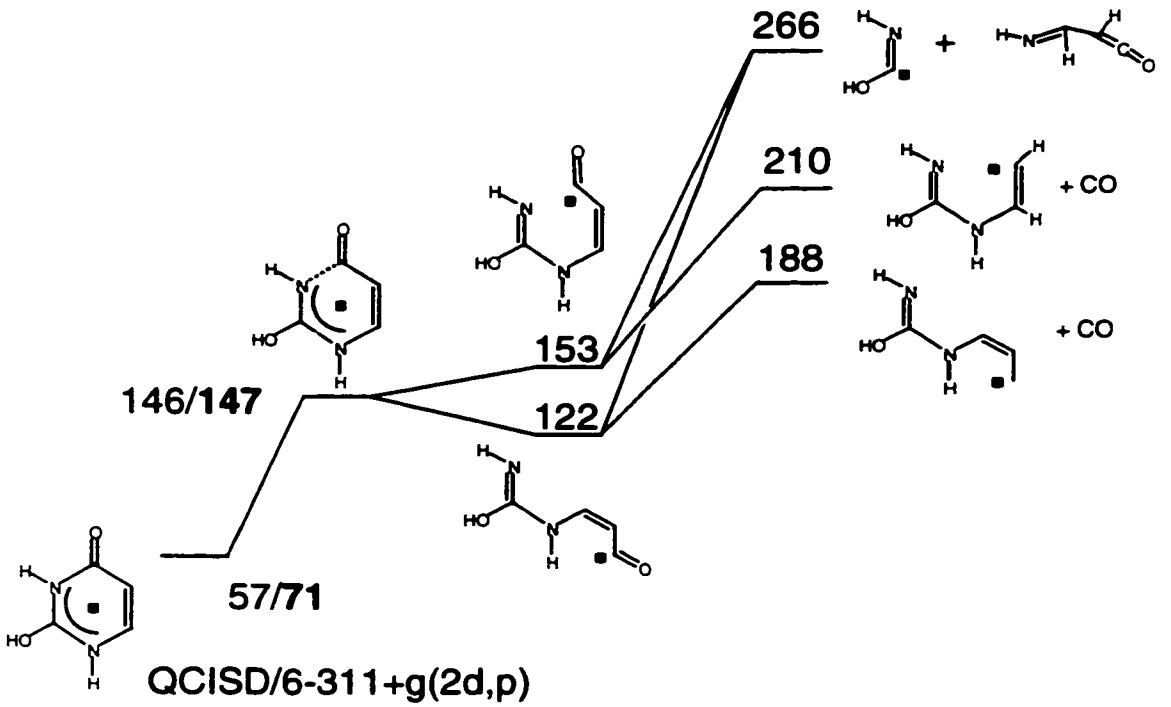

Figure 54. Dissociation products of **137•** by cleavage of the N3-C4 bond

Dissociation Kinetics:

The calculated transition state energies allowed us to estimate the unimolecular rate constant (k_{uni}) for all of the hydrogen eliminations and ring cleavages from **138•** and **137•**. While it has been predicted that energetically the most stable fragmentation pathway from either radical is cleavage of the N3-C4 from **137•**, it is essential to understand the kinetics of this reaction since there is a limited time scale in which the NR spectrum has been acquired.

The calculated k_{uni} for all reactions derived from **138•** is shown in Figure 53. The rate constants were determined based on QCISD 0 K calculation from the transition states. The fastest dissociation (the dissociation with the largest k_{uni}) from **138•** is loss of O8-H at all energies performed resulting in the most stable **13** tautomer + H•. This pathway is followed by N1-H, N3-H, N1-C2, C2-N3, followed by N1-C6. At ~15 kJ/mol, k_{uni} for N1-C2 and C2-N3 cross, so C2-N3 is a faster dissociation than N1-C2 at higher energies. However, at all energies investigated, EVERY hydrogen elimination is faster than any ring cleavage.

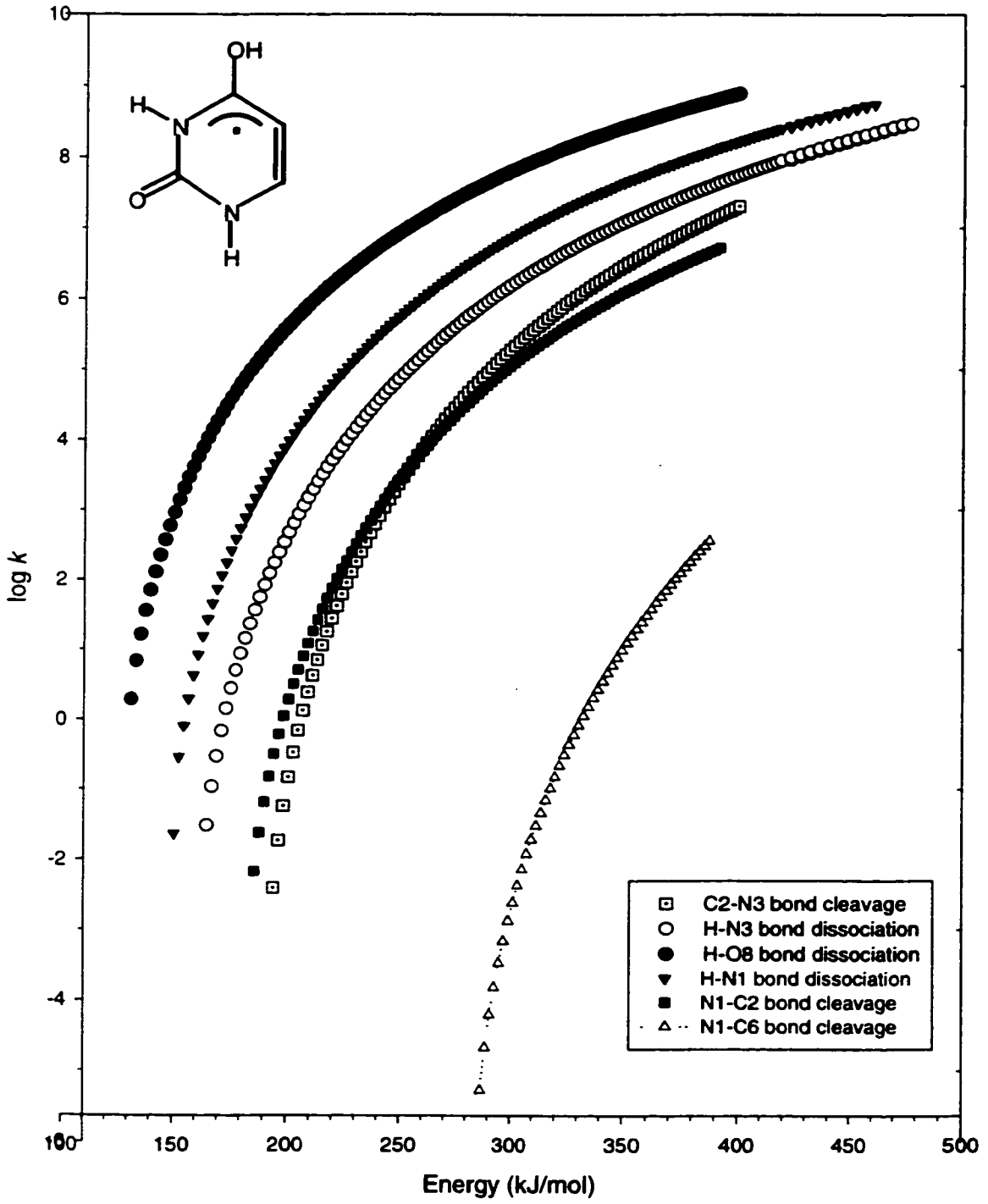

Figure 55. RRKM rate constants for hydrogen eliminations and ring cleavages of **138•**

The calculated k_{uni} for all reactions derived from **137•** is shown in Figure 54. The rate constants were determined based on QCISD 0 K calculation from the transition states. At ~ 5-6 kJ/mol, there is similar dissociation kinetics for loss of O7-H and cleavage of the N3-C4 bond. At higher energies, the cleavage of the N3-C4 bond is clearly a faster dissociation pathway than the O7-H bond dissociation. These pathways are followed by N1-H, N3-H, N1-C6, N1-C2, and C2-N3 respectively.

In conclusion, from RRKM calculations, the fastest dissociation pathway from **138•** is by loss of the O7-H, followed by all other hydrogen eliminations. Therefore, the ring cleavage fragmentation seen in the NR spectra are not expected to occur from **138•**, but rather from **137•** where the fastest dissociation is cleavage of the N3-C4 bond.

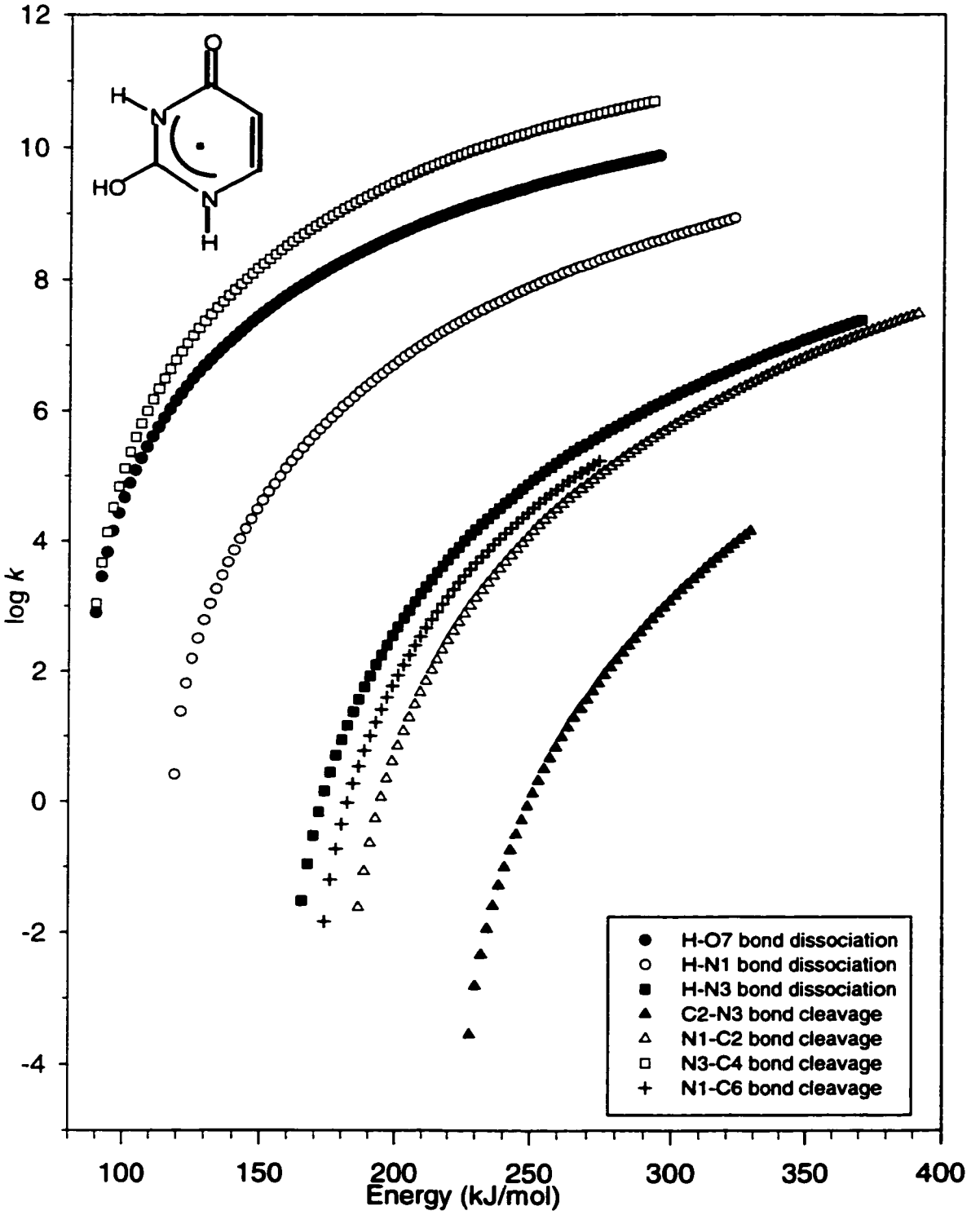

Figure 56. RRKM rate constants for hydrogen eliminations and ring cleavages of **137•**

Conclusions:

Six tautomers of uracil were investigated and it was found uracil **13** is the most stable uracil tautomer. The most basic site in uracil is the O8, with a close second on the O7 site. The experimental and computational data were in accord that **138•** was a stable species in the gas phase. Hydrogen addition to O7 and O8 from uracil **13** were associated with potential energy barriers. Addition of a hydrogen atom to O8 was energetically preferred. Significant ring opened products were present in the NR spectrum indicating a reaction pathway opening the uracil ring. Investigation of **138•** showed hydrogen elimination as the preferred reaction pathway, both energetically and kinetically. Investigation of **137•** however, showed cleavage of the N3-C4 bond both energetically and kinetically preferred. However, fragmentation along this pathway was significantly endothermic. Therefore, it is expected that hydrogen elimination from either **138•** or **137•** is the preferred reaction pathway.

Chapter VI. Additional Work

This chapter is dedicated to other work I accomplished. This first part focuses on computational aspects of cytosine. The radicals were not investigated thoroughly, so more work is needed before cytosine radicals and their reaction pathways can be reasonably understood. However, the framework has already been started and presented here.

The following sections are dedicated to projects in which I partook, although I was not the primary researcher. These sections include the abstracts for papers which were previously published. The aminopyrimidine study was recently published in *J. Phys. Chem. A.*.[31] The pyridyl cations and radicals study was published in *Euro. Mass Spectrom.*,[63] while the alkenylammonium cation work was published in *J. Am. Soc. Mass Spectrom.*.[64]

The last section is dedicated to my initial work in the Turecek group. It focuses on the hypervalent radicals of 1,4-diazabicyclo[2.2.2]octane (Dabco).[65] Included is the abstract which was published in *J. Mass Spectrom.*.

Due to the nature of this chapter, the naming scheme for cations and radicals is section dependent and on occasion symbols are duplicated from one section to the next or coincide with the naming scheme for 3-hydroxypyridine and 2-hydroxypyridine / 2-(1H)pyridone.

Cytosine:

In addition to the 3-hydroxypyridine (**3**) system, 2-hydroxypyridine/2-(1H) pyridone (**1,2**) model systems, and uracil, cytosine was also investigated, although not to the same extent as uracil. Cytosine has 4 tautomers present in the gas phase and the possibility of gas-phase isomerization. In this section, cytosine ions and radicals were studied predominantly through computational methods such as *ab initio* and DFT to study reaction energetics.

Numerous ion and radical structures are discussed in the following text, which are even more complicated since cytosine has 4 different tautomers shown as **A-D** (Figure 56) and many more ions and radicals derived from each of these tautomers. For clarity, a system has been developed. The ring sites (1,2,3,4,5,6) refer to N1, C2, N3, C4, C5, and C6 respectively. Since there is one oxygen in cytosine which resides on C2, no other nomenclature beside O is needed. The nitrogen on C3 is designated N7. Ions and radicals are designated by the tautomer letter followed by the position the hydrogen resides. For example, $\mathbf{AN_3H^+}$ indicates an ion formed by protonation of the N3 position from tautomer **A**.

Every calculation was performed with both ab initio theory and DFT theory. The basis set used for single point energies was 6-311G(2d,p).

Tautomer Stability:

Four tautomers of cytosine were studied using *ab initio* and DFT calculations. Geometries were optimized and frequencies generated at the 6-31G(d,p) basis set. The most stable tautomer was basis set dependent. By MP2/6-311G(2d,p), **A** is the most stable by 4 kJ/mol. However, based on B3LYP/6-311G(2d, p) calculations, **B** is more stable than **A** by 4 kJ/mol. (Figure 57) Tautomer **C** is less stable by 17 / 15 kJ/mol, and tautomer **D** is even less stable at 33 / 28 kJ/mol. The assumption is that both **A** and **B** are present in the ion source, while isomerization to **C** or **D** is unlikely. It may also be further assumed that **A** and **B** are present in roughly equal amounts were the relative amounts of **C** and **D** are negligible. The optimized structures for the cytosine tautomers are shown in Figure 58.

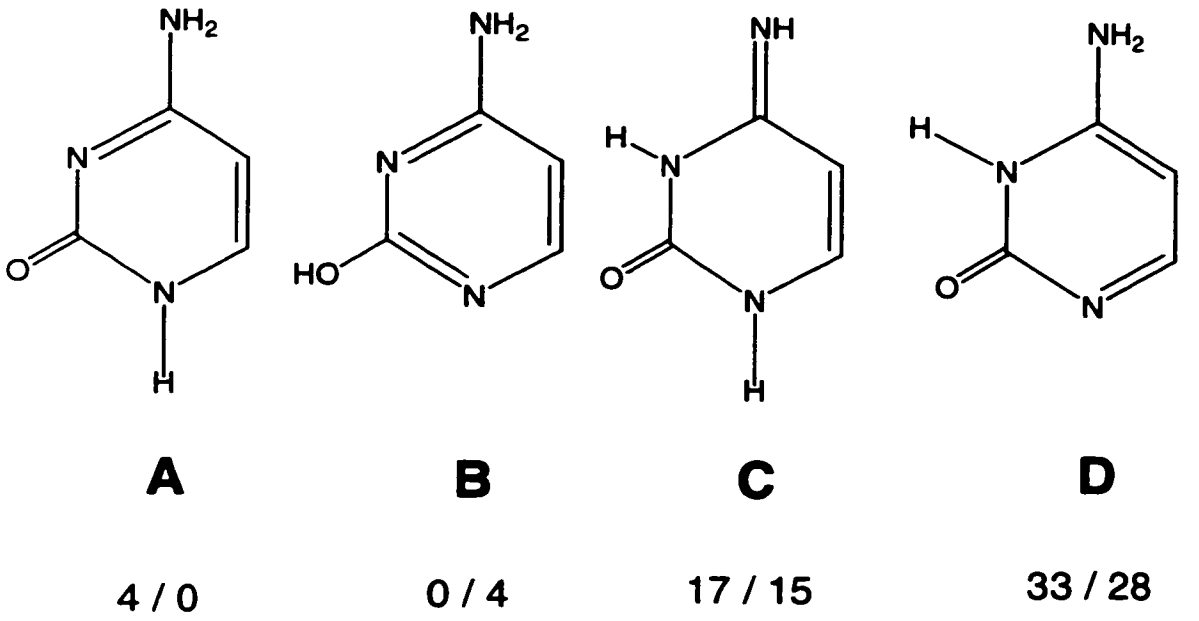

Figure 57. Cytosine tautomer energetics MP2 / B3LYP 6-311G(2d,p)

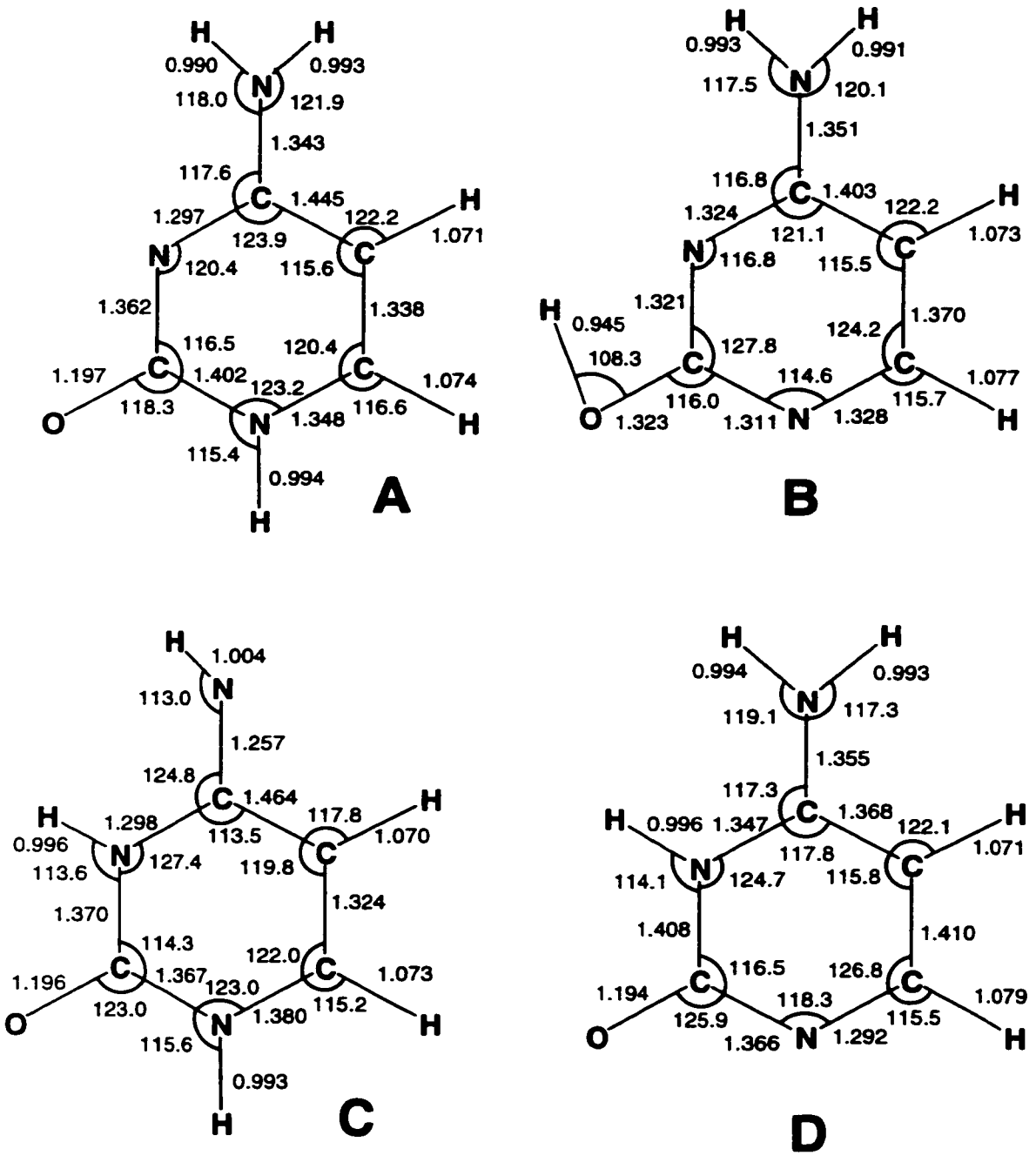

Figure 58. Optimized structures for cytosine tautomers

Ion Stability:

The ions derived from six tautomers of uracil were studied using numerous computational methods. Geometries were optimized and frequencies generated at the 6-31G(d,p) basis set. All ions derived from any cytosine tautomer was examined by MP2 and B3LYP at the 6-311G(2d,p). The most stable six ions optimized are shown in Figure 59.

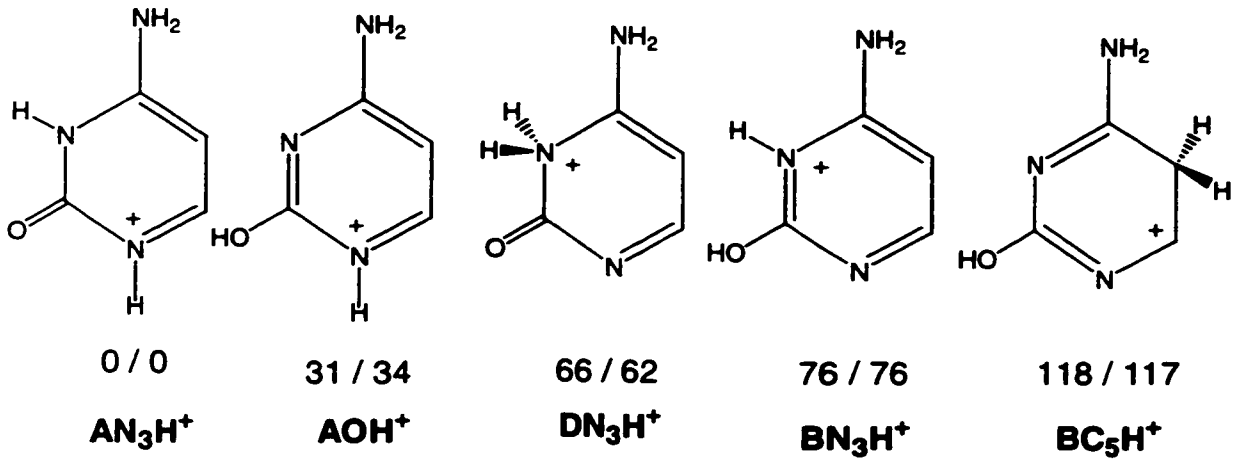

Figure 59. Cytosine ion energetics

The most stable ion is AN_3H^+ (which coincidentally could be made by protonation of N1, N3 or N7 from **D**, **A**, or **C** respectively). The second most stable ion is AOH^+ (also formed by protonation of N1 from **B**) at 31 / 34 kJ/mol above AN_3H^+. The other most stable ions are DN_3H^+, BN_3H^+ and BC_6H^+ by 66, 76, and 118 kJ/mol respectively. Of the top 5 ions, only the third most stable (DN_3H^+) could not be formed by the **A** and **B** tautomers expected to be present in the ion source. Three ions were not optimized due to hydrogen rearrangement. AC_6H^+, BC_6H^+, and DC_6H^+ all rearranged by hydrogen transfer to the carbon 5 position.

Ion Formation:

The proton affinities for each site in cytosine are listed in Table 13.

Table 13. Proton affinities[a] for positions in each tautomer of cytosine

A	N1	N3	C5	O	N7	
MP2	803	962	839	931	841	
B3LYP	809	975	847	941	837	
B	N1	N3	C5	O	N7	
MP2	927	882	840	778	838	
B3LYP	945	902	862	782	835	
C	N1	N3	C5	C6	O	N7
MP2	799	786	811	608	851	969
B3LYP	772	788	819	649	860	983
D	N1	N3	C5	O	N7	
MP2	984	918	872	909	768	
B3LYP	996	934	876	920	763	

[a]298K
6-311G(2d,p)

The most basic site in A is the N3 position. Protonation of N3 on **A** would result in formation of $\mathbf{AN_3H^+}$ which is the most stable ion. The most basic site in **B** is the N1 position. Protonation of N1 from **B** would result in formation of $\mathbf{BN_1H^+}$ which is the second most stable ion. Therefore, unlike the model compounds or uracil where there was either a convergence to a single ion product or a single tautomer present in the gas-phase, cytosine would be expected to have a mixture of the 2 most stable ions.

Radical Dissociation

Cytosine was collisionally neutralized and studied by neutralization – reionization mass spectrometry. The NR spectra (Figure 60a) showed a strong non-dissociating (or survivor ions) signal (*m/z* 111) which indicated that fractions of intermediate cytosine radicals were formed that had lifetimes greater than the flight time between neutralization and reionization (~ 5.1 μs). Upon collision of the neutrals with 50% He, the NCR spectra was obtained. The NCR spectra (Figure 60b) is interesting in how similar it is to the NR spectra. While there are greater fragmentations for the ring cleavages as seen in the intensity increase for *m/z* 28, *m/z* 40, and *m/z* 68. However, no new reaction channels were reached by collisional activation of the radicals.

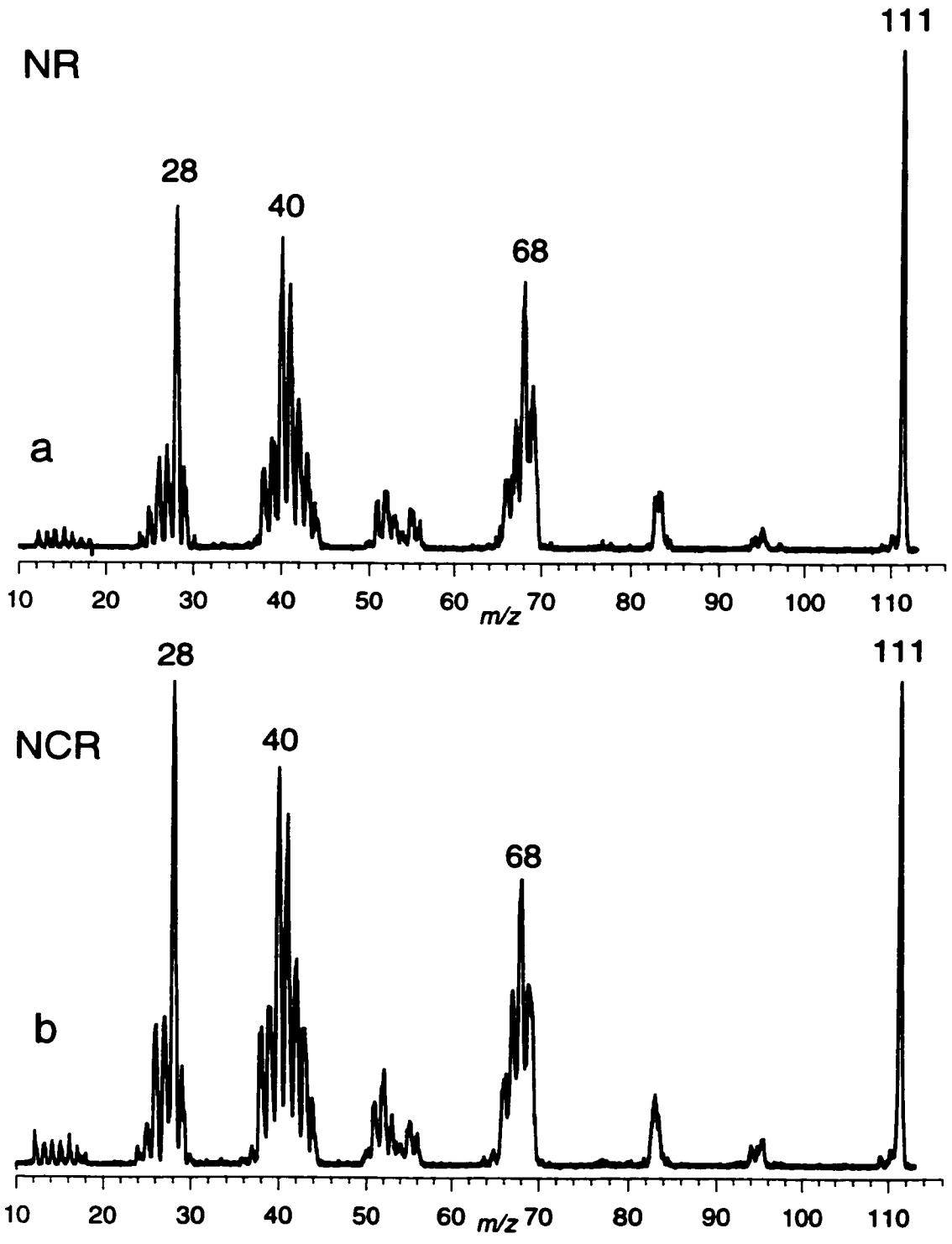

Figure 60. top) NR of cytosine bottom) NCR (50%He) of cytosine

Radical Energetics:

To further investigate cytosine radicals, ab initio and DFT calculations were used to study the relative energies of radicals derived from any tautomer of cytosine in the ground electronic state.

The radicals derived from the four tautomers of cytosine were studied by several computational methods. Geometries were optimized and frequencies determined with UHF at the 6-31G(d,p) basis set.

All (cytosine + H)$^{\bullet}$ radicals from the cytosine tautomers were investigated and it was found that the ordering from the ions differed, although not as significantly as that seen for uracil. The most stable radical was **$AN_3H\bullet$** for all levels of theory followed by **$CC_6H\bullet$**, **$CC_5H\bullet$**, **$BC_6H\bullet$**, and **$BC_5H\bullet$** at 20, 23, 33, and 38 kJ/mol respectively (UMP2 273K). (Figure 61) The most stable radical (**$AN_3H\bullet$**) is formed by electron collision of the most stable ion. This ion (**AN_3H^+**) is derived from one of the most stable tautomers present in the ion source (**A**). Therefore, the ion is expected to be formed in the ion source by protonation of **A** on the N3 position. This ion is not expected to rearrange to form any less stable ion. The corresponding radical is also not expected to rearrange to other least stable radicals. It is interesting that the more stable radicals (**$CC_6H\bullet$**, **$CC_5H\bullet$**, **$BC_6H\bullet$**, and **$BC_5H\bullet$**) all have hydrogen additions on the ring carbon, and not on the more basic nitrogen or oxygen site. This is a similar result seen as that seen for uracil, but not seen for any model compound, indicating the similarities between cytosine and uracil are closer than that for the model compounds and the pyrimidine bases.

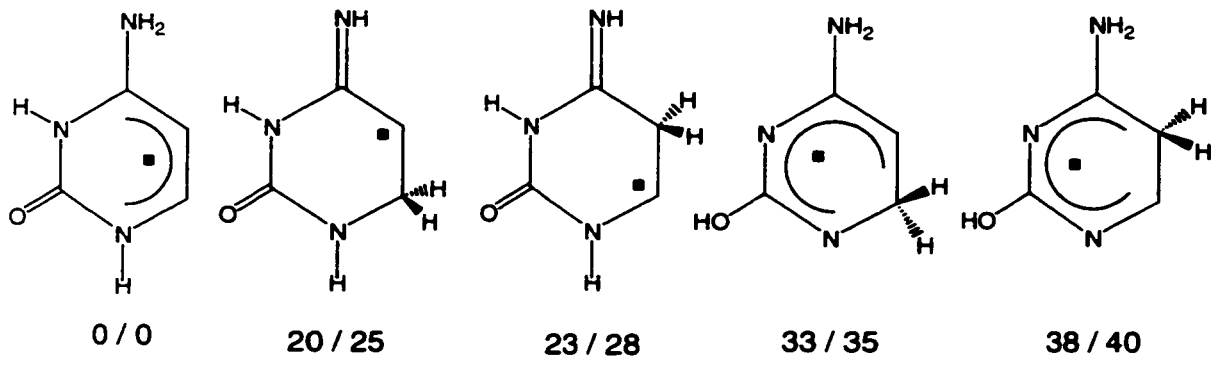

Figure 61. Radical energetics for cytosine

In conclusion, while the cytosine ions have been initially investigated, there is much work to be done before any conclusions about cytosine radicals can be discussed. Energetic and kinetic understanding of fragmentation pathways of cytosine radicals has not been investigated.

Aminopyrimidine

A series of isomeric 4-aminopyrimidinium radicals were used to model hydrogen atom adducts of nucleobases containing the 4-aminopyrimidine structure motif. Relative stabilities and activation energies for dissociations by hydrogen atom loss have been calculated by density functional theory and *ab initio* methods up to effective QCISD(T)/6-311+G(2d,p) for 4-amino-N-1-H- (**1**), 2-H- (**2**), N-3-H- (**3**), 4-H- (**4**), 5-H- (**5**), and 6-H- (**6**) pyrimidinium radicals and the 4-pyrimidylammonium radical (**7**). All these radicals were found to be bound species existing in potential energy wells. The order of stabilities has been established as **5** (most stable) > **3** > **2** > **1** > **6** > **4** >>**7** (least stable). Dissociations of the N-H and C-H bonds in **1**-**7** required activation barriers above the dissociation thresholds. RRKM calculations of unimolecular rate constants for N-H bond dissociations in **1** and **3** predicted substantial stabilization of these radicals by kinetic shift in the gas phase. Additions of hydrogen atoms to the N-1, C-2, N-3, C-4, C-5, and C-6 ring positions in 4-aminopyrimidine were found to be exothermic by 68, 70, 76, 23, 91, and 62 kJ/mol at 0 K, respectively. Hydrogen atom addition to the NH_2 group was 58 kJ mol^{-1} endothermic. The activation barriers for the hydrogen atom additions to 4-aminopyrimidine were found to inversely correlate with the reaction enthalpies. The calculated rate constants predicted predominant (95%) hydrogen atom addition to C-5. The other positions were substantially less reactive, e.g., N-3 (2%), C-2 (1%), C-6 (0.8%), and N-1 (0.4%).

Pyridyl Cations and Radicals

Isomeric pyridyl radicals, 2-pyridyl (**2**), 3-pyridly (**3**) and 4-pyridyl (**4**) were studied by neutralization-reionization mass spectrometry (NRMS) and a combination of ab initio PMP2/6-311(2d,p) and density functional theory B3LYP/6-311G(2d,p) calculations. The experiment and theory agreed on the radicals being stable species in the gas phase. The order of 0 K relative enthalpies was established as **2** (most stable) < (**4** +17 kJ/mol) < 3 (+22 kJ/mol). This differed from the order of cation enthalpies which was $\mathbf{2}^+$ (most stable) < $\mathbf{3}^+$ (+90 kJ/mol) < $\mathbf{4}^+$ (+105 kJ/mol). Metastable-ion spectra of $\mathbf{2}^+$, $\mathbf{3}^+$, and $\mathbf{4}^+$ showed losses of hydrogen cyanide as the dominating dissociations, which were 273, 184 and 168 kJ/mol endothermic, respectively. Radical **2** underwent competitive dissociations by losses of acetylene and hydrogen cyanide for which comparable threshold energies, 292 and 290 kJ/mol, respectively, were obtained computationally. Radicals **3** and **4** cannot eliminate acetylene via low-energy paths or intermediates as investigated by computations. The lowest-energy dissociation in **3** was cleavage of the N-C2 bond and elimination of hydrogen cyanide to form the 3-buten-1-yl radical (**6**), which required 272 kJ/mol at the thermochemical threshold at 0 K. The lowest-energy dissociation in **4** proceeded by cleavage of the C2-C3 bond and elimination of hydrogen cyanide to form **6**, which required 273 kJ/mol at 0 K. The dissociations of pyridyl radicals observed upon collisional neutralization were, in general, consistent with the mechanisms of pyridine pyrolysis proposed earlier by Keifer, Kern, and coworkers[66] and by Hore and Russell.[67] The different energetics and dissociation mechanisms accounted for the differences in the NRMS spectra of $\mathbf{2}^+$-$\mathbf{4}^+$ which allowed partial isomer differentiation.

Alkenylammonium Cations

A series of isomeric hexenylammonium and hexenyldimethylammonium cations were neutralized by collisional electron transfer in the gas phase in an attempt to generate hypervalent ammonium radicals. The radicals dissociated completely on the 4.8-5.4 μs rime scale. Radicals in which the hexene double bond was in the 3-, 4-, and 5-positions dissociated by competitive N-H and N-C bond cleavages. Allylic 2-hexen-1-ylammonium and 2-hexen-1-yldimethylammonium radicals underwent predominant cleavages of allylic N-C bonds. Deuterium labeling experiments revealed no intramolecular hydrogen transfer from the hypervalent ammonium group to the hexene double bond. Ab initio and density functional theory calculations showed that alkenylammonium and alkenylmethyloxonium ions preferred hydrogen bonded structures in the gas phase. The stabilization through intramolecular H bonding in 3-buten-1-ylammonium and 3-buten-1-yl methyloxonium ions was calculated by B3LYP/6-311G(2d,p) at 26 and 18 kJ/mol, respectively. No intramolecular hydrogen bonding was found for the allylammonium ion. The hypervalent 3-buten-1-yl methyloxonium radical was calculated to be unbound and predicted to dissociate exothermically by O-H bond cleavage. This dissociation may provide kinetic energy for the hydrogen atom to overcome a small energy barrier for exothermic addition to the double bond. The 3-buten-1-ylammonium and allylammonium radicals were found to be bound and preferred gauche conformations without the intramolecular hydrogen bonding. Vertical neutralization of alkenylammonium ions was accompanied by small Franck-Condon effects. The failure to detect stable or metastable hypervalent alkenylammonium radicals was ascribed to the low activation barriers to exothermic dissociations by N-H and N-C bond cleavages.

Dabco

Hypervalent organic ammonium radicals were generated by collisional neutralization with dimethyl disulfide of protonated 1,4-diazabicyclo[2.2.2]octane (**1H**$^+$), N,N-dimethylpiperazine (**2H**$^+$) and N-methylpiperazine (**3H**$^+$). The radicals dissociated completely on the 5.1 μs time-scale. Radical 1H underwent competitive N-H and N-C bond dissociations producing 1,4-diazabicyclo[2.2.2]octane and small ring fragments. Dissociations of radical 2H proceeded by N-H bond dissociation and ring cleavage, whereas N-CH_3 bond cleavage was less frequent. Radical 3H underwent N-H, N-CH_3 and N-C_{ring} bond cleavages followed by post-reionization dissociations of the formed cations. The pattern of bond dissociations in the hypervalent ammonium radicals derived from six-membered nitrogen heterocycles is similar to those of aliphatic ammonium radicals.

References:

1. Cadet, J.; Weinfeld, M. *Anal. Chem.* **1993**, *65*, 675A.
2. A) Augusto, O. *Free Radic. Biol. Med.* **1993**, *15*, 329.
   B) McCord, J. M.; Fridovich, I. *J. Biol. Chem.* **1969**, *244*, 6049.
3. Feig, D.I.; Reid, T.M.; Loeb, L.A. *Cancer Res. (Suppl)*, **1994**, *54*, 1890.
4. Steenken, S. *Chem. Rev.* **1989**, *89*, 503.
5. Terlouw, J.K.; Schwarz, H. *Angew. Chem. Int. Ed. Engl.* **1985**, *26*, 805.
6. Lavertu, R.; Catte, M.; Pentenero, A.; Le Goff, P.; *Hebd. Seances Acad. Sci. Ser.* C263, **1966**, 1099.
7. Gellene, G.I.; Porter, R.F. *Int. J. Mass Spectrom. Ion Processes* **1985**, *64*, 55.
8. Holmes, J.L. *Mass Spectrom. Rev.* **1989**, 8, 513.
9. McLafferty, F.W. *Science* **1990**, *247*, 925.
10. A) Wesdemiotis, C.; McLafferty, F.W. *Chem. Rev.***1987**, *87*, 485.
    B) Holmes, J.L. *Mass Spectrom. Rev.* **1989**, *8*, 513.
    C) Wolken, J.K.; Nguyen, V.Q.; Turecek, F.T. *J. Mass Spectrom.* **1997**, *32*, 1162.
    D) Shaffer, S.A.; Wolken, J.K.; Turecek, F.T. *J. Am. Chem. Soc.* **1997**, *8*, 1111.
11. Hehre, W.J.; Radom, L.; Schleyer, P.v.R.; Pople, J.A. *Ab Initio Molecular Orbital Theory*; John Wiley & Sons, New York, 1986.
12. Møller, C.; Plesset, M.S. *Phys. Rev.* **1934**, *46*, 618.
13. Parr, R.G.; Yang, W. *Density Functional Theory of Atoms and Molecules*; Oxford University, New York, 1989.
14. Baer, T.; Hase, W.L. *Unimolecular Reaction Dynamics*; Oxford University, New York, 1996.
15. Baker, F.; Baley, E.C.C. *J. Chem. Soc.* **1907**, *91*, 1122.
16. Levin, E.S.; Rodionova, G.N. *Dokl. Chem.* (Eng. Transl.) **1965**, *164*, 910.
17. Beak, P. *Acc. Chem. Res.* **1977**, *10*, 186.
18. A) Cieplak, P.; Bash, P.; Singh, U.C.; Kollman, P.A. *J. Am. Chem. Soc.* **1987**, *109*, 6283.

B) Wong, M.W.; Wiberg, K.B.; Frisch, M.J. *J. Am. Chem. Soc.* **1992**, *114*, 1645.
C) Moreno, M.; Miller, W.H. *Chem. Phys. Lett.* **1990**, *171*, 475.

19. Bernstein, C.; Bernstein, H. *Aging, Sex, and DNA Repair*; Academic Press, New York, 1991.
20. Stryer, L. *Biochemistry*, 2nd Ed. W.H. Freeman, San Francisco, 1981.
21. The MIT experimental education home page. *esg-www.mit.edu:8001/bio/7001main.html*
22. Lindahl, T.; Nyberg, B. *Biochemistry* **13**, 3405.
23. Tice, R.R.; Setlow, R.B. *Handbook of the Biology of Aging*, Van Nostrand Reinhold, New York, 1985.
24. Shapiro, R.; *Chromosome Damage and Repair*, Plenum Press, New York, 1981.
25. Savva, R.; McAuley-Hecht K.; Brown, T.; Pearl, L. *Nature*, **1995**, 373, 487.
26. A) Florian, J.; Sponer, J.; Warshel, A. *J. Phys. Chem. B.* **1999**, 103, 884.
B) Plaxco, III, K.W.; Goddard, W.A. *Biochemistry* **1994**, 33, 3050.
27. Turecek, F.; Gu, M.; Shaffer, S.A. *J. Am. Soc. Mass Spectrom.* **1992**, 3, 493.
28. A) *Gaussian 94* (Revision E.3); Frisch, M.J.; Trucks, G.W.; Schlegel, H.B.; Gill, P.M.W., Johnson, B.G.; Robb, M.A.; Cheeseman, J.R.; Keith, T.A., Petersson, G.A.; Montgomery, J.A.; Raghavachari, K.; Al-Laham, M.A.; Zakrewski, V.G.; Ortiz, J.V.; Foresman, J.B.; Cioslowski, J.; Stefanov, B.B.; Nanayakkara, A.; Challacombe, M.; Peng, C.Y.; Ayala, P.Y.; Chen, W.; Wong, M.W.; Andres, J.L.; Replogle, E.S.; Gomperts, R.; Martin, R.L.; Fox, D.J.; Binkley, J.S.; Defrees, D.J.; Baker, J.; Stewart, J.P.; Head-Gordon, M.; Gonzalex, C.; Pople, J.A.; Gaussian: Pittsburgh, PA, 1995.
B) *Gaussian 98* (Revision A.7); Frisch, M.J.; Trucks, G.W.; Schlegel, H.B.; Scuseria, G.E.; Robb, M.A.; Cheeseman, J.R.; Zakrzewski, V.G.; J. A. Montgomery, Jr. J.A., Stratmann, R.E.; Burant, J.C.; Dapprich, S.; Millam, J.M.; Daniels, A.D.; Kudin, K.N.; Strain, M.C.; Farkas, O.; Tomasi, J.; Barone, V.; Cossi, M.;Cammi, R.; Mennucci, B.; Pomelli, C.; Adamo, C.; Clifford, S.; Ochterski, J.; Petersson, G.A.; Ayala, P.Y.; Cui, Q.; Morokuma, K.; Malick, D.K.;

Rabuck, A.D.; Raghavachari, K.; Foresman, J.B.; Cioslowski, J.; Ortiz,J.V.; Baboul, A.G.; Stefanov, B.B.; Liu, G.; Liashenko, A.; Piskorz, P.; Komaromi, I.; Gomperts, R.; Martin, R.L.; Fox, D.J.; Keith, T.; Al-Laham, M.A.; Peng,C.Y.; Nanayakkara, A.; Gonzalez, C.; Challacombe, M.; Gill, P.M.W.; Johnson, B.; Chen, W.; Wong, M.W.; Andres, J.L.; Gonzalez, C.; Head-Gordon, M.; Replogle, E.S.; Pople, J.A.
Gaussian, Inc., Pittsburgh PA, 1998.

29. A) Mayer, I. *Adv. Quantum Chem.* **1980**, *12*, 189.
B) Schlegel, H.B. *J. Chem. Phys.* **1986**, *84*, 4530.

30. Nobes, R.H.; Bouma, W.J.; Radom, L. *Chem. Phys. Lett.* **1982**, *89*, 497.

31. Curtiss, L.A.; Raghavachari, K.; Trucks, G.W.; Pople, J.A. *J. Chem. Phys.* **1991**, *94*, 7221.

32. A) Raghavachari, K.; Stefanov, B.B.; Curtiss, L.A. *J. Chem. Phys.* **1997**, *106*, 6764.
B) Curtiss, L.A.; Redfern, P.C.; Smith, B.J.; Radom, L. *J. Chem. Phys.* **1996**, *104*, 5148.
C) Smith, B.J.; Radom, L. *J. Phys. Chem.* **1995**, *99*, 6468.

33. Turecek, F.; Wolken, J.K. *J. Phys. Chem. A.* **1999**, *103*, 1905.

34. A) Zhu, L.; Hase, W.L. *Quantum Chemistry Program Exchange*; Indiana University: Bloomington, IN, 1994; Program No. QCPE 644.
B) Zhu, L.; Hase, W.L. *Chem. Phys. Lett.* **1990**, 175, 117.

35. Mallard, W.G.; Lindstrom, P.J.; Eds.; *NIST Chemical Webbook, NIST Standard Reference Database*; National Institute of Science and Technology, Gaithersburg, MD 1998; Vol. 69, http://webbook.nist.gov/chemistry

36. A) Bohme, D.K.; Mackay, G.I.; Schiff, H.I. *J. Chem. Phys.* **1980**, *73*, 4976.
B) Harrison, A.G.; *Chemical Ionization Mass Spectrometry*, 2nd ed.; CRC Press: Boca Raton, 1992.

37. Aue, D.H.; Webb, H.M.; Davidson, W.R.; Toure, P.; Hopkins, H.P., Jr.; Moulik, S.P.; Jahagirdar, D.V.; *J. Am. Chem. Soc.* **1991**, *113*, 1770.

38. A) Nguyen, V.Q.; Turecek, F. *J. Mass Spectrom.* **1996**, *31*, 1173.
B) Sakuri, H.; Jennings, K.R. *Org. Mass Spectrom.* **1981**, *16*, 393
C) Van Tilborg, M.W.E.M.; Van Thuijl, *J. Org. Mass. Spectrom.* **1983**, *18*, 331.

39. Lavorato, D.; Terlow, J.K.; Dargel, T.K.; Koch, W.; McGibbon, G.A.; Schwarz, H. *J. Am. Chem. Soc.* **1996**, *118*, 11898.

40. Steenken, S.; O'Neill, P. *J. Phys. Chem.* **1978**, *82*, 372.

41. Gilbert, R.G.; Smith, S.C. *Theory of Unimolecular and Recombination Reactions*; Blackwell: Oxford, 1990.

42. Lifshitz, C. *Mass Spectrom. Rev.* **1982**, *1*, 309.

43. From the heats of formation (kJ/mol) of **3** (-44), $\mathbf{3}^{+\bullet}$ (839), H• (218), and H^+ (1530) and the proton affinity of **3** (922).

44. A) Mason, R.; Harris, F.; *J. Chem. Soc., Chem. Commun.* **1987**, 1453.
B) Hrusak, J.; Schoder, D.; Weiske, T.; Schwarz, H. *J. Am. Chem. Soc.* **1993**, *115*, 2015.
C) Glukhovtsev, M.N.; Pross, A.; Nicolaides, A.; Radom, L. *J. Chem. Soc. Chem. Commun.* **1995**, 2347.
D) Szulejko, J.E.; Hrusak, J. McMahon, T.B. *J. Mass Spectrom.* **1997**, *32*, 494.

45. Wolken, J.K.; Turecek, F. *J. Phys. Chem. A.* **1999**, *103*, 6268.

46. Uggerud, E. *Adv. Mass Spectrom.* **1995**, *13*, 53.

47. A) Frank, A.J.; Sadilek, M.; Ferrier, J.G.; Turecek, F. *J. Am. Chem. Soc.* **1997**, 119, 12343.
B) Sadilek, M.; Turecek, F. *J. Phys. Chem.* **1996**, *100*, 15027.
C) Sadilek, M.; Turecek, F. *Chem. Phys. Lett.* **1996**, *263*, 203.
D) Sadilek, M.; Turecek, F. *J. Phys. Chem.* **1996**, *100*, 224.

48. Foresman, J.B.; Head-Gordon, M.; Pople, J.A.; Frisch, M. *J. Phys. Chem.* **1992**, *96*, 135.

49. Turro, N.J. *Modern Molecular Photochemistry*; University Science Books: Mill Valley, 1991.

50. Brown, R.S.; Tse, A.; Vederas, J.C. *J. Am. Chem. Soc.* **1980**, *102*, 1175.

51. Matyas, P.; Fuji, K.; Tanak, K. *Tetrahedron* **1994**, *50*, 2405.

52. A) Imuzuka, K. *Nippon Kagaku Kaishi* **1998**, 149.

B) Kwiatkowski, J.S.; Leszczynski, J. *J. Mol. Struct.* **1996**, *376*, 325.

C) Spioliti, M.; Bencivenni, L.; Diomedi-Carmassei, F.; D'Alessio, L. *Rass Chim.* **1993**, *45*, 143; *Chem. Abstr.* **1995**, *123*, 339007.

D) Kwiatkowski, J.S.; Leszczynski, J. *THEOCHEM* **1994**, *118*, 201.

E) Les, A.; Adomawicz, L.; Nowak, M.J.; Lapinski, L. *THEOCHEM* **1994**, *118*, 157.

53. Baker, J.; Scheiner, A.; Andzelm, J. *Chem. Phys. Lett.* **1993**, *216*, 380.

54. A) McMillen, D.F.; Golden, D.M. *Annu. Rev. Phys. Chem.* **1982**, *33*, 493.

B) Burkey, T.J.; Castelhano, A.L.; Griller, D.; Lossing, F.P. *J. Am. Chem. Soc.* **1983**, *105*, 4701.

C) MacInnes, I.; Walton, J.C.; Nonhebel, D.C. *J. Chem. Soc., Perkin Trans. 2* **1987**, 1789.

55. Bordwell, F.G.; Zhang, X.M.; Alnajjar, M.S. *J. Am. Chem. Soc.* **1992**, *114*, 7623.

56. Sustmann, R.; Korth, H.G. *Adv. Phys. Org. Chem.* **1990**, *26*, 131.

57. A) Williams, B.W.; Porter, R.F. *J. Chem. Phys.* **1980**, *73*, 5598.

B) Jeon, S.J.; Raksit, A.B.; Gellene, G.I.; Porter, R.F. *J. Am. Chem. Soc.* **1985**, *107*, 4129.

C) Boldyrev, A.I.; Simons, J. *J. Chem. Phys.* **1992**, *97*, 6621.

D) Shaffer, S.A.; Turecek, F. *J. Am. Chem. Soc.* **1994**, *116*, 8647.

58. Nguyen, V.Q.; Turecek, F. *J. Am. Chem. Soc.* **1997**, *119*, 2280.

59. A) Gerson, F.; Gleiter, R.; Moshuk, G.; Dreiding, A. A. *J. Am. Chem. Soc.* **1974**, *96*, 2342.

B) Russell, G.A. *The Chemistry of Enones*; Patai, S. Rappoport, Z. Eds.; Wiley-Interscience: Chichester, 1989; Chapter 11.

60. Nguyen, V.Q.;Sadilek, M.; Frank, A.J.; Ferrier, J.G.; Turecek, F. *J. Phys. Chem. A*, **1997**, *101*, 3789.

61. Fitch, W.L.; Sauter, A.D. *Anal. Chem.* **1983**, *55*, 832.

62. Hartland, G.V.; Qin, D.; Dai, H.L.; Chen. C. *J. Chem. Phys.* **1997**, *107*, 2890.

63. Turecek, F.; Wolken, J.K.; Sadilek, M. *Euro. Mass Spectrom.* **1998**, *4*, 321.

64. Shaffer, S.A.; Wolken, J.K.; Turecek, F. *J. Am. Soc. Mass Spectrom.* **1997**, *11*, 1111.

65. Wolken, J.K.; Nguyen, V.Q.; Turecek, F. J. Mass. Spectrom. **1997**, 1169.

66. Kiefer, J.H.; Zhang, Q.; Kern, R.D.; Yao, J.; Jursic, B. *J. Phys. Chem. A.* **1997**, *101*, 7061.

67. Hore, N.R.; Russell, D.K. *J. Chem. Soc. Perkin Trans 2*, **1998**, 269.

JILL K. WOLKEN

4308 9th Avenue NE
Seattle, WA 98105

206/545-7444 (home)
206/543-7656 (work)
206/685-7885 (fax)
jwolken@u.washington.edu

CAREER OBJECTIVE

I am particularly interested in further developing my mass spectrometry skills in a post-doctoral bio-analytical research position.

EDUCATION

Ph.D., Analytical Chemistry, University of Washington, Seattle, WA, to be completed June 2000
"A Mass Spectrometric and Computational Analysis of Biologically-Relevant Radicals"
Advisor: Professor Frantisek Turecek

B.A., Chemistry, College of Wooster, Wooster, OH, 1993
American Chemical Society certification (with an extra concentration in Physics)
Thesis: "Crystallization and X-ray Determination of a Cyclic Phenylsulfonamide Compound"
Advisor: Professor Virginia Pett

RESEARCH EXPERIENCE

1994-present — Graduate Assistant, University of Washington
Advisor: Professor Frantisek Turecek
- Implemented a neutralization-reionization mass spectrometry study of biologically relevant radicals, recently focusing on cytosine and uracil
- Studied protonated molecules with a range of internal energies to determine radical stability dependence on internal energy
- Modeled relevant radicals and ions using *ab initio* and density functional theory to determine proton affinity, thermodynamic stability, and possible fragmentation pathways

1996 — Summer Intern, Pacific Northwest National Laboratories (PNNL)
Supervisor: Dr. John Price
- Conducted cooperative research between University of Washington and PNNL
- Built a laser ablation ion trap to study metal – chlorinated compound reactions

1994 — Graduate Assistant, University of Oregon
Supervisor: Professor David Johnson
- Deposited tin and selenium oxide thin layers onto silicon disks using a vacuum deposition chamber
- Determined physical properties of the oxides using X-ray powder diffraction, gravimetric, and potentiometric analysis

1992-1993	Senior Thesis, The College of Wooster Advisor: Professor Virginia Pett • Determined optimal crystallization conditions for a hemoglobin model compound • Analyzed the crystal structure of the model compound by X-ray crystallography
1992	Summer Intern, Duke University Supervisor: Professor Peter Smith • Targeted heterocyclic reaction intermediate radicals in an electron paramagnetic resonance (EPR) spectrometer • Used a continuous flow system to create transient radicals to detect the short-lived reaction intermediate radicals
1991	Summer Intern, The College of Wooster Supervisor: Professor Don Jacobs • Examined heat capacities of the binary fluid triethylamine (TEA) and water • Calibrated the thermister readings from the sample cell

SKILLS

Instrumentation:

- Operated, maintained, and repaired a Neutralization-Reionization M.S.
- Operated JEOL HX 110 tandem M.S (EB)
- Operated Kratos tandem M.S.
- Operated Bruker Esquire, ESI - ion trap M.S.
- Utilized basic electronics and mechanics to build an laser-ablation ion-trap M.S.
- Taught advanced analytical students utilizing GC-MS, HPLC, AA, ICP-AES, FTIR, UV-Vis, Anode Stripping Voltometry, and Flow Injection Analysis

Computation:

- Employed Gaussian 94 and Gaussian 98 to determine optimized geometries, single point energies, Frank-Condon energies and transition state analysis of biologically relevant molecules
- Modeled reaction kinetics using RRKM calculation
- Employed Chem3D and Spartan as both front and back end graphical interfaces with Gaussian 94 and Gaussian 98
- Created several publications and presentations utilizing SigmaPlot, Excel, and Word

HONORS / AWARDS

Mindlin Graduate Fellowship Recipient 1999
Team Captain for a city league soccer team 1999-2000
Invited panel speaker for Women in Engineering Conference 1997
ASUW scholar 1996 – Funded research at PNNL
Honors on senior Independent Study 1993
American Chemical Society Certification 1993
Secretary for Women in Science Chapter 1992-1993
COSEN Scholar 1992 – Funded research at Duke University
Howard Hughes Scholar 1991 – Funded research, The College of Wooster
Presbyterian Scholarship 1989-1991
Volunteered over 700 hours at COSI science museum, Columbus OH 1986-1989

PUBLICATIONS

"Modeling Nucleobase Radicals in the Gas Phase. Experimental and Computational Study of 2-Hydroxypyridinium and 2-(1H)Pyridone Radicals" Wolken, J.K., Turecek, F., *J. Phys. Chem. A.* **1999**,103, 6268-6281.

"Heterocyclic Radicals in the Gas Phase. An Experimental and Computational Study of 3-Hydroxypyridium Radicals and Cations" Wolken, J.K., Turecek, F., *J. Am. Chem. Soc.* **1999**, 121, 6010-6018.

"Dissociation Energies and Kinetics of Aminopyrimidinium Radicals by *ab initio* and Density Functional Theory" Turecek, F., Wolken, J.K., *J. Phys. Chem. A.* **1999**, 103, 1905-1912.

"Distinction of Isomeric Pyridyl Cations and Radicals by Neutralization-Reionization Mass Spectrometry, *ab initio* and Density Functional Theory Calculations" Turecek, F., Wolken, J.K., Sadilek, M., *Euro. Mass Spectrom.* **1998**, 4, 321-332.

"Bond Dissociations in Hypervalent Ammonium Radicals Prepared by Collisional Neutralization of Protonated Six-membered Nitrogen Heterocycles" Wolken, J.K., Nguyen V.Q., Turecek F., *J. Mass Spectrom.* **1997**, 1169.

"Neutralization-reionization of Alkenylammonium Cations: An Experimental and ab initio Study of Intramolecular N-H Center Dot C=C Interactions in Cations and Hypervalent Ammonium Radicals" Shaffer S.A., Wolken J.K., Turecek F., *J. Am. Soc. Mass Spectrom.* **1997**, 8, 1111-1123.

PRESENTATIONS

"Neutralization–Reionization Mass Spectrometry and Computational Study of Uracil" 47th American Society for Mass Spectrometry Conference, Dallas, TX, June 1999.

"Determination of Cocaine Use through Florescence Polarization Immunoassay" Analytical Chemistry Seminar, Department of Chemistry, University of Washington, Seattle, WA, April 1996.

POSTERS

"Neutralization–Reionization Mass Spectrometry and *ab initio* Calculation Study of DNA Model Compounds: 2-hydroxypyridine/2-pyridone and 3-hydroxypyridine" 46th American Society for Mass Spectrometry Conference, Orlando, FL, June 1998.

"A Study of 2-Hydroxypyridine and 3-Hydroxypyridine using Neutralization–Reionization Mass Spectrometry" 45th American Society for Mass Spectrometry Conference, Palm Springs, CA, June 1997.

"Cyclic Hypervalent Ammonium Radicals" 44th American Society for Mass Spectrometry Conference, Portland, OR, June 1996.